

POLITECNICO DI TORINO

Collegio di Ingegneria Meccanica,
Aerospaziale, dell'Autoveicolo e della Produzione

**Master's Degree Course in
Mechanical Engineering**

Master of Science Thesis

Investigation of Geometrical Parameters
Influencing the Aerodynamic Damping of
an Axial Compressor



Advisors

Prof. Stefano Zucca
Prof. Damian M. Vogt
Dipl.-Ing. Patrick Buchwald

Candidate

Aydin Farahmand

April 2018

Abstract

The flow in turbomachines is inherently unsteady and creates alternating loads on the components. In particular, the rotor and stator blades are exposed to highly unsteady pressure and velocity fields due to upstream wakes and turbulence along with potential effects of neighboring rows, resulting in unsteady forces and thus vibration of the blades. If the frequency, phase and distribution of the forces coincide with an eigenmode of the structure, the vibration amplitudes will grow larger, with the maximum amplitude depending on the overall damping of the structure. Especially for integrated rotors (blisks) with very low mechanical and frictional damping, the aerodynamic damping of the blades determines the vibration amplitude and hence the stability of the structure.

Aerodynamic damping describes the influence of the unsteady aerodynamic forces on the oscillating blades, which can be either stabilizing or destabilizing, depending on several geometrical and physical parameters. In order to design reliable, highly efficient turbomachines with high pressure ratios and improved performance, the exact determination of the aerodynamic damping during the design process is crucial, however though an accurate prediction of the unsteady aerodynamic forces with transient CFD simulations is still very time consuming and requires enormous computational powers. Furthermore, there are no specific geometrical design parameters regarding aerodynamic damping yet, which could help to decrease the number of design iterations in design process of new turbomachines.

The main objective of this work has been to investigate, if there are correlations between specific geometrical parameters such as blade angle distribution and the aerodynamic damping of an axial compressor rotor. In order to determine the appropriate setup for the transient CFD simulations for investigation of the aerodynamic damping coefficient, initially, a numerical influence study has been performed for a grid including an isolated rotor representing the subjected rotor geometry under investigation. Subsequently, geometrical parameters have been identified and the baseline rotor blisk has been then be modified according to a test matrix of the parameters. The rotor design was realized using ANSYS DesignModeler and BladeGen, with the subsequent CFD mesh being developed using Numeca AutoGrid. Once modal analysis of the blisks were performed in ANSYS Mechanical Classic, transient CFD simulations have been performed using ANSYS CFX 18 to determine the aerodynamic damping, utilizing both the "Traveling Wave Mode" approach and the "Influence Coefficients Method".

Keywords: *aerodynamic damping, aeroelasticity, turbomachinery, CFD, forced response, flutter, FEM, traveling wave mode, influence coefficients method*

Acknowledgements

I would like to express my gratitude to my advisor Patrick Buchwald at the Institute of Thermal Turbomachinery and Machinery Laboratory at the University of Stuttgart, for introducing me to the field of aeroelasticity and for his dedication, patience and enthusiastic support through every aspect of this work. In addition, I also would like to thank Prof. Damian Vogt, for providing me the opportunity to work on this interesting topic in such a stimulating environment.

Special thanks goes to my supervisor at Politecnico di Torino, Prof. Stefano Zucca for his collaboration, support, and for taking active interest in my work and providing valuable comments and suggestions in our discussions.

Contents

| | |
|--|-------------|
| List of Figures | xi |
| List of Tables | xvii |
| Nomenclature | xix |
| 1 Introduction | 1 |
| 2 Literature Review | 3 |
| 2.1 Basic Principles of Aeroelasticity | 3 |
| 2.1.1 Static Aeroelasticity | 4 |
| 2.1.2 Dynamic Aeroelasticity | 4 |
| 2.2 Aeroelasticity in Turbomachines | 4 |
| 2.2.1 Forced Response | 4 |
| 2.2.2 Flutter | 5 |
| 2.2.3 Compressor Flutter Map | 8 |
| 2.2.4 Acoustic Resonance | 9 |
| 2.3 Aerodynamic Damping | 9 |
| 2.3.1 Aeroelastic Equation of Motion | 10 |
| 2.3.2 Aerodynamic Coupling | 11 |
| 2.3.3 Traveling Wave Mode Approach | 12 |
| 2.3.4 Influence Coefficients Method | 14 |
| 2.3.5 Influence of Incidence Angle and Mode Shapes | 16 |
| 2.4 Governing Equations | 17 |
| 2.4.1 Basic Principles of Computational Fluid Dynamics | 17 |
| 2.4.2 Structural Dynamics Analysis | 19 |
| 3 Objectives and Approach | 21 |
| 4 Baseline Rotor Design | 23 |

| | | |
|----------|---|-----------|
| 5 | Computational Fluid Dynamics Model | 25 |
| 5.1 | CFD Mesh Generation | 25 |
| 5.1.1 | Mesh Domain Definition | 25 |
| 5.1.2 | Meridional Control | 26 |
| 5.1.3 | Blade to Blade Control | 26 |
| 5.2 | CFD Simulation Setup | 28 |
| 5.2.1 | Domain Settings | 28 |
| 5.2.2 | Boundary Conditions | 30 |
| 5.2.3 | Solver Control Settings | 33 |
| 5.3 | Post-Processing Unsteady CFD Simulation Results | 34 |
| 5.3.1 | Post-Processing Procedure in Time-Domain and Frequency-Domain . | 34 |
| 5.3.2 | Calculation of Aerodynamic Damping Ratio | 35 |
| 6 | Structural Dynamics Analysis | 39 |
| 6.1 | FEM Simulation Setup | 39 |
| 6.2 | Mesh Independence Study | 40 |
| 6.3 | Baseline Rotor Structural Analysis Results | 41 |
| 7 | CFD Numerical Influence Study | 43 |
| 7.1 | Steady State Simulations | 43 |
| 7.2 | Unsteady Simulations | 47 |
| 7.2.1 | Mesh Resolution | 48 |
| 7.2.2 | Number of Time-Steps per Period | 49 |
| 7.2.3 | Varying Amplitude of Mesh Displacement | 49 |
| 7.3 | Traveling Wave Mode Simulations | 50 |
| 7.4 | Influence Coefficients Method Simulations | 51 |
| 8 | Influence of Frequency Variations on the Aerodynamic Damping of the Baseline Rotor | 55 |
| 8.1 | 1 st Bending Mode | 55 |
| 8.2 | 1 st Torsional Mode | 59 |
| 9 | Influence of Blade Count on Aerodynamic Damping | 63 |
| 9.1 | Scaling Technique | 63 |
| 9.2 | Modal Analysis | 64 |
| 9.3 | Steady State Analysis | 66 |

| | | |
|-----------|--|------------|
| 9.4 | Unsteady CFD Analysis | 67 |
| 9.5 | Results | 68 |
| 9.5.1 | 1 st Bending Mode (Blades Vibrating at Different Frequencies) | 68 |
| 9.5.2 | 1 st Bending Mode (Blades Vibrating at the Same Frequency) | 72 |
| 9.5.3 | 1 st Torsional Mode (Blades Vibrating at Different Frequencies) | 74 |
| 9.5.4 | 1 st Torsional Mode (Blades Vibrating at the Same Frequency) | 77 |
| 9.6 | Conclusion | 81 |
| 10 | Influence of Blade Loading Distribution on Aerodynamic Damping | 83 |
| 10.1 | Steady State Analysis | 84 |
| 10.2 | Modal Analysis | 85 |
| 10.3 | Unsteady CFD Analysis | 86 |
| 10.4 | Results | 86 |
| 10.4.1 | 1 st Bending Mode (Blades Vibrating at Different Frequencies) | 86 |
| 10.4.2 | 1 st Bending Mode (Blades Vibrating at the Same Frequency) | 89 |
| 10.4.3 | 1 st Torsional Mode (Blades Vibrating at Different Frequencies) | 91 |
| 10.4.4 | 1 st Torsional Mode (Blades Vibrating at the Same Frequency) | 94 |
| 10.5 | Conclusion | 97 |
| 11 | Conclusion and Future Work | 99 |
| | Bibliography | 101 |

List of Figures

| | | |
|------|---|----|
| 2.1 | Collar's triangle of forces, adapted from [4] | 3 |
| 2.2 | Campbell diagram indicating the occurrence of flutter, adapted from [27] . . | 5 |
| 2.3 | Cross-section of a EuroJet EJ200 low bypass turbofan engine [18] | 6 |
| 2.4 | Graphical interpretation of mass ratio and reduced frequency, [27] | 7 |
| 2.5 | Compressor flutter map, [10] | 8 |
| 2.6 | Graphical representation of aerodynamic coupling, [27] | 11 |
| 2.7 | Graphical representation of nodal diameters of a disk, traveling wave mode shapes and the corresponding instantaneous blade row geometry, [27] | 12 |
| 2.8 | Phase shift between blade motion and unsteady pressure perturbation [17] . | 13 |
| 2.9 | Superposition of the influence coefficients from blades -1 and +1 on blade 0 for $\sigma = 0$ and $\sigma = 90^\circ$, [27] | 14 |
| 2.10 | An example of a typical S-Curve, along with a schematic contribution of blade pairs on overall stability parameter, [27] | 15 |
| 2.11 | Torsion mode representation of rigid-body modes along with an example of stability plots for a LPT cascade at different operating conditions, [27] . . | 16 |
| 2.12 | An arbitrary control volume, [3] | 17 |
| 3.1 | Graphical representation of the overall work-flow | 22 |
| 4.1 | Baseline rotor geometry | 24 |
| 5.1 | An example of a medium mesh domain generated for the baseline rotor . . . | 26 |
| 5.2 | An overview of the O4H block topology formed at the midspan position (left) and shroud gap region (right) | 27 |
| 5.3 | An overview of the surface CFD mesh with its displaced shape (left) and a graphical representation of the mapping process (right) | 30 |
| 5.4 | An overview of the boundary conditions imposed for a model with four passages | 31 |
| 5.5 | An example of extracted influence coefficients for a setup with 17 blades (left), and an example of a S-curve calculated both in time and frequency domain(right) | 36 |

| | | |
|------|--|----|
| 6.1 | The Geometry, node locations and the coordinate system for SOLID-187 element, [2] | 39 |
| 6.2 | Influence of mesh size on the first three eigen-frequencies | 40 |
| 6.3 | A graphical representation of 10 first modes shapes of the baseline rotor . . | 41 |
| 7.1 | Mesh grid refinement from a very coarse mesh (left) to a very fine mesh (right) | 44 |
| 7.2 | Comparison of efficiency η_{tt} and compression ratio Π_{tt} for various meshes size | 45 |
| 7.3 | Comparison of efficiency η_{tt} and compression ratio Π_{tt} for various operating points | 46 |
| 7.4 | Mach number plots for different meshes at 0.9 and 0.5 span positions | 46 |
| 7.5 | Steady State simulation mesh (left), compared to unsteady simulation mesh (right) with modified upstream and downstream channel length and mesh resolution | 47 |
| 7.6 | Monitor points for efficiency, compression ratio (left) and aerodynamic damping (right) | 48 |
| 7.7 | Normalized aerodynamic damping ratio as a function of mesh resolution . . | 49 |
| 7.8 | Aerodynamic damping ratio as a function of number of time-steps per period | 49 |
| 7.9 | Aerodynamic damping ratio as a function of maximum amplitude of mesh motion | 50 |
| 7.10 | S-Curve for the baseline case with blades vibration at the 1st bending mode | 50 |
| 7.11 | Comparison of S-Curves obtained with TWM and ICM approaches | 51 |
| 7.12 | Comparison of blade influence coefficients obtained through ICM simulations for two computational domains with different number of simulated passages | 52 |
| 7.13 | S-Curves obtained using ICM method with different number of passages . . | 53 |
| 7.14 | Blade influence coefficients obtained using ICM method with different number of passages | 53 |
| 8.1 | Characteristic S-Curve of the baseline rotor with different blade oscillation frequencies | 56 |
| 8.2 | Blade influence coefficients of baseline rotor with different blade oscillation frequencies | 56 |
| 8.3 | Variations of the normalized blade influence coefficients as a function of blade oscillation frequency, 1 st bending mode | 57 |

| | | |
|------|--|----|
| 8.4 | Local aerodynamic damping ratio (left), amplitude of the local complex work per cycle (center) and phase shift between the local complex force and complex displacement values (right) plotted on the suction and pressure side of baseline rotor blade (1^{st} bending, $\sigma = 0$) | 58 |
| 8.5 | Characteristic S-Curve of the baseline rotor with different blade oscillation frequencies | 59 |
| 8.6 | Blade influence coefficients of baseline rotor with different blade oscillation frequencies | 60 |
| 8.7 | Variations of the normalized blade influence coefficients as a function of blade oscillation frequency, 1^{st} torsional mode | 60 |
| 8.8 | Local aerodynamic damping ratio (left), amplitude of the local complex work per cycle (center) and phase shift between the local complex force and complex displacement values (right) plotted on the suction and pressure side of baseline rotor blade (1^{st} torsional, $\sigma = 0$) | 61 |
| 9.1 | Blade hub profile of modified rotors with various blade count | 64 |
| 9.2 | A graphical representation of the 1^{st} bending and the 1^{st} torsional modes of different blades corresponding to rotors with variable blade count | 64 |
| 9.3 | Comparison of eigen-frequencies and MAC numbers for different blades corresponding to rotors with variable blade count | 65 |
| 9.4 | Blade loadings plot (left) and steady-state aerodynamic performance variations (right) compared for different cases | 66 |
| 9.5 | S-Curve for rotors with various blade count oscillating in different frequencies | 68 |
| 9.6 | Blade influence coefficients for rotors with various blade count oscillating in different frequencies | 69 |
| 9.7 | Local aerodynamic damping ratio (left), amplitude of the local complex work per cycle (center) and phase shift between the local complex force and complex displacement values (right) plotted on the suction and pressure side of baseline rotor blade (mode 1, $\sigma = 0$) | 70 |
| 9.8 | Local aerodynamic damping ratio (left), amplitude of the local complex work per cycle (center) and phase shift between the local complex force and complex displacement values (right) plotted on the suction and pressure side of the modified rotor with 21 blades (mode 1, $\sigma = 0$) | 70 |
| 9.9 | Phase shift between the local complex force and complex displacement values plotted on the pressure side of modified rotor consisting of 25 blades (mode 1, $\sigma = 0$) | 71 |
| 9.10 | Phase shift between the local complex force and complex displacement values (left) and the local wall shear stress values (right) plotted on the suction side of modified rotor consisting of 25 blades (mode 1, $\sigma = 0$) | 71 |
| 9.11 | S-Curve for rotors with various blade count oscillating in same frequency | 72 |

| | |
|---|----|
| 9.12 Blade influence coefficients for rotors with various blade count oscillating in same frequency | 73 |
| 9.13 Local aerodynamic damping ratio (left), amplitude of the local complex work per cycle (center) and phase shift between the local complex force and complex displacement values (right) plotted on the suction and pressure side of baseline rotor blade (mode 1, $\sigma = 0$) | 73 |
| 9.14 Local aerodynamic damping ratio (left), amplitude of the local complex work per cycle (center) and phase shift between the local complex force and complex displacement values (right) plotted on the suction and pressure side of the modified rotor with 25 blades (mode 1, $\sigma = 0$) | 74 |
| 9.15 S-Curve for rotors with various blade count oscillating in different frequencies | 75 |
| 9.16 Blade influence coefficients for rotors with various blade count oscillating in different frequencies | 75 |
| 9.17 Local aerodynamic damping ratio (left), amplitude of the local complex work per cycle (center) and phase shift between the local complex force and complex displacement values (right) plotted on the suction and pressure side of baseline rotor blade (mode 2, $\sigma = 84.7$) | 76 |
| 9.18 Local aerodynamic damping ratio (left), amplitude of the local complex work per cycle (center) and phase shift between the local complex force and complex displacement values (right) plotted on the suction and pressure side of the modified rotor with 25 blades (mode 2, $\sigma = 100.8$) | 76 |
| 9.19 S-Curve for rotors with various blade count oscillating in same frequency . . | 78 |
| 9.20 Blade influence coefficients for rotors with various blade count oscillating in same frequency | 78 |
| 9.21 Local aerodynamic damping ratio (left), amplitude of the local complex work per cycle (center) and phase shift between the local complex force and complex displacement values (right) plotted on the suction and pressure side of baseline rotor blade (mode 2, $\sigma = 84.7$) | 79 |
| 9.22 Local aerodynamic damping ratio (left), amplitude of the local complex work per cycle (center) and phase shift between the local complex force and complex displacement values (right) plotted on the suction and pressure side of the modified rotor with 25 blades (mode 2, $\sigma = 100.8$) | 79 |
| 9.23 S-Curves of the rotor consisting of 25 blades compared at two different frequencies (mode 2, $\sigma = 100.8$) | 80 |
| 9.24 Local aerodynamic damping ratio (left), amplitude of the local complex work per cycle (center) and phase shift between the local complex force and complex displacement values (right) plotted on the suction and pressure side of the modified rotor with 25 blades (mode 2, $\sigma = 100.8$) | 80 |
| 10.1 Variations of the (β_2) angle as a function of the spanwise position for different cases of modified geometries | 83 |

| | |
|--|----|
| 10.2 Steady state aerodynamic performance of the investigated cases with variable β_2 angle | 84 |
| 10.3 Blade loading plots at 0.1 span positions (left), 0.5 span position (center) and 0.9 span position (right) | 85 |
| 10.4 Graphical representation of the 1 st bending and 1 st torsional mode shapes of the investigated cases with variable β_2 angle | 85 |
| 10.5 S-Curve for rotors with various trailing edge angle oscillating in different frequencies | 87 |
| 10.6 Blade influence coefficients for rotors with various trailing edge angle oscillating in different frequencies | 87 |
| 10.7 Local aerodynamic damping ratio (left), amplitude of the local complex work per cycle (center) and phase shift between the local complex force and complex displacement values (right) plotted on the suction and pressure side of baseline rotor blade (mode 1, $\sigma = 0$) | 88 |
| 10.8 Local aerodynamic damping ratio (left), amplitude of the local complex work per cycle (center) and phase shift between the local complex force and complex displacement values (right) plotted on the suction and pressure side of the modified rotor of case 6 (mode 1, $\sigma = 0$) | 88 |
| 10.9 S-Curve for rotors with various trailing edge angle oscillating in same frequency | 89 |
| 10.10 Blade influence coefficients for rotors with various trailing edge angle oscillating in same frequency | 90 |
| 10.11 Local aerodynamic damping ratio (left), amplitude of the local complex work per cycle (center) and phase shift between the local complex force and complex displacement values (right) plotted on the suction and pressure side of baseline rotor blade (mode 1, $\sigma = 0$) | 90 |
| 10.12 Local aerodynamic damping ratio (left), amplitude of the local complex work per cycle (center) and phase shift between the local complex force and complex displacement values (right) plotted on the suction and pressure side of the modified rotor of case 12 (mode 1, $\sigma = 0$) | 91 |
| 10.13 S-Curve for rotors with various trailing edge angle oscillating in different frequencies | 92 |
| 10.14 Blade influence coefficients for rotors with various trailing edge angle oscillating in different frequencies | 92 |
| 10.15 Local aerodynamic damping ratio (left), amplitude of the local complex work per cycle (center) and phase shift between the local complex force and complex displacement values (right) plotted on the suction and pressure side of baseline rotor blade (mode 2, $\sigma = 0$) | 93 |

| | | |
|-------|--|----|
| 10.16 | Local aerodynamic damping ratio (left), amplitude of the local complex work per cycle (center) and phase shift between the local complex force and complex displacement values (right) plotted on the suction and pressure side of the modified rotor of case 5 (mode 2, $\sigma = 0$) | 94 |
| 10.17 | S-Curve for rotors with various trailing edge angle oscillating in same frequency | 95 |
| 10.18 | Blade influence coefficients for rotors with various trailing edge angle oscillating in same frequency | 95 |
| 10.19 | Local aerodynamic damping ratio (left), amplitude of the local complex work per cycle (center) and phase shift between the local complex force and complex displacement values (right) plotted on the suction and pressure side of baseline rotor blade (mode 2, $\sigma = 0$) | 96 |
| 10.20 | Local aerodynamic damping ratio (left), amplitude of the local complex work per cycle (center) and phase shift between the local complex force and complex displacement values (right) plotted on the suction and pressure side of the modified rotor of case 12 (mode 2, $\sigma = 0$) | 96 |

List of Tables

| | | |
|------|--|----|
| 2.1 | Typical flutter reduced frequency ranges, [10] | 7 |
| 2.2 | Values of reduced frequency for which flutter has been observed, [22] | 7 |
| 4.1 | Summary of compressor design parameters | 23 |
| 4.2 | Summary of material properties (17-4 PH Stainless Steel), [5] | 23 |
| 4.3 | Blade profile parameters | 24 |
| 6.1 | 10 first eigen-frequencies of the baseline blisk rotating at 16200 RPM | 41 |
| 7.1 | Summary of the steady state simulation setup settings | 43 |
| 7.2 | Steady State simulation CFD mesh parameters | 44 |
| 7.3 | Summary of the unsteady simulation setup settings | 47 |
| 7.4 | Unsteady simulation CFD mesh parameters | 48 |
| 7.5 | Computational time required for CFD simulation using TWM and ICM methods | 52 |
| 9.1 | An overview of unsteady CFD setups and computational effort for different cases | 67 |
| 10.1 | Geometrical parameters for different cases with modified trailing edge angle | 84 |
| 10.2 | Frequencies of the first two mode shapes of investigated cases with variable β_2 angle | 85 |

Nomenclature

Latin Letters

| | | |
|-------------|-------------------|--|
| b | m | blade span height |
| C | m | chord length |
| C | kg/s | damping matrix |
| C | - | turbulence intensity factor |
| c | N s/m | damping coefficient |
| c_{cr} | N s/m | critical damping coefficient |
| c_p | J/kgK | specific heat capacity at constant pressure |
| d | m | distance from the nearest boundary |
| ds | m ² | infinitesimal arcwise surface component, per unit span |
| e_t | J/kg | specific total energy |
| F | N | force, force vector |
| \hat{F} | N | complex force vector |
| f | Hz | frequency |
| \hat{h} | - | complex mode shape vector |
| I | - | identity matrix |
| I | - | turbulence intensity |
| i | - | imaginary unit, $i = \sqrt{-1}$ |
| K | kg/s ² | stiffness matrix |
| k | - | reduced frequency |
| L_{ref} | m | reference length of the test case |
| l | - | nodal diameter |
| M | kg | mass matrix |
| m | kg | mass |
| m | kg/m | mass per unit wing span |
| m, n | - | blade indices |
| \dot{m} | kg/s | mass-flow rate |
| N | - | number of blades |
| N_{NB} | - | number of blades |
| \vec{n} | - | normal vector to surface element |
| p | N/m ² | pressure |
| \bar{p} | N/m ² | mean pressure |
| \hat{p} | N/m ² | complex pressure perturbation |
| \tilde{p} | N/m ² | time-dependent fluctuating pressure |

| | | |
|--------------------|-----------------------|---|
| p_{dyn} | Pa | dynamic pressure |
| \bar{Q} | m | modal displacement vector |
| q_{α} | W/m | thermal flux |
| R | m | radius |
| S | m | span height |
| S | m^2 | surface area |
| Sf | - | blade scaling factor |
| T | s | oscillation period |
| t | s | time |
| u | m/s | flow velocity |
| \vec{u} | m/s | velocity vector |
| u_{ref} | m/s | reference velocity of the flow |
| u_{τ} | m/s | friction velocity, shear velocity |
| V | m^3 | volume |
| \vec{v} | m/s | velocity vector |
| X | m | displacement vector |
| \dot{X} | m/s | first derivative of displacement vector (velocity) |
| \ddot{X} | m/s^2 | second derivative of displacement vector (acceleration) |
| x, y, z | m | Cartesian coordinates |
| Y^+ | - | dimensionless wall distance parameter |
| Y_{wall} | m | distance of the nearest grid to the wall |
| W_{cycle} | J | work per cycle |

Greek Letters

| | | |
|--|----------------------------|---|
| α | m^2/s | thermal diffusivity |
| Γ_{disp} | N/m | mesh stiffness |
| δ | m | mesh displacement |
| ζ | - | damping ratio |
| λ | W/mK^2 | thermal conductivity |
| λ | m | wave length |
| μ | - | mass ratio |
| μ_t | $\text{Pa} \cdot \text{s}$ | turbulence viscosity |
| ν | m^2/s | kinematic viscosity |
| Ξ | - | stability parameter |
| Π_{ν} | $\text{N}/\text{kg m}^2$ | viscous part of the stress tensor |
| ρ_0 | kg/m^3 | density |
| σ | - | interblade phase angle |
| ϕ | - | mode shape |
| $\phi_{\text{p} \rightarrow \text{h}}$ | rad | phase angle of response with respect to excitation (motion); the phase angle is per definition positive if the response is leading the excitation |

ω rad/s angular velocity

Subscripts

ae aerodynamic
 cycle over a complete cycle
 damping related to damping
 disp displacement
 dist distance
 disturbance related to disturbances
 dyn dynamic
 est estimated
 Hub blade hub
 ic influence coefficient
 inlet domain inlet
 ip integration point
 max maximum
 NB number of blades
 ref reference
 Shroud blade shroud
 spec specified
 static absolute quantities
 tot total quantities
 twm traveling wave mode
 vol volume
 wall refers to a wall boundary
 ν viscous
 τ refers to shear stress

Superscripts

* normalized value
 ° degree

Operators, Functions and Symbols

∇ gradient
 $\nabla \cdot$ divergence
 \otimes dyadic product
 \cdot inner product

Abbreviations

| | |
|------|---|
| BCR | blade count ratio |
| CEL | CFX expression language |
| CFD | computational fluid dynamics |
| DOF | degree of freedom |
| FEM | finite element method |
| FFT | Fast Fourier Transformation algorithm |
| GGI | general grid interface connection |
| HCF | high cycle fatigue |
| ICM | Influence Coefficients Method |
| IBPA | inter blade phase angle |
| MAC | modal assurance criteria |
| NFS | Navier-Stokes-Fourier system of equations |
| RMS | root mean square value |
| SST | shear stress transport model |
| TWM | Traveling Wave Mode |

1 Introduction

By virtue of their superior power density (power-to-weight ratio) and flexible operational characteristics, gas turbines still remain to be the prime choice for aircraft propulsion and conventional power generation systems in large-scale and smaller scale applications. Aiming at higher efficiency, improved performance and reliability, lower fuel emissions and more compact designs, modern gas turbines are designed with a tendency towards more aggressive stage loadings, higher temperatures modern light weight materials and slender blade designs with advanced three dimensional shapes. On the other hand however, application of these modern solutions renders unsteady aerodynamic forces and flutter problems which may eventually lead to component failure as a result of excessive stresses or high-cycle fatigue (HCF) induced by limit cycle vibrations.

Flutter denotes a self-excited and self-sustained aeroelastic instability phenomenon that occurs when the aerodynamic forces overcome the structural and inertial forces in slender flexible structures [27]. Thus in a gas turbine, flutter is prone to occur particularly in the fan and the first stages of the compressor, or in the last stages of the turbine where blades with higher aspect ratios are exposed to aggressive blade loadings.

Designing for aeroelastic stability, is therefore one of the key tasks of modern engine designers, in order to guarantee a wide range of flutter-free operating points. Also due to low structural damping, prediction of unsteady aerodynamic forces induced by the oscillation of blades, and their reciprocal influence on the vibration modes, is of an essential importance for an aeroelastically stable design.

In recent years the advent of modern numerical solution techniques such as computational fluid dynamics (CFD) and finite element analysis methods (FEM) along with a substantial increase in computational power during the last decade, has made it possible to develop powerful tools for detailed assessment of the unsteady aerodynamic forces for various blade geometries. However though an exact determination of the aerodynamic damping during the design process with transient CFD simulations is still very time consuming. Furthermore, there are still no specific geometrical design parameters regarding aerodynamic damping, which could help to decrease the number of design iterations in design process of new turbomachines.

The main objective of the present work is to investigate possible correlations between specific geometrical parameters and the aerodynamic damping of an axial compressor rotor. In order to determine the transient CFD setup for the assessment of aerodynamic damping, a numerical influence study has been performed for an isolated rotor concept, representing the subject axial compressor. Subsequently, geometrical parameters have been identified and a baseline rotor blisk has been then modified according to a test matrix of parameters. Once the eigenmodes of the blisks were determined using ANSYS Mechanical APDL, transient CFD simulations have been performed using ANSYS CFX 18 for both "Traveling Wave Mode" approach and the "Influence Coefficients Method".

2 Literature Review

2.1 Basic Principles of Aeroelasticity

Aeroelasticity is an engineering terminology that defines an interdisciplinary field, which deals with the mutual interaction between inertial, elastic and aerodynamic forces. Therefore flow-structure interaction can take place at any elastic structure subjected to a fluid flow [4].

The classic theory of aeroelasticity deals with the stress and deformation of an elastic body under prescribed external forces or displacements. The external loadings acting on the body are, in general, independent of the deformation of the body. It is usually assumed that the deformation is small and does not substantially affect the action of external forces. The situation is different however, in most significant problems of aeroelasticity. The aerodynamic forces depend critically on the attitude of the body relative to the flow. The elastic deformation plays an important role in determining the load itself and conversely the magnitude of the aerodynamic force is not known until the elastic deformation is determined [11].

An in depth study of the fluid-structure interactions did not attain prominent attention until the early stages of the World War II. With the advent of monoplane configurations and increasing airplane speeds however, with little or no increase in load requirements which were placed on aircraft structures by design criteria specifications, aircraft designers encountered a wide variety of problems which are now classified as aeroelastic problems [4].

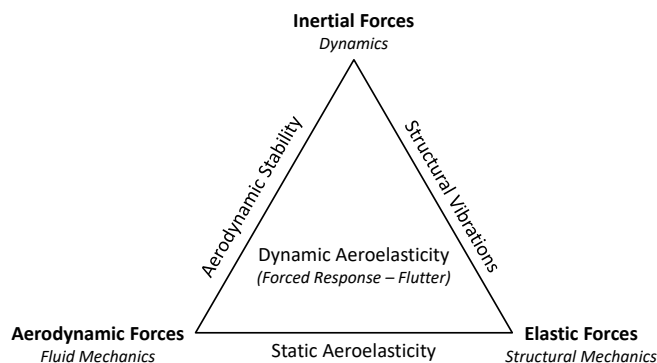


Fig. 2.1 – Collar's triangle of forces, adapted from [4]

A comprehensive study on aeroelasticity was conducted in 1947 by collar, where he has ingeniously classified problems in aeroelasticity by means of a triangle of forces. Referring to Figure 2.1, the three types of forces, aerodynamic, elastic and inertial, are placed

at the vertices of a triangle so that each aeroelastic phenomenon can be located on the diagram according to its relation to the three vertices. Dynamic aeroelastic phenomena such as flutter, lie within the triangle, since they involve all three types of forces, whereas, static aeroelastic phenomena such as divergence, lie outside the triangle, as they involve only aerodynamic and elastic forces.

2.1.1 Static Aeroelasticity

Static aeroelastic phenomena deals with the interaction of aerodynamic and elastic forces as stated in Collar's triangle of forces. By definition, time is not present as an independent variable. This indicates that no vibrations are implied in the phenomena, but that a structure will deform under the steady aerodynamic load [10]. In most of the physical conditions, the system converges to a stable static condition and the related problem is defined as "aeroelastic deformation". It could happen, however, that the deformed shape of the structure leads to an increase of aerodynamic forces resulting in an instability.

Divergence is the most important static aeroelastic instability. This corresponds to a static instability of a lifting surface of an aircraft in flight, at a speed called the divergence speed, where the elasticity of the lifting surface plays an essential role in the instability [4, 9]. Divergence typically affects slender components subjected to high aerodynamic loads such as aircraft wings or wind turbine airfoils. Thus, in turbomachinery applications, the blades are not prone to fail under this phenomena due to the high stiffness values resulting from the influence of high centrifugal loads and mechanical properties of the materials used for blade manufacturing.

2.1.2 Dynamic Aeroelasticity

The terminology "dynamic aeroelasticity" covers the interactions of unsteady aerodynamic forces, elastic forces and inertial forces in Collar's triangle. Depending on the nature of the unsteady flow, instabilities may appear in various forms such as, flutter, forced vibrations, buffeting, galloping, vortex-shedding, buzz, gust, etc. It is worth also noting that, for certain high temperature applications, dynamic thermal stresses may enter the aeroelastic chain, changing the Collar's triangle into a tetrahedron [7, 10].

2.2 Aeroelasticity in Turbomachines

2.2.1 Forced Response

In turbomachinery applications, the relative motion between the rotating and stationary components result in generation of unsteady nonuniform flow fields. The consequent periodic unsteady aerodynamic loads cause a forced vibration of the blades. Flow disturbances in turbomachines are mainly initiated by wake interactions of the different

blade-rows, potential fields of downstream rows or other flow disturbances caused by upstream elements such as inlet guide vanes and combustion chamber burners or the shock waves moving along blade passages [22].

With the relative motion between blade-rows, being the main source of flow disturbances, the frequency of the forcing term is proportional to the rotational velocity. A potential resonance condition featuring a distinct nodal diameter may evolve if the excitation frequency of the forcing term, coincides with the eigen-frequency and the corresponding eigen-mode of the bladed disc. In such cases, the forced response may result in vibration amplitudes which exceed the material fatigue endurance limit, leading to high cycle fatigue (HCF) [20]. Thus in order to avoid failure in case of resonance the overall damping including the hysteretic, frictional and aerodynamic damping must be positive.

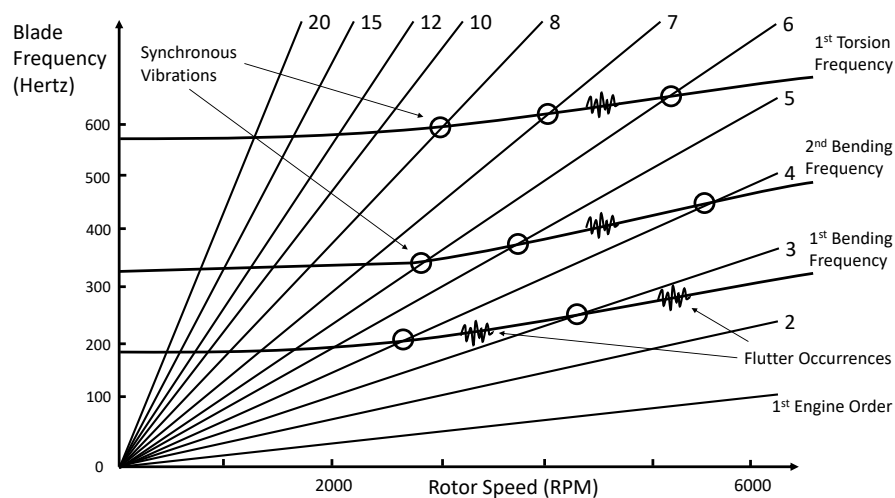


Fig. 2.2 – Campbell diagram indicating the occurrence of flutter, adapted from [27]

The excitation of structural modes in turbomachines, is conveniently assessed by means of a Campbell diagram, such as the one depicted in Figure 2.2, which represents the changes in excitation frequency as a function of the rotational velocity, together with the corresponding engine orders. In this diagram, the horizontal lines represent the eigen-frequencies of the blades. An increase in the rotational speed results in increasing centrifugal forces which cause the natural frequency curves to vary with a positive slope in the Campbell diagram. According to this diagram, crossings of an engine order and a vibration mode indicate possible forced resonance, and crosses indicate either propagating stall, flutter or other non-synchronous excitation [10].

2.2.2 Flutter

Unlike forced vibrations, in case of flutter, flow unsteadiness emerges due to the vibration of the blade itself, rather than an external source. The resulting unsteady aerodynamic forces can be either stabilizing or destabilizing in nature. Flutter denotes a self-excited and self-sustained aeroelastic instability phenomenon that occurs when the aerodynamic forces overcome the structural and inertial forces. Flutter phenomena will

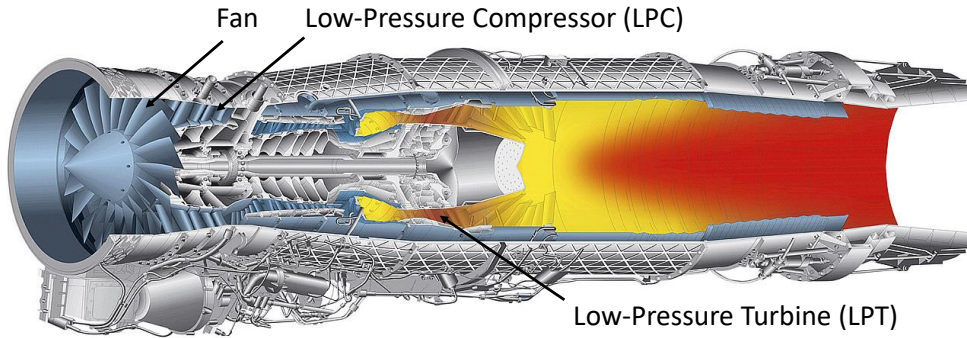


Fig. 2.3 – Cross-section of a EuroJet EJ200 low bypass turbofan engine [18]

evolve in case the fluid is feeding energy into the structure leading to larger vibration amplitudes and consequently to even larger aerodynamic forces which may eventually lead to component failure as a result of excessive stresses or high-cycle fatigue (HCF) [27].

In turbomachines, flutter is prone to occur particularly in slender flexible components such as the fan or the low pressure compressor (LPC) and low pressure turbine (LPT) in a gas turbine, where blades with higher aspect ratios are exposed to aggressive blade loadings. Figure 2.3 depicts a modern aero-engine denoting the components which are more susceptible to flutter.

The classical type of flutter is associated with potential flow and usually, but not necessarily, involves the coupling of two or more degrees of freedom. The non-classical type on the other hand, may involve separated flow or stalling conditions, which is difficult to analyze on a purely theoretical basis [4].

Instability problems on wing structures, appeared when aircraft designers abandoned biplane construction with high torsional rigidity, in favor of monoplane types [4]. Thereafter, it was quickly observed that the mass ratio was the main stability parameter determining the onset of the wing flutter occurrence. The mass ratio, μ , is defined as the ratio of the mass of the wing or blade to the mass of the surrounding air enclosed in a circle which has a diameter equal to the chord length [27]. In equation 2.1, m denotes the mass per unit wing span, ρ_0 is the air density and c is the chord length.

$$\mu = \frac{4m}{\pi \cdot \rho_0 \cdot C^2} \quad (2.1)$$

In case of aircraft wings, a smaller mass ratio indicates a higher probability of flutter occurrence. In turbomachines though the mass ratio attains higher values and is no more an appropriate criteria for analyzing flutter instabilities. Meldahi suggested that in turbomachine blade-rows flutter appears above certain flow velocities and thus introduced the “reduced frequency” as a criteria for determining the onset of flutter phenomena [27]. The reduced frequency k relates the time of the flight for a fluid particle needed to travel across blade chord to the vibration period and is defined as

$$k = \frac{t}{T} = \frac{2\pi \cdot f \cdot C}{u} \quad (2.2)$$

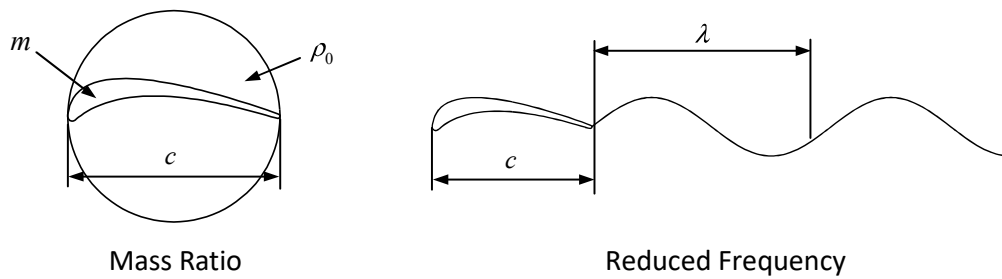


Fig. 2.4 – Graphical interpretation of mass ratio and reduced frequency, [27]

where f is the vibration frequency, C is the chord length and u is the flow velocity (usually the reference velocity is the upstream velocity for compressors and downstream velocity for turbines). It is possible to further elaborate on equation 2.2, in order to obtain the reduced frequency as a ratio of the blade chord and the wave length.

$$\lambda = \frac{u}{\omega} = \frac{u}{2\pi f} \rightarrow k = \frac{C}{\lambda} \quad (2.3)$$

Figure 2.4, represents a graphical interpretation of the mass ratio and reduced frequency. For turbomachine blade-rows, critical reduced frequencies have been reported in a range between 0.1 and 1.0. Fleeter and Jay, have presented an example of the reduced frequency span for axial-flow turbomachines, under which flutter has been witnessed. Srinivasan reports similar values pointing out that flutter occurrences in the first mode have been observed for reduced frequencies less than 0.4 and between 0.4 and 0.7 for modes with predominantly first torsion mode [10, 22].

Table 2.1 – Typical flutter reduced frequency ranges, [10]

| Type of Flutter | Reduced Frequency k |
|------------------------------------|-----------------------|
| Unstalled supersonic torsion | 0.35 -> 0.65 |
| Supersonic bending | 0.1 -> 0.25 |
| Subsonic/transonic torsional stall | 0.2 -> 0.8 |
| Choke bending | 0.15 -> 0.25 |

Table 2.2 – Values of reduced frequency for which flutter has been observed, [22]

| | | |
|--------------------|-------------|---------------------|
| P&W Research Rotor | 0.4 to 0.6 | (Mikolajczak, 1975) |
| TS 22 | 0.6 to 0.65 | (Stargardter, 1979) |
| NASA Test Rotor | 0.5 to 0.7 | (Kielb, 1983) |
| NASA Engine Tests | 0.7 to 0.75 | (Lubomski, 1980) |
| First Fan Rotor | 0.7 | (Kurkov, 1984) |

2.2.3 Compressor Flutter Map

In compressors, flutter may appear in several regions of the characteristics map due to different physical reasons. Such instabilities may occur either on the working line or at the off-design conditions but still below the surge line, thus being of primary importance. The most important flutter domains on a typical compressor map are illustrated on Figure 2.5 which has been established empirically throughout the years on blades of conventional materials and shapes and does not necessarily follow that it must be identical in nature when more advanced airfoil shapes and materials are employed [10].

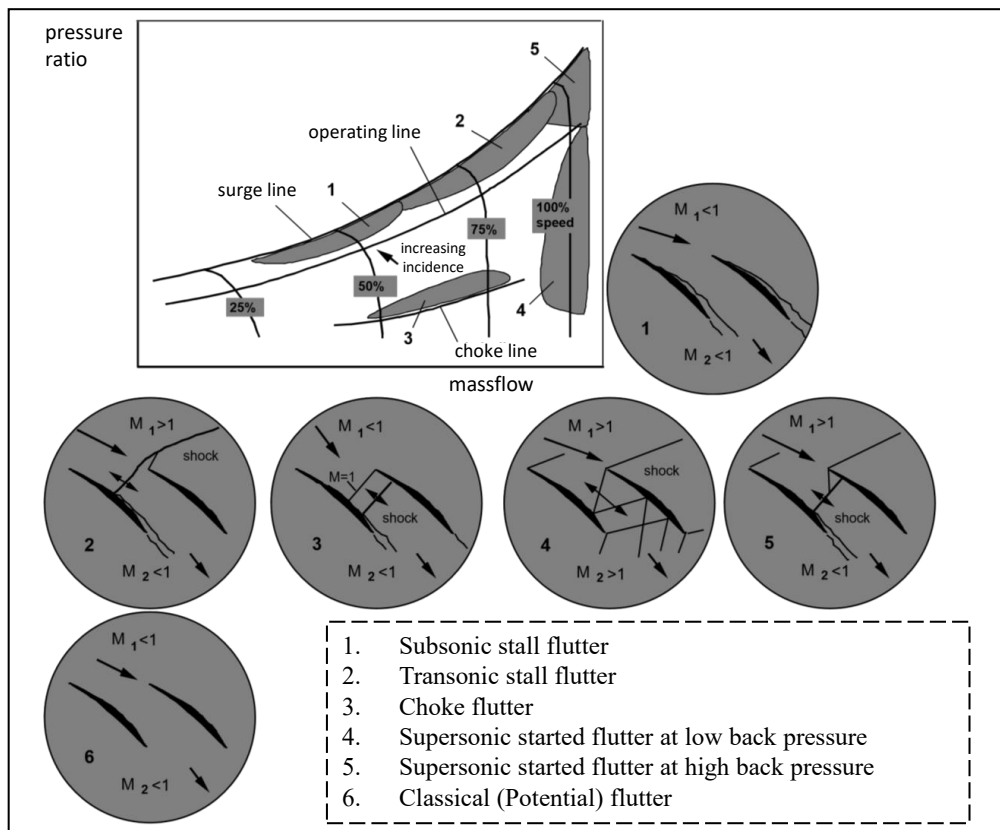


Fig. 2.5 – Compressor flutter map, [10]

Classical (Potential) Flutter: This is usually defined as flutter when the flow is attached at all times and involves directly the phase lag between the movement of blade and induced time-dependent aerodynamic forces, which can be either stabilizing or destabilizing, depending on the value of the time lag.

Stall Flutter: As the name indicates, this type of flutter is situated close to the stall line of the compressor map, and it is thus usually believed that the flow is stalled, or at

least largely separated. This is an essentially non-linear phenomena that is characterized by an abrupt decrease in the flutter speed as the flow becomes stalled.

Choke Flutter: This type of flutter evolves near the choke line of axial-flow compressors (at negative incidences and part speed conditions) and is probably characterized by choked flow, separations and shock waves. Choke flutter may involve either the bending or torsional mode of the blades.

Supersonic Unstalled Flutter: A type of classical flutter that appears in the supersonic flow regions. In the compressor map, this kink of flutter is associated with a low back pressure and usually involves a torsional mode, thus being sometimes referred to as “supersonic torsional flutter”.

Supersonic Flutter at High Back Pressure: By increasing back pressure, the shock waves will move up the blade. This type of flutter is probably accompanied by a strong in-passage shock wave, together with a boundary layer separation and usually involves a bending mode, thus being called “supersonic bending flutter”.

2.2.4 Acoustic Resonance

Acoustic resonance is an aeroelastic problem which amounts to the influence of adjacent space upstream or downstream of the blade row. In such a phenomena, the unsteady pressure field which arises due to the oscillation of the blades, can induce acoustic resonance in the adjacent ducts. In fact acoustic resonance adds one degree of freedom to the aeroelastic system, which might be effective for extraordinary coupling of blades during flutter [27]. Although the acoustic waves may resonate and propagate in annular ducts, significant amplitudes will only appear if there is an excitation source such as vortex shedding which feeds energy into the perturbation [10].

2.3 Aerodynamic Damping

In modern gas turbines in order to achieve higher efficiencies and more compact designs, blades are designed with more aggressive stage loadings and thus more slender geometries with advanced three dimensional shapes. As a result the eigen-frequencies have decreased and it has become necessary to control the mode shapes without significantly affecting the overall weight of the blade [10].

Experimental investigation on turbojet engine blade damping by Srinivasan et al, indicate that material (hysteric) damping is negligible for turbomachine blades as the dissipated energy during an oscillation cycle is very low due to high stiffness of the materials [23]. Mechanical or friction damping, is an alternative source of damping which can be achieved by introducing part-span shrouds (also called snubbers or clappers) on fan blades, and shrouds, part-span shrouds or lacing wires on turbine blades. However though such devises introduce both an additional weight and a mechanical coupling between the different blades of the rotor [10]. It is also worth noting that, investigations

by Kielb and Abhari has showed, that the mechanical and the material damping are inversely proportional to the square of the rotational speed due to a decline in friction as the speed increases [13]. In this regard, aerodynamic damping plays an important role in the overall damping of the system. It is worth noting that for the integrated bladed rotors (blisks), with material damping being of negligible order, aerodynamic damping is the only significant source of damping present in the system.

Depending on the phase-lag between the vibrating blade and the unsteady aerodynamic forces acting on it, the structure will either absorb energy from the flow, or inversely feed energy to the flow. In case of positive aerodynamic damping, the aerodynamic forces will impel a stabilizing effect, limiting the amplitude of maximum displacement. In general, the way the structure behaves over a certain period of time depends thus on the unsteady characteristics of the fluid and the structure over several vibration cycles [10].

2.3.1 Aeroelastic Equation of Motion

From theoretical point of view the motion of a vibrating structure within a fluid flow can be described by the aeroelastic equation as [27]

$$[M] \{\ddot{X}\} + [C] \{\dot{X}\} + [K] \{X\} = \{F_{ae}(t)\} \quad (2.4)$$

where $[M]$ denotes the modal mass matrix, $[C]$ is the modal damping matrix, $[K]$ is the modal stiffness matrix, and $\{X\}$ represents the modal coordinates. The right hand side of the equation 2.4 includes unsteady modal forces which can be decomposed as follows

$$F_{ae}(t) = F_{damping}(t) + F_{disturbance}(t) \quad (2.5)$$

In equation 2.5, $F_{damping}(t)$ represents the aerodynamic damping force induced by the blade oscillations, whereas $F_{disturbance}(t)$ denotes the aerodynamic forcing arising from spatial non-uniformities of the upstream and downstream flow fields. In case of flutter analysis, only the forces induced by the blade motion are of interest and thus the right hand side of the equation 2.5 simplifies to $F_{ae}(t) = F_{damping}(t)$.

In order to solve the aeroelastic equation, a modal coordinate system is introduced as

$$\{X(t)\} = [\phi] \{\bar{Q}\} e^{i\omega t} \quad (2.6)$$

where ω denotes the frequency, \bar{Q} is the modal displacement and ϕ represents the mode shape. Thus the equation 2.4 can be further elaborated as

$$\left\{ -\omega^2 [M_m] + i\omega [C_m] + [K_m] - [\phi^*]^T [A] \right\} \{\bar{Q}\} = 0 \quad (2.7)$$

In equation 2.7, matrix $[A]$ contains the modal unsteady aerodynamic forces. This equation represents a complex eigenvalue problem the solution of which describes the stability of the system.

2.3.2 Aerodynamic Coupling

In contrast to airplane wings, where flutter is driven by a mode coalescence phenomena, flutter problems in turbomachines involve influences of neighboring blades rather than a single blade as a result of close spacing between blades. The motion of each single blade is influencing instantaneously the flow field in its direct neighborhood inducing a response on itself and on its direct neighbors as depicted in Figure 2.6. This phenomenon is referred to as aerodynamic coupling [24, 27].

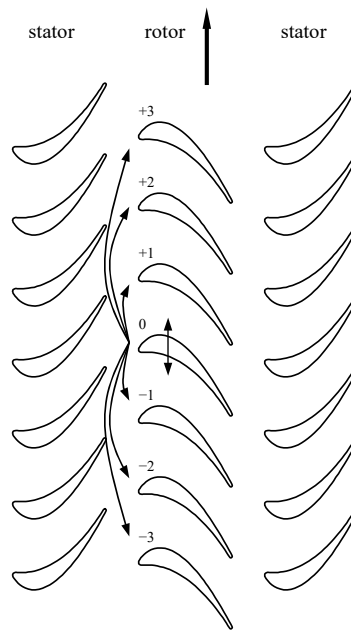


Fig. 2.6 – Graphical representation of aerodynamic coupling, [27]

According to a traditional approach suggested by Crawley, provided that all the blades in a rotor are identical and equally spaced (perfectly tuned rotor), the oscillatory motion of a blade row at the onset of flutter can be characterized as a traveling wave mode. In other words, in a tuned blade row, all the blades oscillate in the same mode, amplitude and frequency but with a certain phase lag between two adjacent blades which is referred to as “Interblade Phase Angle” (IBPA) [27]. Due to the kinematic constraints, interblade phase angle can only take discrete values so as to fulfill full cycle periodicity and is therefore defined as

$$\sigma = \frac{2\pi \cdot l}{N_{\text{NB}}}, \quad l = 1, 2, 3, \dots, l_{\text{max}} \quad (2.8)$$

for forward traveling wave modes and

$$\sigma = 2\pi \left(\frac{N_{\text{NB}} - l}{N_{\text{NB}}} \right), \quad l = 1, 2, 3, \dots, l_{\text{max}} \quad (2.9)$$

for backward traveling wave modes.

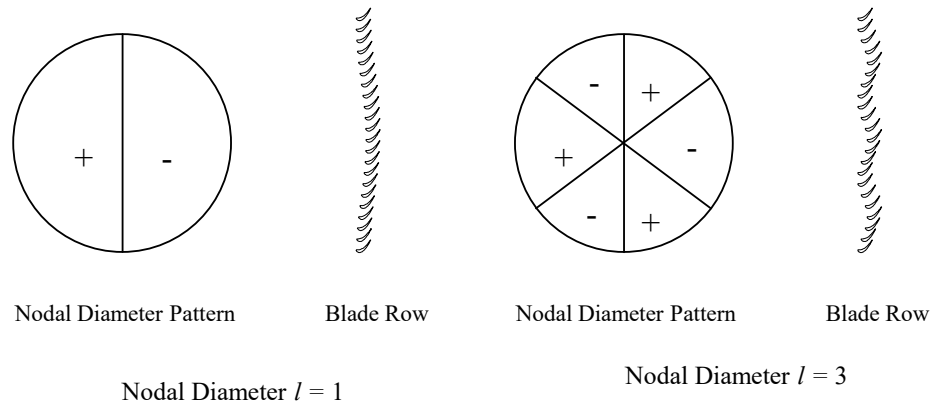


Fig. 2.7 – Graphical representation of nodal diameters of a disk, traveling wave mode shapes and the corresponding instantaneous blade row geometry, [27]

In equations 2.8 and 2.9, N denotes the number of blades, whereas l represents the “nodal diameter” which defines the order of the traveling wave. Depending on the total number of blades, the maximum nodal diameter is calculated as

$$l_{\max} = \begin{cases} \frac{N_{\text{NB}}}{2} & N_{\text{NB}} = \text{even} \\ \frac{N_{\text{NB}}-1}{2} & N_{\text{NB}} = \text{odd} \end{cases} \quad (2.10)$$

An example of nodal diameter patterns and the corresponding cascade geometries is depicted in Figure 2.7

2.3.3 Traveling Wave Mode Approach

As mentioned previously, the two major differences that separate aeroelastic phenomena on aircraft wings and turbomachine blades are the mass ratio and aerodynamic coupling effects. Regarding the aeroelastic equation of motion, the structural terms are substantially larger compared to the aerodynamic damping term as a result of the high mass ratios. The practical implication of this is that the structural and aerodynamic parts can be decoupled, which results in great simplification of the aeroelastic problem. Consequently it is possible to determine the structural eigen-modes without considering the flow interactions (i.e. in vacuum), while the influence of aerodynamic forces on stability, can be determined through an unsteady flow analysis over a cascade of blades oscillating in an arbitrary or prescribed motion [10, 27].

Oscillatory motion of blades generate an unsteady pressure disturbance which propagates in the surrounding flow field. The work per oscillation cycle exerted by the fluid on the blade profile, can be introduced as a stability criteria in such a manner that if the overall work performed by the unsteady flow on the structure is positive, the situation is referred to as unstable. Verdon, has established that, in case of small perturbations, the unsteady pressure field resulting from the harmonic motion of the blade, is also har-

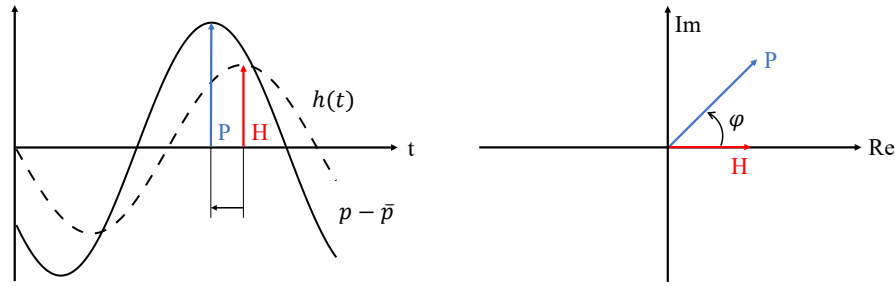


Fig. 2.8 – Phase shift between blade motion and unsteady pressure perturbation [17]

monic in time, with the same frequency, but with a phase shift to the motion. Thus the unsteady pressure can be represented as a harmonic oscillation around a mean value as

$$p(x, y, z, t) = \bar{p}(x, y, z) + \tilde{p}(x, y, z, t) = \bar{p}(x, y, z) + \hat{p} \cdot e^{i(\omega t + \phi_{p \rightarrow h})} \quad (2.11)$$

Equation 2.11 is the sum of a mean value corresponding to the steady pressure distribution $\bar{p}(x, y, z)$ and a time-dependent fluctuating part $\tilde{p}(x, y, z, t)$ with a complex perturbation amplitude equal to \hat{p} . Figure 2.8 is a graphical demonstration of the phase shift between harmonic motion of the blade and its resulting harmonic unsteady pressure, both in time domain and frequency domain representation. Similarly the instantaneous unsteady aerodynamic force will be harmonic as well and thus can be written as \hat{F} which yields from integration of the product of unsteady pressure and blade velocity over blade surface area.

Consequently the corresponding work per oscillation cycle is obtained by integrating the product of force and velocity over a period of oscillation [27].

$$W_{\text{cycle}} = \int_T \int_S \tilde{p} \vec{v} \cdot \vec{n} \, ds \, dt = \int_T \tilde{F} \vec{v} \, dt = \int_T \hat{F} \vec{v} e^{i\omega t} \, dt \quad (2.12)$$

In equation 2.12, \vec{v} denotes the velocity of the moving blade, S is the blade surface area and \vec{n} represents the local normal vector. After integration, with \hat{h} representing the complex motion of the blade, the expression for work per cycle simplifies to

$$W_{\text{cycle}} = \pi \cdot \left| \hat{F} \right| \cdot \left| \hat{h} \right| \cdot \sin(\phi_{F \rightarrow h}) \quad (2.13)$$

According to equation 2.13, the phase shift between force and blade motion, indicates the fact that only the imaginary part of the complex force is contributing to the overall work per cycle. As a result, the flow will induce a stabilizing influence, if the response is lagging the excitation, or in other words if the imaginary part has a negative contribution.

Verdon introduced a normalized stability parameter, referred to as “aerodynamic damping” which measures the negated work per cycle normalized by the oscillation amplitude h , π , span height of the blade b , and the dynamic pressure p_{dyn} [25, 28]. Thus a positive aerodynamic damping indicates that the flow is acting in a stabilizing manner.

$$\Xi = \frac{-W_{\text{cycle}}}{\pi \cdot b \cdot p_{\text{dyn}} \cdot h^2} \quad (2.14)$$

2.3.4 Influence Coefficients Method

In case of a perfectly tuned rotor oscillating in a traveling wave mode, the same unsteady pressure field will be generated around each blade, but with a phase shift equal to σ (IBPA) with respect to the neighboring blade. The practical implication of this fact is that by measuring the flow field around a reference blade, the the unsteady pressure filed around all the blades on the same blade-row can be determined. However from experimental point of view, implementation of this method is quite complex since it requires all the blades to be oscillated with a specific frequency and a certain inter-blade phase angle [8, 27].

Hanamera et al. and Crawley, have suggested another method referred to as “Influence Coefficients Method”, which is based on the linear superposition principle. Assuming that the perturbations are small, the total unsteady response on a blade includes the responses of the reference blade itself and of the other blades lagged by the respective multiple of the interblade phase angles. Thus the response in traveling wave mode at a reference blade in a cascade of $N + 1$ blades is stated as

$$\hat{p}_{A,twm}^{m,\sigma}(x,y,z) = \sum_{n=-\frac{N}{2}}^{n=+\frac{N}{2}} \hat{p}_{A,ic}^{n,m}(x,y,z) \cdot e^{-i\sigma n} \quad (2.15)$$

In equation 2.15, $\hat{p}_{A,twm}^{m,\sigma}(x,y,z,t)$ denotes the complex pressure coefficient at point (x,y,z) , acting on blade m with the cascade oscillating in traveling wave mode with an interblade phase angle of σ . Meanwhile, $\hat{p}_{A,ic}^{n,m}(x,y,z,t)$ is the pressure coefficient of the vibrating blade n , acting on the non-vibrating reference blade m at point (x,y,z) . The coefficients $\hat{p}_{A,ic}^{n,m}$ are commonly referred to as local aerodynamic influence coefficients.

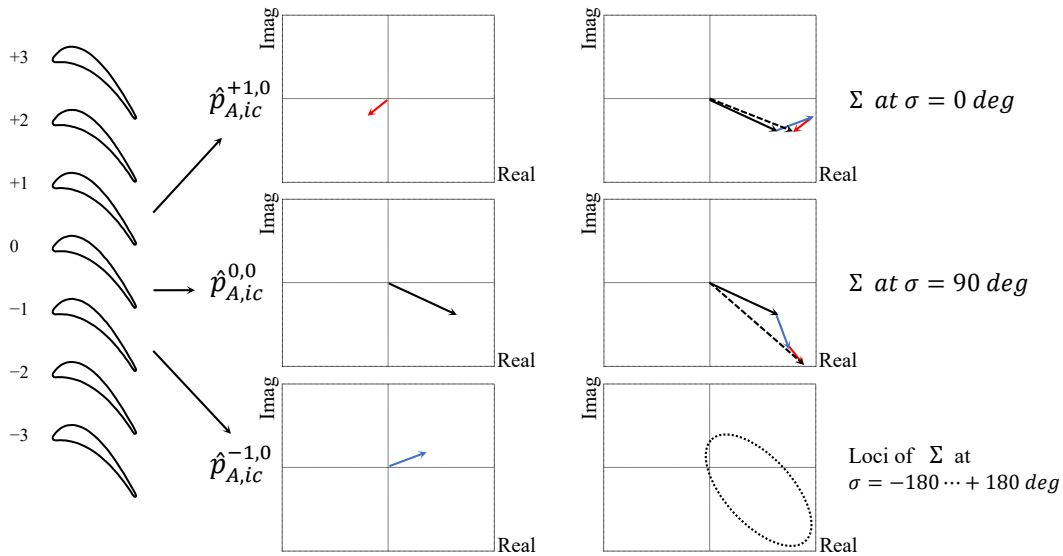


Fig. 2.9 – Superposition of the influence coefficients from blades -1 and +1 on blade 0 for $\sigma = 0$ and $\sigma = 90^\circ$, [27]

Equation 2.15 highlights the impact of inter-blade phase angle on the magnitude and phase of the overall traveling wave mode response as graphically depicted in Figure 2.9. In this figure, the complex pressure is represented by a vector with the length corresponding to its magnitude, which is oriented according to the phase shift with respect to the blade motion. The influence coefficients are depicted on the left-hand side whereas the superposition is shown for two different interblade phase angles on the right hand site. In addition the loci of all possible combinations are included as well.

According to equation 2.15, the reference blade (index $n = 0$) has a constant contribution to the summation, meanwhile the neighboring blades induce a harmonically varying contribution whose order increase moving away from the reference blade. (i.e. first harmonic for blades ± 1 , second harmonic for blades ± 2 ...) On the other hand previous studies dealing with coupling effects during cascade flutter, such as Széchényi, Crawley or Nowinski and Panovsky, have all concluded that with increasing distance from the reference blade, the influence decreases rapidly and attains convergence after blade pair ± 2 [8, 24, 27]. It is worth noting that the variation of stability parameter Ξ as a function of interblade phase angle (IBPA), represent a characteristic curve which, in literature, is usually referred to as S-Curve. An example of a typical S-Curve is shown in Figure 2.10.

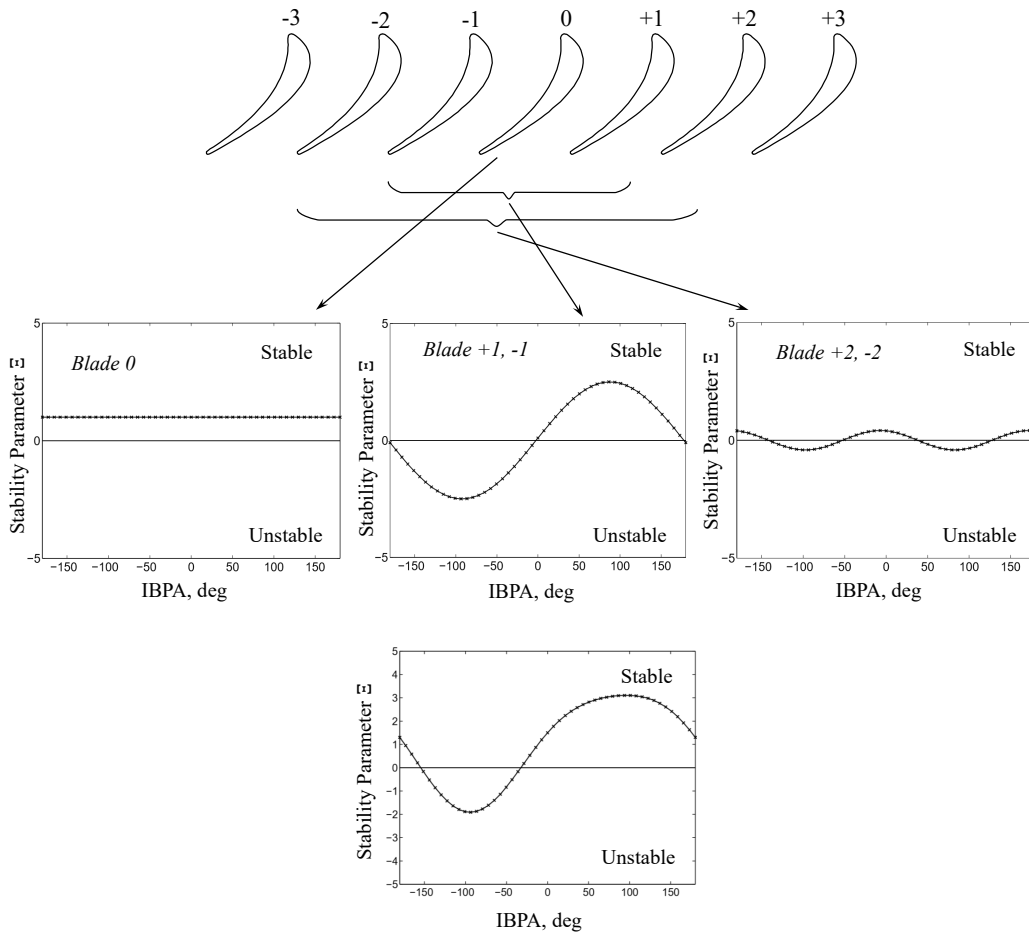


Fig. 2.10 – An example of a typical S-Curve, along with a schematic contribution of blade pairs on overall stability parameter, [27]

2.3.5 Influence of Incidence Angle and Mode Shapes

The flow incidence angle is an important parameter affecting the aeroelastic stability. An increase in incidence angle usually leads to separated flow conditions around the leading edge. Generally several studies on the influence of incidence angle such as Carta and St.Hilaire have concluded that higher values of incidence lead to a reduction in aerodynamic stability and consequently lower values for critical reduced frequency [10].

Additional to the reduced frequency and incidence angle, mode shape has a dominant influence on the aeroelastic stability. In general mode shapes of a bladed disk depending on its structural setup, can be either disk-dominated or bladed-dominated. In a simplified model, unshrouded disk blades can be modeled as a beam with its three mode shapes with the lowest frequency, being of greatest interest for stability analysis. Panovsky and Kielb, have created a preliminary design tool so called “Tie-Dye” plots, that assesses the aeroelastic stability on a two-dimensional section of a cascade. This method represents any generic mode as a rigid-body rotation of the reference section about a center of torsion resulting in a stability map [27].

An example of a stability map is depicted in Figure 2.11 Each center of torsion position of the reference blade gives a different aerodynamic damping. The areas with positive aerodynamic damping indicate that a torsion axis (of the reference blade) situated in this region gives a damped blade vibration. It is noted that certain regions have high gradients, whereas the gradients are lower at other places.

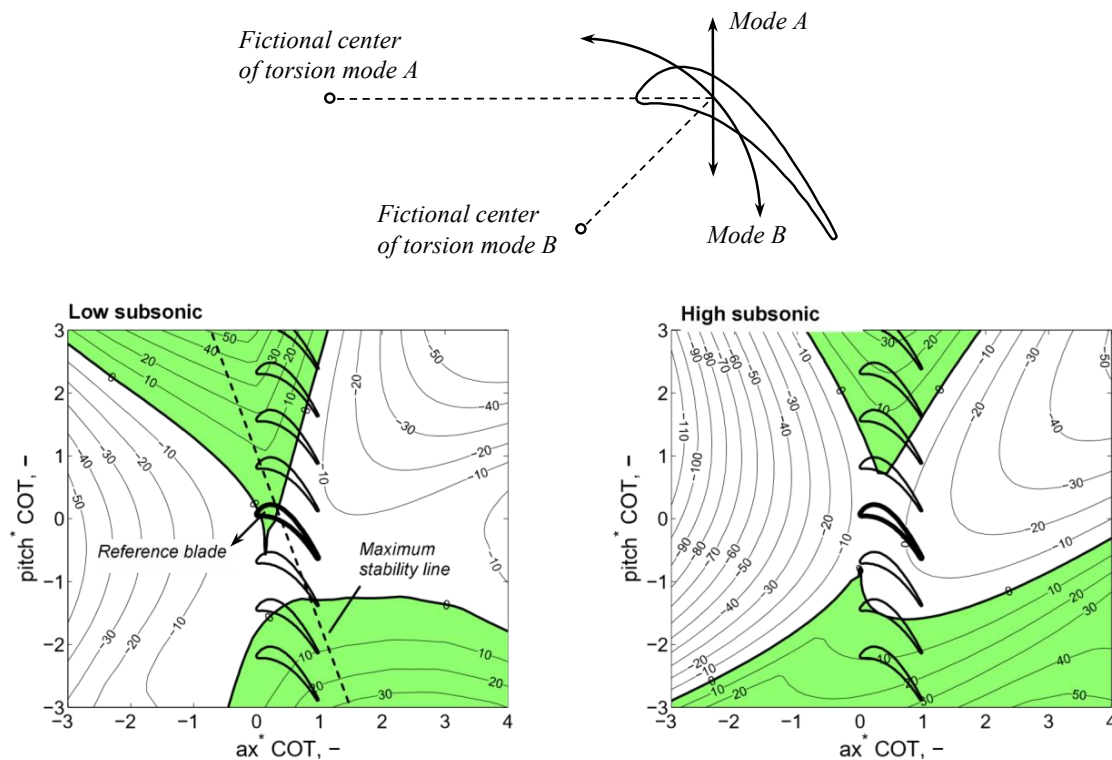


Fig. 2.11 – Torsion mode representation of rigid-body modes along with an example of stability plots for a LPT cascade at different operating conditions, [27]

2.4 Governing Equations

An aeroelastic problem involves two different engineering principles, namely fluid dynamics and structural mechanics. While the fluid dynamics equations are typically defined using spatial coordinates (Eulerian reference frame), the structural dynamics equations are usually formulated using material coordinates (Lagrangian reference frame).

2.4.1 Basic Principles of Computational Fluid Dynamics

The following section is based on the lecture notes of Professor Pietro Asinari of Politecnico di Torino [3] and outlines briefly the basic principles and governing equations of computational fluid dynamics.

Computational Fluid Dynamics (CFD) is a computer-aided tool for analysis of systems involving fluid flow, heat transfer, and associated physical processes such as chemical reactions. In general CFD tools utilize numerical solution techniques such as finite element or finite volume methods in order to solve the governing equations of fluid dynamics with specified boundary conditions over a discretized domain through an iterative procedure.

Mass Conservation

The net mass flux at the border of an arbitrary control volume such as the one depicted in Figure 2.12, will determine a rate of change of the mass accumulated inside the control volume. Mass conservation equation can be derived by performing a mass balance over the domain Ω as

$$\frac{\partial m_{\Omega}}{\partial t} = \frac{\partial}{\partial t} \int_{\Omega} \rho dV = - \oint_{\partial\Omega} \rho \mathbf{u} \cdot \hat{\mathbf{n}} dS \quad \rightarrow \quad \frac{\partial \rho}{\partial t} + \nabla \cdot (\rho \mathbf{u}) \quad (2.16)$$

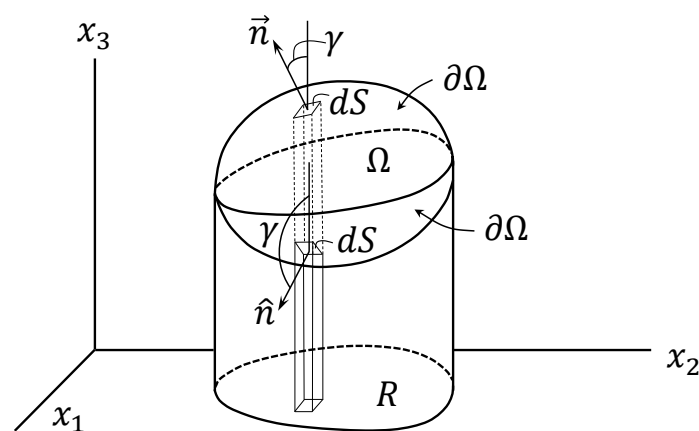


Fig. 2.12 – An arbitrary control volume, [3]

Momentum Conservation

Equation 2.17 yields the integral momentum equation, with u_Ω being the barycentric velocity in Ω . In this case, the velocity streams itself (by advection) which is a source of nonlinearity.

$$\begin{aligned} u_\Omega &= \frac{1}{m_\Omega} \int_\Omega \rho u dV \quad \rightarrow \quad \frac{\partial(m_\Omega u_\Omega)}{\partial t} = \frac{\partial}{\partial t} \int_\Omega \rho u dV = - \oint_{\partial\Omega} F(\rho u) \cdot \hat{n} dS + \int_\Omega s(\rho u) dV \\ &\quad \rightarrow \quad \frac{\partial(\rho u)}{\partial t} + \nabla \cdot (\rho u \otimes u) + \nabla p = \nabla \cdot \Pi_v + \rho a \end{aligned} \quad (2.17)$$

where a represents any external force acting on the system and Π_v denotes the viscous stress tensor as

$$\Pi_v = \rho \nu \left(\nabla u + \nabla u^T - \frac{2}{3} \nabla \cdot u I \right) \quad (2.18)$$

Total Energy Conservation

The total energy conservation equation is derived from the first law of thermodynamics. Considering the Reynold's transport theorem the integral total energy conservation equation can be expressed as

$$\begin{aligned} \frac{\partial(m_\Omega e_t)}{\partial t} &= \frac{\partial}{\partial t} \int_\Omega \rho e_t dV = - \oint_{\partial\Omega} f(\rho e_t) \cdot \hat{n} dS \\ &\quad \rightarrow \quad \frac{\partial(\rho e_t)}{\partial t} + \nabla \cdot (\rho e_t u + p u) = \nabla \cdot (-q_\alpha + \Pi_v \cdot u) \end{aligned} \quad (2.19)$$

where q_α denotes the thermal flux which according to Fourier law, can be expressed as

$$q_\alpha = -\lambda \nabla T = -\rho c_p \alpha \nabla T \quad (2.20)$$

Equations 2.16, 2.17 and 2.19 form a non-linear system of partial differential which is called the Navier-Stokes-Fourier (NFS) system of equations, that are in general considered to be capable of describing Newtonian turbulent viscous flows.

Turbulence Models

In order to model turbulent flows in CFD, an appropriate turbulence model is required to close the NFS system of equations. For most of the engineering purposes, it is unnecessary to resolve details of the turbulent fluctuations, and usually the effects of turbulence on the mean flow are only considered. Thus it is possible to develop Reynolds-averaged Navier-Stokes equations (RANS) for the mean value of flow variables by taking a time average of these variables over a sufficiently long period compared to the frequency of turbulent fluctuations [26].

2.4.2 Structural Dynamics Analysis

Dynamic analysis of bladed discs can be performed using Finite Elements Method (FEM), which is in general a discretization method for solution of partial derivative differential equations. FEM is based on subdivision of the structure into finite elements, such as beam elements, shell elements, plate elements and etc. Therefore this method yields models with a large number of degrees of freedom with DOFs being the displacements at nodes of each element [12].

The equation of motion for the finite element representation of a structure can be written as

$$[M] \{\ddot{X}\} + [C] \{\dot{X}\} + [K] \{X\} = \{F(t)\} \quad (2.21)$$

The undamped homogeneous form of equation 2.21 represents free vibration problem of the structure, which yields the following eigen-value problem.

$$\omega^2 [M] \{\bar{X}\} = [K] \{\bar{X}\} \quad (2.22)$$

The resulting set of n eigenvalues ω_n and eigenvectors $\{\phi_n\}$, yield the undamped natural frequencies and natural modes or mode shapes of the structure. According to the expansion theorem, using m modes for the n DOF system, the displacements vector can be written as

$$\{u(t)\} = [\Phi] \{q(t)\} \quad (2.23)$$

In equation 2.23, $[\Phi]$ is the $n \times m$ modal matrix which includes the undamped eigenvectors $\{\phi_n\}$, whereas the vector $\{q(t)\}$ is the time-dependent modal coordinate vector. Substituting equation 2.23 into the original equation of motion and premultiplying by the transpose of the modal matrix, the modal equation of motion is obtained as

$$[M_m] \{\ddot{q}\} + [C_m] \{\dot{q}\} + [K_m] \{q\} = [\Phi]^T \{F(t)\} = \{Q(t)\} \quad (2.24)$$

With $[M_m]$, $[C_m]$ and $[K_m]$, being respectively the $m \times m$ generalized mass, damping and stiffness matrices, equation 2.24, represents a system of m equations. Due to the orthogonality of mass and stiffness matrices, the generalized mass and generalized stiffness matrices are diagonal. The generalized damping matrix can be modeled by an equivalent modal damping, in order to obtain diagonal matrix. Meanwhile the expression at the right hand side of equation 2.24, is referred to as generalized force vector $\{Q(t)\}$. The modal form of the equation of motion, represents a system of m uncoupled, second-order ordinary differential equations.

3 Objectives and Approach

In the perspective of experimental and numerical studies related to aeroelasticity, the blade geometry has often been considered as given, which means that the aeroelastic considerations have traditionally been introduced late in the design phase. Geometrical parameters of a blade determine the vibration frequency and mode shapes, thus directly influence the aeroelastic stability of the system. Due to the fact that modifications to the geometrical parameters are inconvenient to be applied late in the design process, the present knowledge regarding the influence of such parameters on aeroelastic response of a specific blade geometry is still very limited.

However, in recent years with the aid of modern numerical solution techniques such as computational fluid dynamics (CFD) and finite element analysis methods (FEM) along with a substantial increase in computational power it has been made possible to perform a detailed assessment of the unsteady aerodynamic forces for various blade geometries during the design process. The main objective of the present work is to investigate possible correlations between specific geometrical parameters and the aerodynamic damping of an axial compressor rotor, which could help to decrease the number of design iterations.

A decoupled treatment of aerodynamic and structural parts of the aeroelastic problem is possible in turbomachinery applications, since the mass ratio is substantially high. The main advantage of this approach is the fact that any method can be used for predicting the motion of the structure and unsteady aerodynamic forces. In this study, assuming blade dominated modes for the rotor, modal analysis is performed using ANSYS Mechanical APDL, for a set of various rotor geometries realized in BladeGen and ANSYS DesignModeler.

A structured CFD mesh including an isolated rotor concept has been realized in Numeca AutoGrid, which has been subjected to a numerical influence study with the aim of determining the proper setup for the subsequent CFD simulations. ANSYS CFX 18, which is a transient Navier-Stokes solver, has been used to predict the aerodynamic damping of the subject axial compressor blisk for both “Traveling Wave Mode” approach and the “Influence Coefficients Method”. Figure 3.1, is representation of the overall work-flow that is carried out in present study.

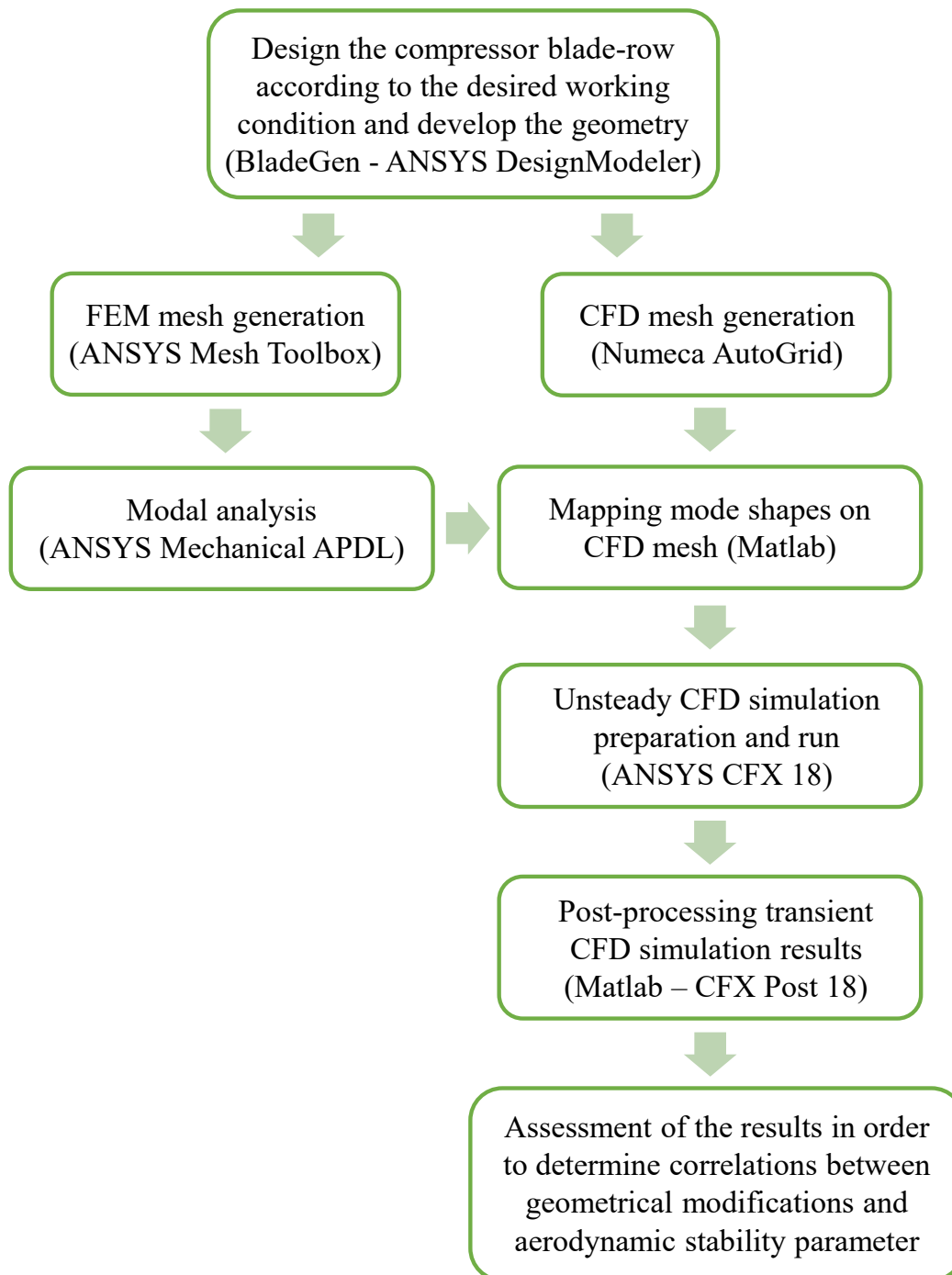


Fig. 3.1 – Graphical representation of the overall work-flow

4 Baseline Rotor Design

The baseline bladed rotor subjected to present investigation, is an axial compressor blisk, comprised of 17 blades, that has been designed at the Institute of Thermal Turbomachinery and Machinery Laboratory (ITSM), University of Stuttgart, with profiles designed according to the free-vortex theory. An unshrouded geometry with integrated design (blisk), has been chosen for this study in order to eliminate mechanical coupling between the blades and to have minimum mechanical and frictional damping effects. The blisk, which is rotating at 16200 RPM, is made of stainless steel with the blade profiles being stacked on their centroid in order to avoid twisting of blades due to the centrifugal forces.

The rotor blisk along with its geometrical parameters is illustrated in Figure 4.1. A summary of the blade profile parameters, operating condition and material properties are represented in Tables 4.3, 4.1 and 4.2.

Table 4.1 – Summary of compressor design parameters

| Parameter | Value |
|-----------------------|---------------|
| Rotational Speed | 16200 [rpm] |
| Mass Flow Rate | 2.2 [kg/s] |
| Inlet Pressure | 97 [KPa] |
| Inlet Temperature | 294 [K] |
| Efficiency | 0.867 |
| Power | 23.3782 [kW] |
| Torque | 13.7806 [N m] |
| Mean Flow Coefficient | 0.43416 |

Table 4.2 – Summary of material properties (17-4 PH Stainless Steel), [5]

| Parameter | Value |
|-----------------------|---------------------------------------|
| Density | 7.8×10^9 [kg/m] ³ |
| Modulus of Elasticity | 200×10^3 [MPa] |
| Poisson's Ratio | 0.272 |

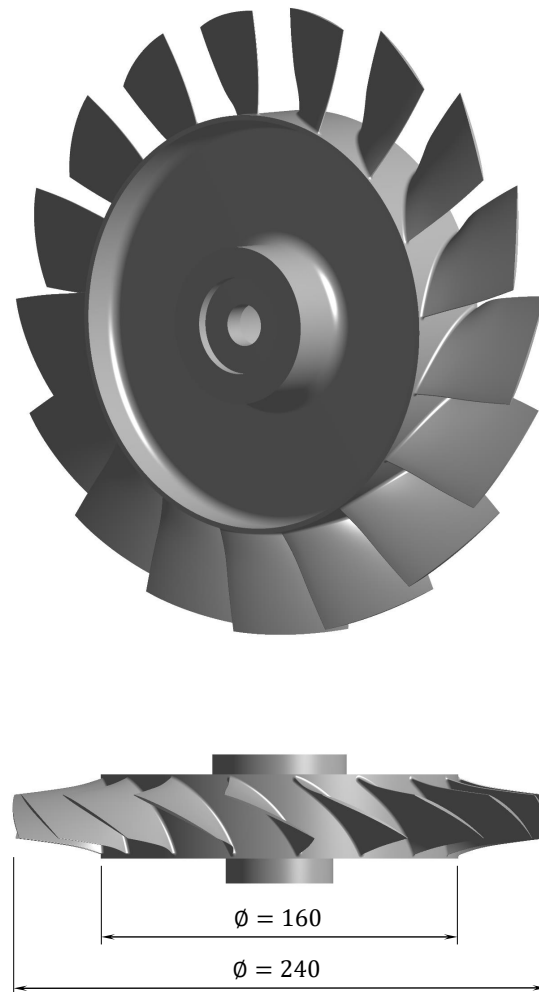


Fig. 4.1 – Baseline rotor geometry

Table 4.3 – Blade profile parameters

| Parameter | Symbol | Value |
|--------------------|---------------------|----------|
| Hub Radius | R_{Hub} | 80 [mm] |
| Shroud Radius | R_{Shroud} | 120 [mm] |
| Span Height | S | 40 [mm] |
| Aspect Ratio | S/C | 0.81 |
| Solidity (midspan) | C/P | 1.22 |

5 Computational Fluid Dynamics Model

The following chapter focuses on an overview of the simulation setups used in the present work. A description of the CFD mesh, boundary conditions, turbulence model and solver settings as well as an introduction to the various softwares used for preparation of the numerical models is represented.

5.1 CFD Mesh Generation

The CFD meshes used in steady-state as well as unsteady simulations performed in this study, have been prepared using, NUMECA's AutoGrid5 which is an automatic meshing system for turbomachinery configurations. AutoGrid takes advantage of the characteristics of turbomachinery configurations by creating blade to blade grids onto surfaces of revolution [19]. Mesh generation in AutoGrid involves the following steps:

- Geometry definition; the curves required for the definition of hub and shroud surfaces of revolution
- Generation of meridional flow path
- Generation and control of 2D meshes (topology, grid clustering etc) on spanwise surfaces
- Generation of the final 3D mesh

AutoGrid enables to generate adapted structured meshes. Although generation of structured mesh can be complex, in particular for blade geometries with high stager angle, this type of mesh is preferred due to higher accuracy results.

5.1.1 Mesh Domain Definition

For this study a single passage domain with periodic boundaries is defined, which can be transformed conveniently in CFX-Pre in order to create domains with different number of passages depending on the simulation requirements. The spanwise boundaries of the domain, namely the hub and the shroud along with the blade and the inlet and outlet limits are defined by a number of curves in Cartesian or cylindrical coordinates. A MATLAB script has been used in order to modify a predefined geomTurbo template script with the corresponding data of the curves, hub and shroud radius, hub fillet, shroud tip gap and the location of the inlet and outlet limits. An example of a CFD mesh domain generated for the baseline rotor is illustrated in Figure 5.1.

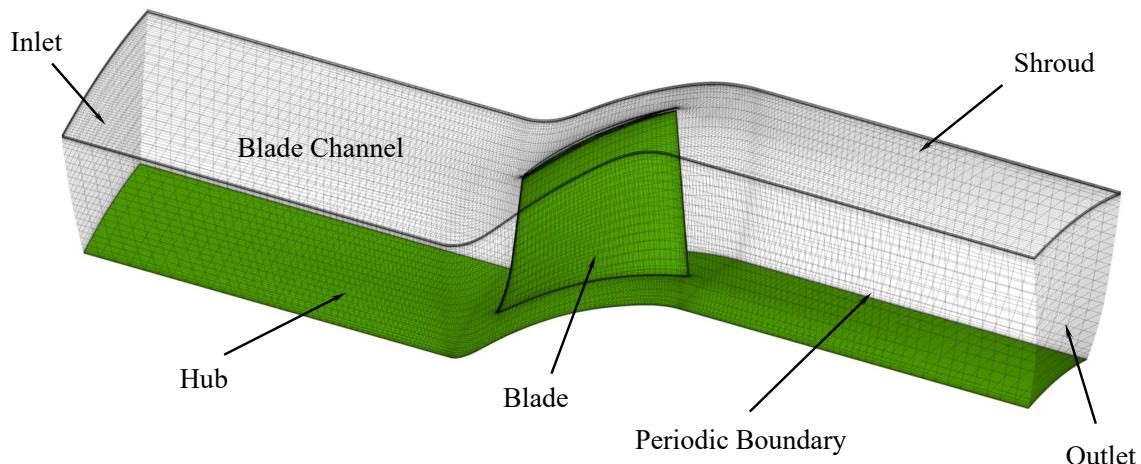


Fig. 5.1 – An example of a medium mesh domain generated for the baseline rotor

5.1.2 Meridional Control

The 3D row meshes generated with AutoGrid are obtained by stacking blade to blade meshes on surfaces of revolution generated from meridional curves called flow paths. The number of flow path in spanwise direction, cell width at the hub and shroud and hub fillets can be adjusted in order to obtain desired mesh resolution. It is also possible to introduce meridional control lines to directly control the block faces which are used to construct flow paths. For the purpose of the present work, meridional control lines have been implemented in order to coarsen the mesh towards the inlet and outlet boundaries (relax inlet and outlet clustering) to avoid any possible numerical problems arising from wall reflections.

5.1.3 Blade to Blade Control

The blade to blade meshes are created using a two dimensional multi-block structured topology. Each block has four edges along which grid points are distributed. Depending on the turbomachinery type, it is possible to use three different blocking topologies namely O4H, H&I or H&H. For instance when the row geometry contains splitter blades or if the machine includes a centrifugal impeller, the H&I topology is recommended by AutoGrid. In this study a O4H topology is chosen which consists of an O block around the blade (skin block) and four H blocks surrounding it as shown in Figure 5.2.

Blade to Blade mesh control make it possible to determine the number of grid points along the solid wall depending on the grid level. This tool also includes an option to obtain matching periodicity boundary condition in order to avoid possible errors due to interpolations at the mixing planes. The shroud gap in O4H configuration, includes a H block surrounded by an O-block. By default, the shroud gap mesh matches the skin mesh around the blade, therefore it is usually enough to adjust the number of points inside the O-block. The skin block is created using a hyperbolic mesh.

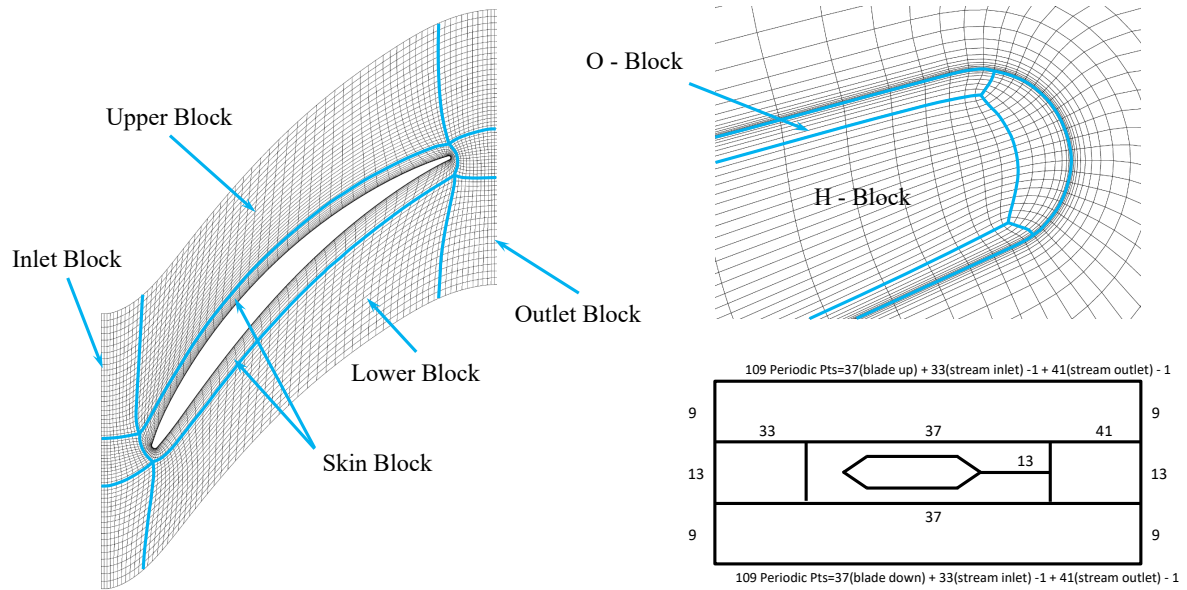


Fig. 5.2 – An overview of the O4H block topology formed at the midspan position (left) and shroud gap region (right)

The width of the boundary layer is controlled by the cell width at the wall, the expansion ratio and the number of points in it. The width of the first cell close to the wall has a direct influence on Y^+ values, which is a dimensionless wall distance parameter defined as [19]

$$Y^+ = \frac{Y_{\text{wall}} \cdot u_{\tau}}{\nu} \quad (5.1)$$

where

$$Y_{\text{wall}} = 6 \left(\frac{u_{\text{ref}}}{\nu} \right)^{-\frac{7}{8}} \left(\frac{L_{\text{ref}}}{2} \right)^{0.125} Y^+ \quad (5.2)$$

In equations 5.1 and 5.2, u_{τ} denotes the friction velocity, ν is the kinematic viscosity, u_{ref} , is a reference velocity of the flow and L_{ref} represents the reference length of the test case. The implementation of the wall boundary conditions in turbulent flows starts with the evaluation of Y^+ values.

The implementation of wall boundary conditions in turbulent flows start with the evaluation of Y^+ values. A near-wall flow can be assumed to be laminar if Y^+ has a value which is lower than 10. The wall shear stress is assumed to be entirely viscous in origin. Otherwise for turbulent flows a wall function approach can be used [26]. Thus the width of the first cell close to the wall must be selected with care since the quality of the flow solution will often depend upon the capture of the flow phenomena inside the boundary layers which develop along the solid walls.

5.2 CFD Simulation Setup

ANSYS CFX is a general purpose computational fluid dynamics solver which consists of three software modules namely, CFX-Pre (physical pre-processor), CFX-Solve (solver) and CFD-Post (post-processor). CFX uses a coupled solver, meaning that all the hydrodynamic equations are solved as a single system [1]. In the following subsections an overview of flow physics, boundary conditions and solver parameters implemented in this study, is represented.

5.2.1 Domain Settings

CFX-Pre, uses the 3D primitives of the imported mesh to create fluid domains, that can be conveniently transformed to build various flow passages according to the requirements of the analysis. In the present work a Total Energy heat transfer model has been used which models the transport of enthalpy and includes kinetic energy effects. The selection of the Total Energy model has implications for whether the fluid is modeled as compressible or incompressible (Air ideal gas in this case).

Turbulence Model

The most common turbulence models used in CFD codes can be classified as classic models which are based on time-averaged Reynolds equations or large eddy simulation models. Large eddy simulation models are turbulence models where the time-dependent flow equations are solved for mean flow and the largest eddies and where the effects of smaller eddies are modeled [26]. Meanwhile large eddy simulations are currently very costly and time consuming, the classical models are sufficient for most of the engineering applications. Among the classical models, the $k-\omega$ model, has the advantage of the near wall treatment for low-Reynolds number computations. This model does not involve the complex nonlinear damping functions required for the $k-\epsilon$ model and is therefore more accurate and more robust. The $k-\omega$ model assumes that turbulence viscosity is linked to the turbulence kinetic energy and turbulence frequency via the relation [1]

$$\mu_t = \rho \frac{k}{\omega} \quad (5.3)$$

The Shear Stress Transport (SST) Model, used in the current investigation, is a $k-\omega$ based model that accounts for the transport of the turbulent shear stress and gives highly accurate predictions of the onset and the amount of flow separation under adverse pressure gradients. Other $k-\omega$ models such as Wilcox and Baseline $k-\omega$ model (BSL), fail to properly predict the onset and amount of flow separation from smooth surfaces due to the fact that these models do not account for the transport of the turbulent shear stress, and thus overpredict the eddy-viscosity. The SST model on the other hand imposes a limiter to the formulation of the eddy-viscosity in order to obtain a better transport behavior [1]. It is worth noting that for SST model, an Automatic Near-Wall Treatment is implied by CFX, which replaces the wall functions with a low-Reynolds near wall formulation.

Mesh Deformation

In case of transient simulation, oscillatory motion of the blades within the fluid domain, can be simulated as moving wall boundaries, which introduce a mesh deformation with a predefined stiffness. Among various mesh deformation models available in CFX, the “Regions of Motion Specified”, model enables the specification of the motion of nodes on boundaries of the mesh using CEL (CFX Expression Language) expressions. The motion of all the other nodes is then determined through a displacement diffusion model by solving the following equation

$$\nabla \cdot (\Gamma_{\text{disp}} \nabla \delta) \quad (5.4)$$

Where Γ_{disp} denotes the mesh stiffness, and δ is the displacement relative to the previous mesh locations [1]. In equation 5.4, defining a constant value for mesh stiffness, may lead to large deformation of smaller cells near boundaries and thus formation of negative cells during the simulation. In order to preserve mesh distribution and quality near fine boundary layers or fine geometrical features, a variable mesh stiffness can be defined. In CFX, different mesh stiffness options such as “Increase Near Small Volumes” and “Increase Near Boundaries” are available to induce a non-homogeneous diffusion of the displacements throughout the mesh. Meanwhile the “Blend Distance and Small Volumes” option, combines features of both of the mentioned models and makes use of information about the local domain mesh. This model is formulated as

$$\Gamma_{\text{disp}} = A \left(\frac{V_{\text{ref}}}{V} \right)^{C_{\text{vol}}} + B \left(\frac{L_{\text{ref}}}{\max(d, d_{\text{wall}})} \right)^{C_{\text{dis}}} \quad (5.5)$$

where

- $L_{\text{ref}} = 0.5 (\text{volume of domain})^{1/3}$
- $d_{\text{wall}} = 10 (\text{minimum control volume in domain})^{1/3}$

In equation 5.5, V and d are the local values for control volume size and the distance from the nearest boundary respectively. V_{ref} is a mean control volume in the domain and factors A and B are simple default weights that indicate a dominance of one term over the other [1]. In this relationship, the exponents C_{vol} and C_{dis} , provide an exponential increase in the mesh stiffness as the control volume size and the distance from the nearest boundary decrease. It is worth noting that, different numerical schemes can be chosen for solving the mesh displacement diffusion equation in CFX. This is done by implementing an “expert parameter” in order to obtain an improved mesh quality and to avoid mesh folding.

Mapping of Mode Shapes

As it is mentioned above, the “Regions of Motion Specified” mesh deformation model, requires CEL expressions which contain information about the motion of nodes on boundaries of the mesh. In the present work such CEL files are created using a Matlab script

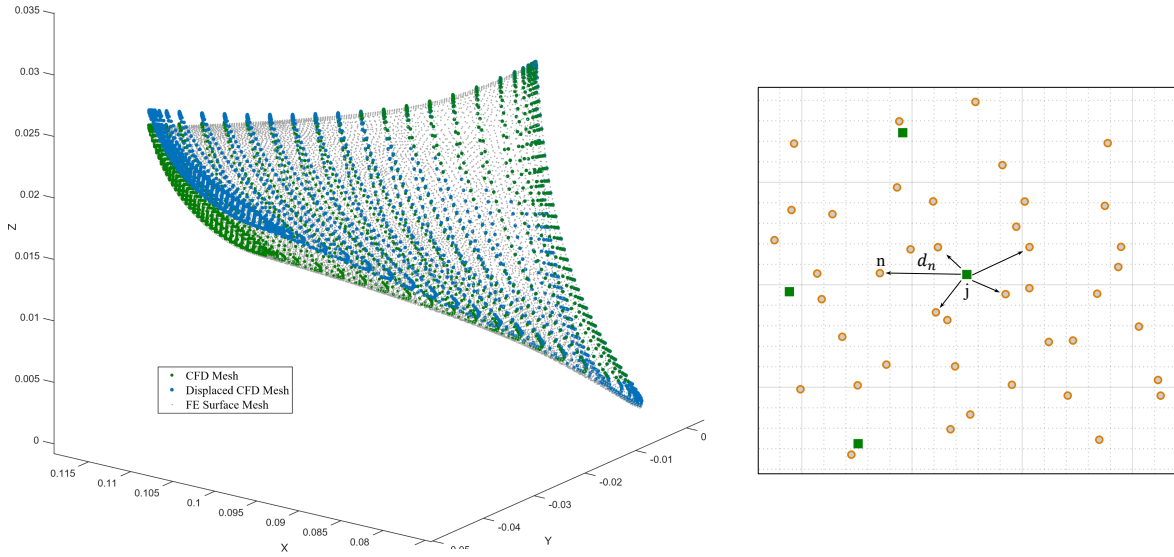


Fig. 5.3 – An overview of the surface CFD mesh with its displaced shape (left) and a graphical representation of the mapping process (right)

which is intended for mapping the mode shapes of the FE mesh, generated by ANSYS Mechanical APDL, to the corresponding nodes on the CFD mesh. In this regard for every CFD node j on the surface of the blade, the surface FE nodes are sorted in order of their distance from node j and then a weighted average of the displacement of the n nearby nodes is mapped on the node j as formulated below

$$d_{CFD,j} = \frac{\frac{1}{d_1^2} \cdot d_{FE,1} + \frac{1}{d_2^2} \cdot d_{FE,2} + \dots + \frac{1}{d_n^2} \cdot d_{FE,n}}{\sum_{i=1}^{i=n} \frac{1}{(d_i + \epsilon)^2}} = \frac{\sum_{i=1}^{i=n} \frac{1}{d_i^2} d_{FE,n}}{\sum_{i=1}^{i=n} \frac{1}{(d_i + \epsilon)^2}} \quad (5.6)$$

In equation 5.6, $d_{CFD,j}$ denotes the displacement of the resultant displacement of the CFD node j , $d_{FE,n}$ is the displacement of the n^{th} nearby FE node and ϵ is an offset value to avoid singularities in computation of distances between nodes. It is worth noting that in this study, the displacements are normalized over the chord length of the blade. Figure 5.3, illustrates the CFD mesh of the baseline rotor blade surface along with the displaced mesh under the first mode of blade vibration.

5.2.2 Boundary Conditions

Numerical solution of the NFS system of equations within a discretized fluid domain, require specification of the conditions on external boundaries of the domain. Thus with the solution being directly dependent on the boundary conditions, it is important to set appropriate boundary conditions which accurately reflect the real flow field. In CFX different boundary conditions such as inlets, outlets, openings, walls and symmetry planes, can be applies to any bounding surface of a 3D primitive that is included in the domain.

For a given computational domain various combinations of boundary conditions can affect the robustness and thus the reliability of the results. For instance a combination of total pressure at an inlet and velocity/mass-flow at an outlet is robust since the static pressure at the outlet and the velocity at the inlet are part of the solution. On the other hand though, a combination of total pressure at an inlet and static pressure at an outlet makes the solution very sensitive to initial guess as the system mass-flow is part of the solution.

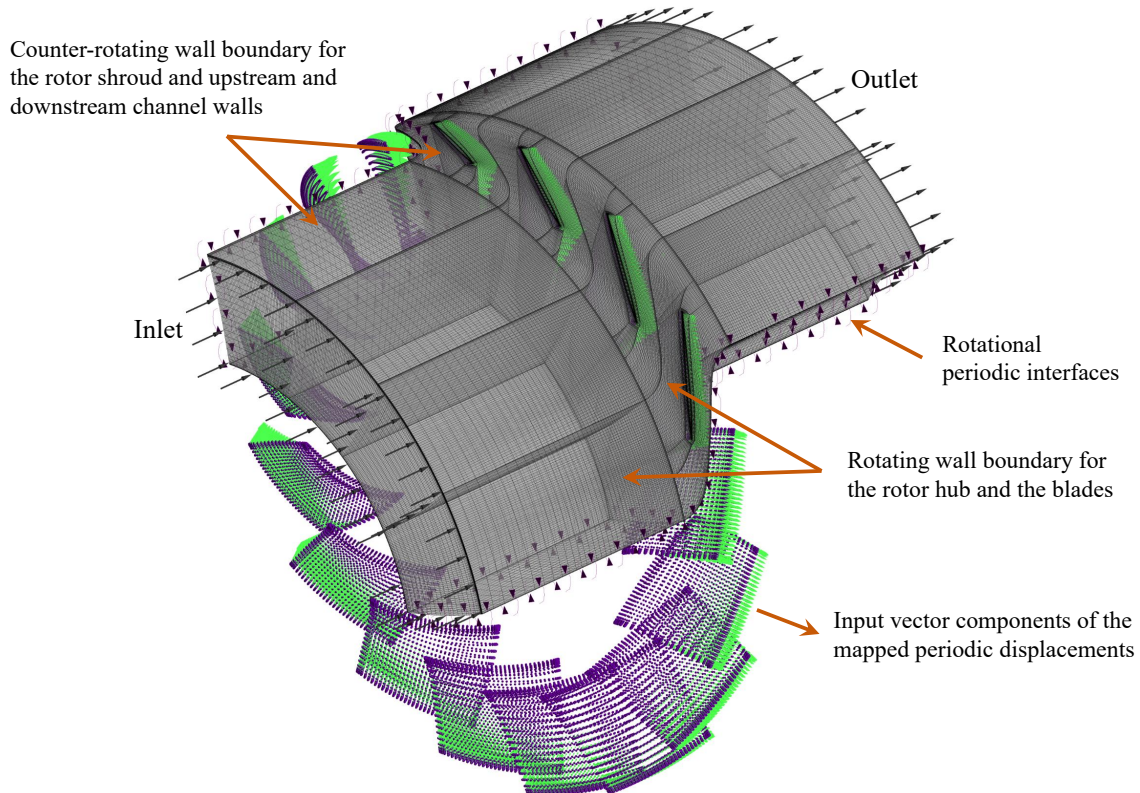


Fig. 5.4 – An overview of the boundary conditions imposed for a model with four passages

Inlet

An inlet boundary condition of a domain can be specified in different types considering the mass and momentum equations, the turbulence model and the energy equation. In the present work, the static frame total pressure, p_{tot} , is specified for both the steady state and transient simulations, where CFX-Solver computes the static pressure needed to properly close the boundary condition. It is also possible to define the direction vector explicitly in Cartesian coordinates or alternatively to define it as normal to the boundary. The scale of inlet turbulence quantities, such as inlet turbulence energy k and turbulence viscosity μ_t , are either directly specified or calculated according to the turbulence intensity as

$$k_{\text{inlet}} = \frac{3}{2} I^2 U^2 \quad \text{and} \quad \mu_t = C I \mu \quad (5.7)$$

Where I denotes the turbulence intensity and C is turbulence intensity factor at the boundary condition (default value of C is 1000). Regarding the boundary advection and diffusion terms of the energy equation, by setting the inlet total temperature, the static temperature is dynamically computed as

$$T_{\text{static,inlet}} = T_{\text{tot,inlet}} - \frac{U^2}{2C_p} \quad (5.8)$$

Outlet

The various boundary conditions which can be defined at the outlet of a domain, include static pressure, velocity or mass flow. For all other transport equations, the outlet value of the variable is part of the solution. The velocity constraints can be specified either as normal to the boundary or with its Cartesian coordinates. Meanwhile the mass flux distribution across the outlet is determined by comparing the estimated total mass flow rate, $\dot{m}_{\text{tot}}^{\text{est}}$, calculated by the flow solver with the specified value of mass-flow rate, \dot{m}_{spec} . Thus a scaling factor F can be calculated as the ratio of \dot{m}_{spec} over $\dot{m}_{\text{tot}}^{\text{est}}$, which will be multiplied to the integration point mass-flow in an iterative procedure as

$$\dot{m}_{\text{ip}} = F \rho_{\text{ip}} A_{\text{ip}} U_{\text{ip}} \quad (5.9)$$

As a result, the mass flux profile is an implicit result of the solution and at the same time gives exactly the specified mass flow rate [1]. In the present work, while mass-flow boundary conditions are used for the steady-state simulations, in case of transient simulations though, after comparing various boundary conditions at the outlet, a pressure boundary condition was chosen due to more robust numerical setups. In this case by specifying an average static pressure over the whole outlet \bar{p}_{spec} , the pressure profile can vary according to the upstream influences while constraining the average value to \bar{p}_{spec} as

$$\bar{p}_{\text{spec}} = \frac{1}{A} \int_S p_{\text{ip}} dA \quad (5.10)$$

Where p_{ip} , is the imposed pressure at each integration point. In order to impose this condition p_{ip} is calculated as

$$p_{\text{ip}} = \bar{p}_{\text{spec}} + (p_{\text{n}} - \bar{p}_{\text{n}}) \quad (5.11)$$

So, the integration point pressure in this case is set to the specified value plus the difference between the local nodal value and the average outlet boundary pressure [1].

Wall Boundaries

Different wall boundary condition settings which can be imposed in CFX include wall roughness and the flow velocity at the walls, regarding the mass and momentum equations, and heat transfer model, regarding the energy equation. If a rotational velocity is

imposed on the domain, all the wall boundaries within that domain including the blade and the hub will have a rotational motion as well, therefore a counter-rotating wall is introduced for the stationary shroud.

In case of unsteady simulations, the “Periodic Displacement” option allows to introduce a transient periodic motion to the blade surface nodes that repeats itself at a given frequency and has an associated phase offset. This is done by initializing a profile data which contains input vector components of the mapped mode shapes in a CEL file and sector tags which define position of each blade in cylindrical coordinate system. For Traveling Wave Mode simulations, by activating the “Transient Blade Row” feature of CFX, it is possible to associate a distinct phase shift to the oscillatory motion of each individual blade depending on its sector tag. It is also possible to specify a nodal diameter along with the direction of the traveling wave (forward/backward) for all the blades.

Domain Interfaces

Domain Interfaces provide a way of connecting meshes or domains together for different purposes. For instance they can be used for connecting unmatched meshes within a domain or connecting two separate domains such as domains rotating at different rates or domains with different physical types [1]. In an attempt to reduce the size of a computational domain by assuming periodicity in the model, it is possible to introduce “translational” or “rotational” periodic interfaces. In CFX there are various mesh connection options such as direct connections (One-to-One) or general grid interface connections (GGI), in order to ensure that the flow leaving one side of the interface appears on the other side.

5.2.3 Solver Control Settings

The basic parameters which control the CFX-Solver during the solution stage include advection scheme, transient scheme, turbulence numerics, convergence control and convergence criteria. In order to calculate the advection terms in the discrete finite volume equations, a distinct advection scheme such as “Upwind” or “High Resolution” can be associate to every set of NFS system of equations and the turbulence model. Method of time scale control for numerical simulations is one of the most important parameters influencing the convergence of a simulation. For steady state simulations, the “Physical Time Scale” option enables a fixed time scale to be used for the selected equations over the entire flow domain. In order to set a convergence criteria, a target value for residual size (RMS or MAX) can be imposed in solver control settings. It is worth noting that CFX uses normalized residuals to assess if convergence is reached or not.

In case of transient simulations, there are two transient methods available in CFX R18, namely the “Time Integration” and the “Harmonic Balance” methods. For the time integration method, the eigen-frequency of the corresponding mode shape is used to establish a value for the time period in which each disturbance of interest cycles an integer number of times [1]. When using the “Transient Blade Row” model, it is possible to directly compute the time step size by dividing the time period over a specified number of

time steps per period. With the accuracy of the solution being directly influenced by time step size, it is important to choose a proper number of time steps per period sufficient to resolve each disturbance.

5.3 Post-Processing Unsteady CFD Simulation Results

As the desired convergence criteria is reached, CFX-Solver will generate results files which contain a full description of the flow simulation including the calculated solution values at each mesh node in addition to the original information contained in the CFX-Solver input file. In case of unsteady simulations, it is also possible to export Transient Result files for specific time steps with selected variables.

The Transient Blade Row feature of CFX makes it possible to define aerodynamic damping monitor points with a value that is calculated according to the Equation. 2.12. It is worth noting that integration limits are set to encompass an integration interval rather than a vibration cycle and the resulting value yields the unnormalized value of aerodynamic damping which can be normalized if required. In case of Traveling Wave Mode simulations, with specified nodal diameter and traveling wave direction, it is enough to directly read the converged value of this monitor point.

Unlike TWM simulations where all the blades within the domain oscillate with a predefined inter-blade phase angle, in Influence Coefficients method simulations, the mesh motion is imposed on a single blade only with the neighboring blades remaining stationary during the unsteady flow simulations. Thus a post-processing procedure is required in order to superimpose linearly the influence of stationary blades on the moving blade with an appropriate phase shift as it is outlined in section 2.3.4. In this regard, either a time-domain approach or a frequency-domain approach can be implemented as it is described below.

5.3.1 Post-Processing Procedure in Time-Domain and Frequency-Domain

Once a transient periodic solution is achieved, it is necessary to export transient result files with selected variables such as mesh displacement, mesh velocity, pressures at nodes, blade surface normal vectors and elemental areas, for all the time-steps making up a full oscillation period.

In order to calculate aerodynamic damping through a time-domain approach, having extracted nodal pressure signals over a complete period, a force signal can be calculated for every node on the blade boundary surface. This is done by multiplying the resulting pressure signal of every node by the element surface area and corresponding normal vector. With the aim of linearly superimposing every component of the obtained nodal force vectors of the neighboring blades on the reference blade, a Fast Fourier Transformation (FFT), is then performed on the force signals so that an appropriate phase shift can be applied depending on the inter-blade phase angle as it is demonstrated in equation 5.12.

$$\hat{F}_{\text{overall}}(x, y, z) = \sum_{n=0}^{n=N_{\text{NB}}} \left| \hat{F}_n(x, y, z) \right| \cdot e^{-i(\phi_n \pm n\sigma)} \quad (5.12)$$

In equation 5.12, ϕ_n denotes the phase angle of the complex work whereas σ is the interblade phase angle which is either added or subtracted from the phase angle depending on the position of the each blade with respect to the reference blade.

Performing an inverse Fourier transformation on the resulting overall complex force, it is then possible to obtain the wall power density by multiplying the superimposed nodal force vectors by the corresponding mesh velocities, which can be subsequently integrated over one period to obtain the elemental wall work per cycle. In such a manner, the aerodynamic damping coefficient can be calculated by normalizing the negated value wall work density.

Following a frequency-domain approach on the other hand, an FFT is performed on both the nodal displacement and nodal force signals, which yield a complex displacement and a complex force that are phase shifted with respect to each other. Then in order to calculate a complex work value for every node the complex force shall be rotated with a rotation angle which equals to the difference in the phase angles of the two complex values as $\phi_{\text{rotation}} = \phi_F - \phi_d$.

$$\hat{W}_{\text{cycle}} = -\pi \sum_{n=0}^{n=N_{\text{NB}}} \left| \hat{d}_n \right| \cdot \hat{F} \cdot e^{\pm i\phi_{\text{rotation}}} \quad (5.13)$$

The complex work calculate through equation 5.13 for every node of each blade can be superimposed on the reference blade in a similar manner to the time-domain approach with the its corresponding phase shift for all the inter-blade phase angles. With the imaginary part of the overall complex work representing the unnormalized aerodynamic damping coefficient, the main advantage of the frequency-domain approach with respect to the time-domain approach is the fact that by performing an FFT on the overall complex work, it is possible to extract the influence coefficients of each of the individual blades on the overall aerodynamic damping coefficient as it is illustrated in Figure 5.5.

5.3.2 Calculation of Aerodynamic Damping Ratio

As it is explained in section 2.3.3, Verdon refers to aerodynamic damping as a normalized stability parameter which involves, work per oscillation cycle and a reference pressure according to equation 2.14. This definition of aerodynamic damping is practical in determining the onset of flutter as the flow field changes in a turbomachine for different operating conditions. However though with the aim of investigating the influence of geometrical parameters in aerodynamic damping for similar flow fields at a certain operating condition an alternative definition of stability parameter is required [21].

Carta has introduced an aerodynamic damping ratio ζ_{ae} , with reference to equation of motion of a single degree of freedom system in the presence of viscous damping [6].

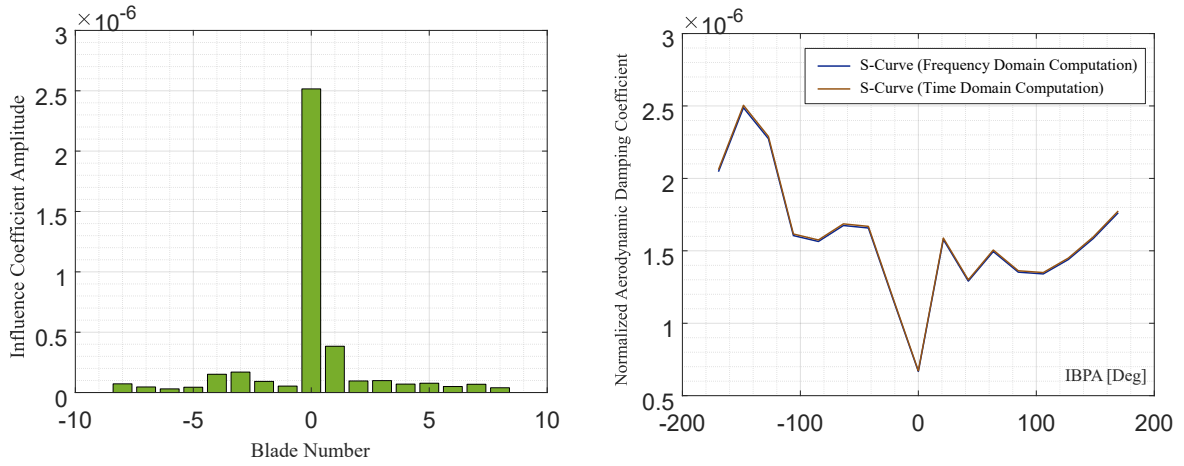


Fig. 5.5 – An example of extracted influence coefficients for a setup with 17 blades (left), and an example of a S-curve calculated both in time and frequency domain(right)

$$\ddot{x} + 2\omega_n \cdot \zeta \cdot \dot{x} + \omega_n^2 \cdot x = 0 \quad (5.14)$$

In equation 5.14, $\omega_n = \sqrt{\frac{k}{m}}$ denotes the undamped natural frequency whereas $\zeta = \frac{c}{c_{cr}}$ is the damping ratio with $c_{cr} = 2 \cdot m \cdot \omega_n$ being the critical damping. Thus the damping force F_d , can be written as

$$F_d = -c \cdot \dot{x} = -\zeta \cdot c_{cr} \cdot \dot{x} = -2\zeta \cdot m \cdot \omega_n \cdot \dot{x} \quad (5.15)$$

As a result the overall work performed by the damping force during every oscillation cycle can be computed as

$$W_d = -2\zeta \cdot m \cdot \omega_n \cdot \dot{x} \cdot \int_T \dot{x}^2 dt \quad (5.16)$$

An average kinetic energy per oscillation cycle is defined as

$$E_k = \frac{1}{T} \int_T \frac{1}{2} m \dot{x}^2 dt = \frac{m \cdot \omega_d}{4\pi} \int_T \dot{x}^2 dt \quad (5.17)$$

Where $T = \frac{2\pi}{\omega_d}$ denotes the period of damped oscillation cycle with $\omega_d = \omega_n \sqrt{1 - \zeta^2}$ representing the damped natural frequency. Assuming small values for ζ and with reference to the ratio of damping work per cycle over the average kinetic energy, an aerodynamic damping ratio can be defined as

$$\zeta_{ae} = -\frac{W_{d,cycle}}{8 \cdot \pi \cdot E_k} \quad (5.18)$$

With reference to the modal analysis concept and taking into account that the eigenvectors are mass normalized, a definition of maximum kinetic energy in matrix form can be derived as

$$E_{k,\max} = \frac{1}{2} [\dot{\Phi}]^T [M_m] [\dot{\Phi}] = \frac{1}{2} \omega_n^2 [\Phi]^T [M_m] [\Phi] = \frac{1}{2} \omega_n^2 \quad (5.19)$$

Consequently, assuming the average kinetic energy to be $E_K = \frac{1}{2} E_{k,\max}$ and subsituating it into the equation 5.18, the definition of aerodynamic damping ratio can be rewritten as

$$\zeta_{ae} = -\frac{W_{d,\text{cycle}}}{2 \cdot \pi \cdot \omega_n^2 \cdot S^2} = -\frac{W_{d,\text{cycle}}}{8 \cdot \pi^3 \cdot f^2 \cdot S^2} \quad (5.20)$$

It should be noted that in equation 5.20, the scaling factor S is implemented in order take into account the correlation between the vibration amplitude of the CFD mesh and the FE mesh as suggested by Moffatt and He [16].

6 Structural Dynamics Analysis

The following chapter focuses on an overview of the structural analysis performed in the present work. A description of the FEM simulation setup including mesh element type and boundary conditions, along with a mesh independence study and FE analysis results are presented. The modal analysis is performed by ANSYS Mechanical APDL, which is a general purpose finite-element modeling package intended for numerical solution of a wide variety of mechanical problems.

6.1 FEM Simulation Setup

In a general approach, an axial compressor blisk can be modeled as a bladed disk with oscillation modes which can be either blade-dominated or disk-dominated depending on its structural setup [27]. As a simplified model, in the absence of shrouds and lacing wires, the blades can be approximated as cantilever beams attached to a disk with a very high stiffness. While modeling the bladed disk assembly would be more realistic, on the other hand in order to determine the aerodynamic damping characteristics of the blisk, CFD simulations with full rotor passage will be necessary.

In this study, assuming a perfectly tuned rotor and with the aim of performing traveling wave mode simulations, the single blade geometry is considered for the sake of modal analysis. ANSYS Meshing is used to generate an automated FE mesh with an adaptive size control and a smooth transition inflation option, for the imported geometry from ANSYS DesignModeler. After importing the generated mesh in ANSYS Mechanical APDL the element type is modified to a “SOLID-187”, which is 3D 10-node tetrahedral structural solid element. The SOLID-187 element which is depicted graphically in Figure 6.1, is defined by 10 nodes, each having three translational degrees of freedom in x, y and z directions which is well suited to modeling irregular meshes.

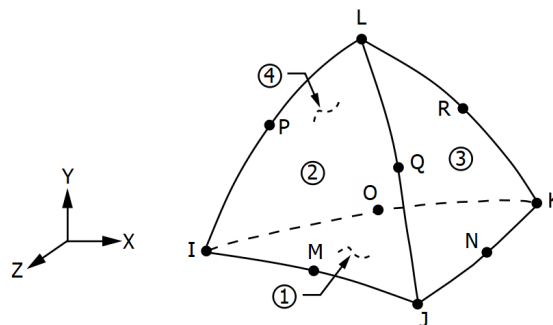


Fig. 6.1 – The Geometry, node locations and the coordinate system for SOLID-187 element, [2]

In addition to the nodal locations data, which is directly imported from ANSYS Meshing, the material properties including the Young's modulus and Poisson's Ratio, are the other input data that should be defined for this element type. In order to model the blade as cantilever beam, a boundary condition has been applied to the blade hub, in such a manner that all the translational degrees of freedom of the nodes corresponding to the blade hub surface have been constrained.

In order to determine the influence of centrifugal stiffening of the blade, prior to the modal analysis, a static analysis has been performed for the subject blisk which is constructed of 17-4 PH stainless-steel and has rotational speed of 16200 RPM. The eigenvalue problem is then solved using Block Lanczos modal-extraction method, which uses a sparse matrix solver, in order to extract the first 10 eigen-frequencies and the corresponding modal displacements.

6.2 Mesh Independence Study

FEM analysis have been performed for grids with different size starting from a very coarse mesh with approximately 600 elements to a very fine mesh with about 35000 elements, with the scope of investigating the influence of mesh size on numerical results. Figure 6.2, reports eigen-frequencies obtained for the three first modes with different meshes. It can be observed that a fine mesh with 28822 nodes and 16077 elements exhibits accurate results and thus has been chosen to proceed with the modal analysis of the baseline rotor blade.

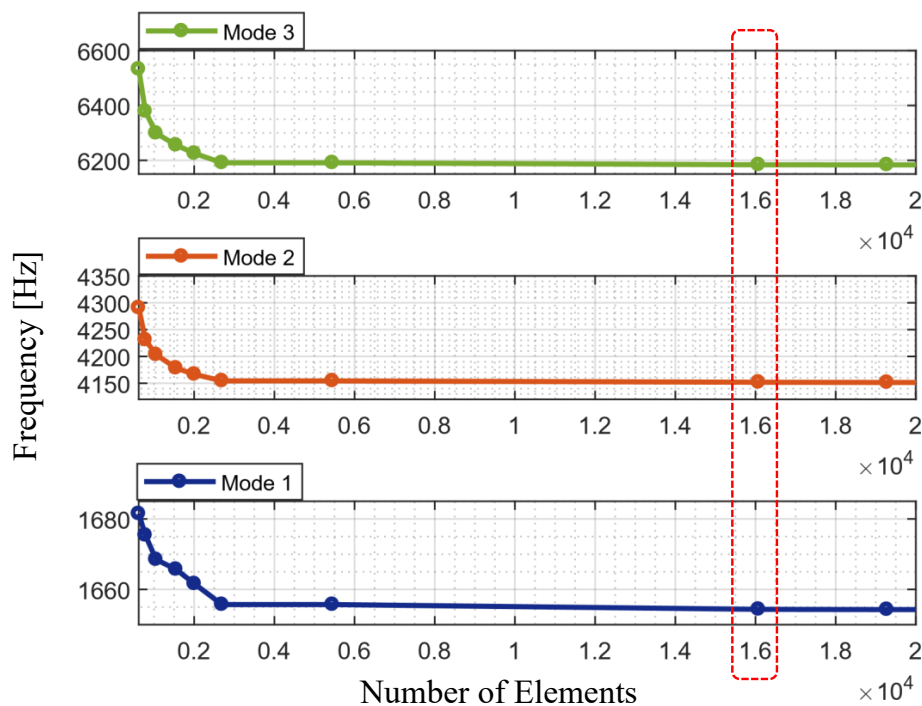


Fig. 6.2 – Influence of mesh size on the first three eigen-frequencies

6.3 Baseline Rotor Structural Analysis Results

An overview of the obtained mass-normalized, mode shapes and eigen-frequencies is illustrated in Figure 6.3. As it was described in the previous sections, the resulting nodal displacement of the blade surface nodes can be exported and mapped on the corresponding nodes of the CFD mesh in order to investigate the aeroelastic stability of the oscillating blades in a decoupled manner. It is worth noting that in the present work the first bending mode and the first torsional mode are chosen to proceed with investigation of the aerodynamic damping of the subject compressor blisk.

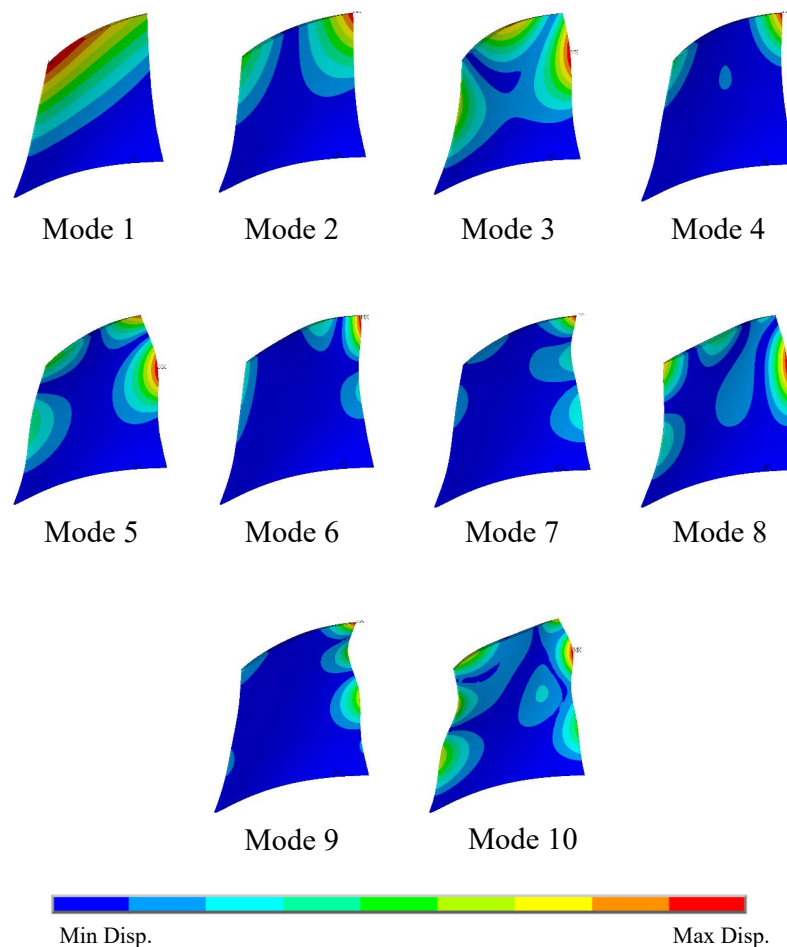


Fig. 6.3 – A graphical representation of 10 first modes shapes of the baseline rotor

Table 6.1 – 10 first eigen-frequencies of the baseline blisk rotating at 16200 RPM

| Mode Number | 1 | 2 | 3 | 4 | 5 | 6 | 7 | 8 | 9 | 10 |
|----------------|--------|--------|--------|--------|--------|-------|-------|-------|-------|-------|
| Frequency [Hz] | 1654.4 | 4151.9 | 6183.8 | 7323.4 | 9089.5 | 12273 | 12501 | 13134 | 16301 | 17969 |

7 CFD Numerical Influence Study

Prior to the solution of discretized CFD equations by CFX-Solver, it is necessary to perform a numerical influence study with the scope of determining the appropriate temporal and spacial increments such as grid spacing and element size. The following chapter represents an overview of the CFD simulation settings such as boundary conditions and solver controls applied in the present work for steady and unsteady simulations, as well as the numerical influence study which is performed for each case.

7.1 Steady State Simulations

For the subject axial compressor blisk, steady state simulations are performed using ANSYS CFX in order to obtain its performance characteristics for a specified rotational velocity over a range of different mass-flow rates. The results of such steady state simulations are also essential for imposing the initial conditions for the unsteady simulations. In table 7.1 a summary of the boundary conditions and solver controls implied for the steady state simulation setup is given. It is noted that the simulation domain consists of a single passages with periodic boundaries and inlet and outlet sections which are located at a distance of 100 [mm] from the rotor blade's leading and trailing edges.

Table 7.1 – Summary of the steady state simulation setup settings

| | |
|---|------------------------|
| Boundary Conditions | |
| Rotational Velocity | 16200 RPM |
| Inlet Total Temperature | 294 [K] |
| Inlet Total Pressure | 97000 [Pa] |
| Outlet Mass-Flow Rate (at design operating condition) | 2.2 [kg/s] |
| Solver Control | |
| Advection Scheme | High Resolution |
| Turbulence Model | Shear Stress Transport |
| Heat Transfer Model | Total Energy |
| Physical Timescale | 5×10^{-5} [s] |

Within this domain which includes a single isolated blade, rotating wall boundaries have been defined for the blade and rotor hub surfaces, whereas counter rotating walls are used for the stationary shroud as well as upstream and downstream channel hubs. Along with monitor points for pressure and temperature which provide a feedback on the convergence of momentum and energy equations, other monitor points for variables such as the total to total efficiency, compression ratio and shaft power have been defined.

Various CFD meshes with O4H block topology and different grid resolution and wall distance have been generated in AutoGrid with the aim of investigating mesh independence of the CFD simulations. Figure 7.1 illustrates an overview of the grid quality for three different meshes generated for the isolated blade of the baseline rotor. An option is available in AutoGrid which avoids mesh discontinuity at the blade tip-gap region that results in lower skewness angles at some regions. Thus it is necessary to maintain a minimum value of this parameter in order to guarantee accurate results. Table 7.2, summarizes the main parameters of the various meshes generated with different fineness level.

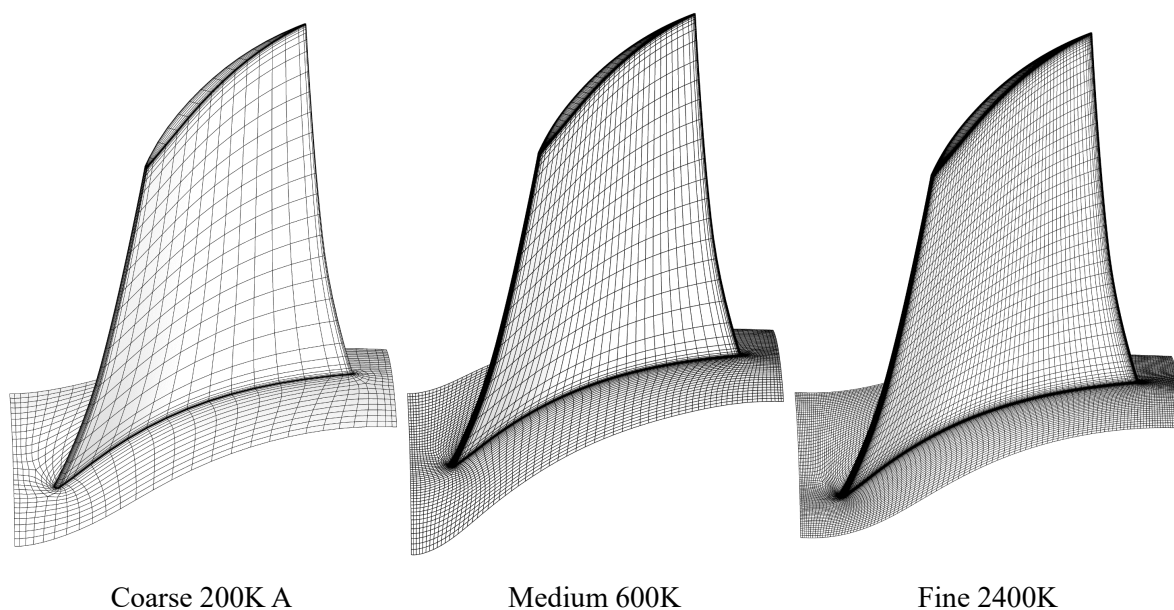


Fig. 7.1 – Mesh grid refinement from a very coarse mesh (left) to a very fine mesh (right)

Table 7.2 – Steady State simulation CFD mesh parameters

| Mesh Name | Number of Elements | Average Y^+ | Minimum Face Angle [deg] |
|------------------|--------------------|---------------|--------------------------|
| SS Coarse 200K A | 191312 | 0.6 | 21.3 |
| SS Coarse 200K B | 191312 | 1.2 | 21.3 |
| SS Coarse 400K A | 370132 | 0.6 | 18.3 |
| SS Coarse 400K B | 370132 | 4.0 | 17.3 |
| SS Coarse 400K C | 370132 | 16 | 18.1 |
| SS Medium 600K | 616252 | 0.6 | 19.9 |
| SS Medium 800K | 747456 | 0.6 | 19.9 |
| SS Fine 1000K | 941380 | 0.6 | 18.9 |
| SS Fine 1200K | 1138688 | 0.6 | 18.2 |
| SS Fine 2400K | 2338784 | 0.6 | 21.6 |

As a convergence criteria a monitor point has been defined so that in case the standard deviation of total to total efficiency reaches a value of 0.001 after a minimum number of 500 iterations, the solver stops the simulation.

Considering the above mentioned settings, steady state simulations were performed for various meshes at the design operating conditions. The diagrams illustrated in Figure 7.2, represent a comparison of the compression ratio Π and the isentropic total to total efficiency η_{tt} obtained at the end of simulations. It can be observed that the medium “SS Medium 600K” mesh which is highlighted in the figure has a deviation of 0.53 and 0.12 percents in terms of efficiency and compression ratio respectively in comparison to the finest mesh of “SS Fine 2400K”.

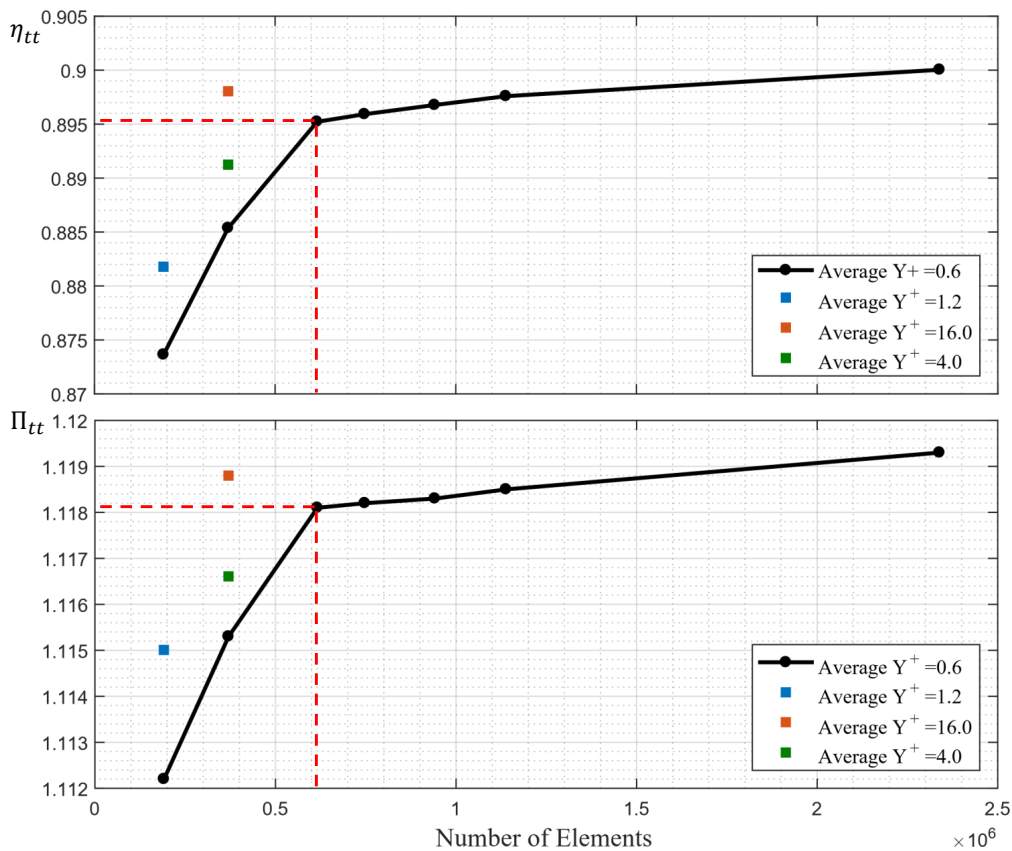


Fig. 7.2 – Comparison of efficiency η_{tt} and compression ratio Π_{tt} for various meshes size

In order to ensure an accurate prediction of the operating characteristics of the compressor rotor, further steady state simulations have been performed keeping the rotational speed unchanged, over a varying range of operating conditions with different mass-flow rates, for three selected meshes. As it is illustrated in Figure 7.3 the speed lines obtained for the three meshes are compared. Meanwhile comparing the Mach number plots at different span positions, as represented in Figure 7.4, a detailed investigation of the flow field changes with changing grid quality is possible. Comparing the steady state simulation results, it can be observed that the medium mesh “SS Medium 600k” reveals a reasonable trade off regarding the solution accuracy and computational effort.

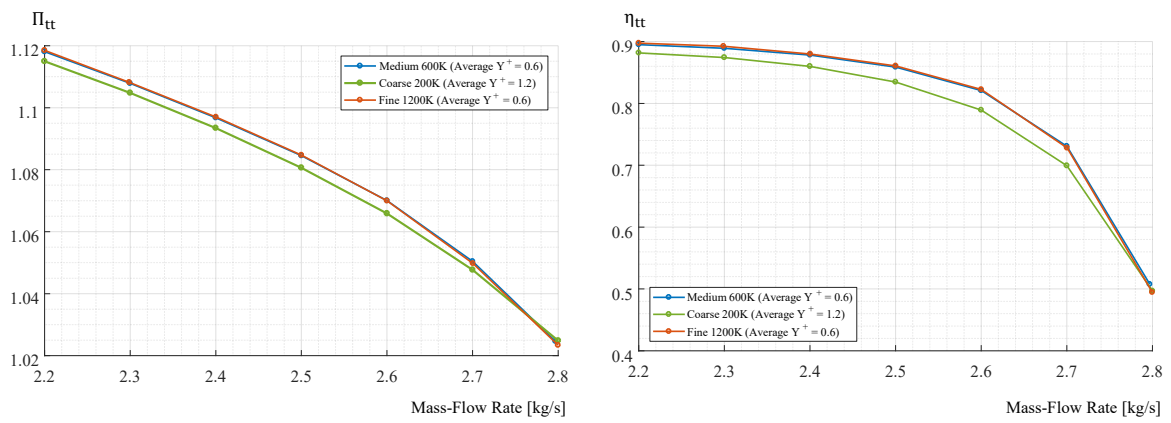


Fig. 7.3 – Comparison of efficiency η_{tt} and compression ratio Π_{tt} for various operating points

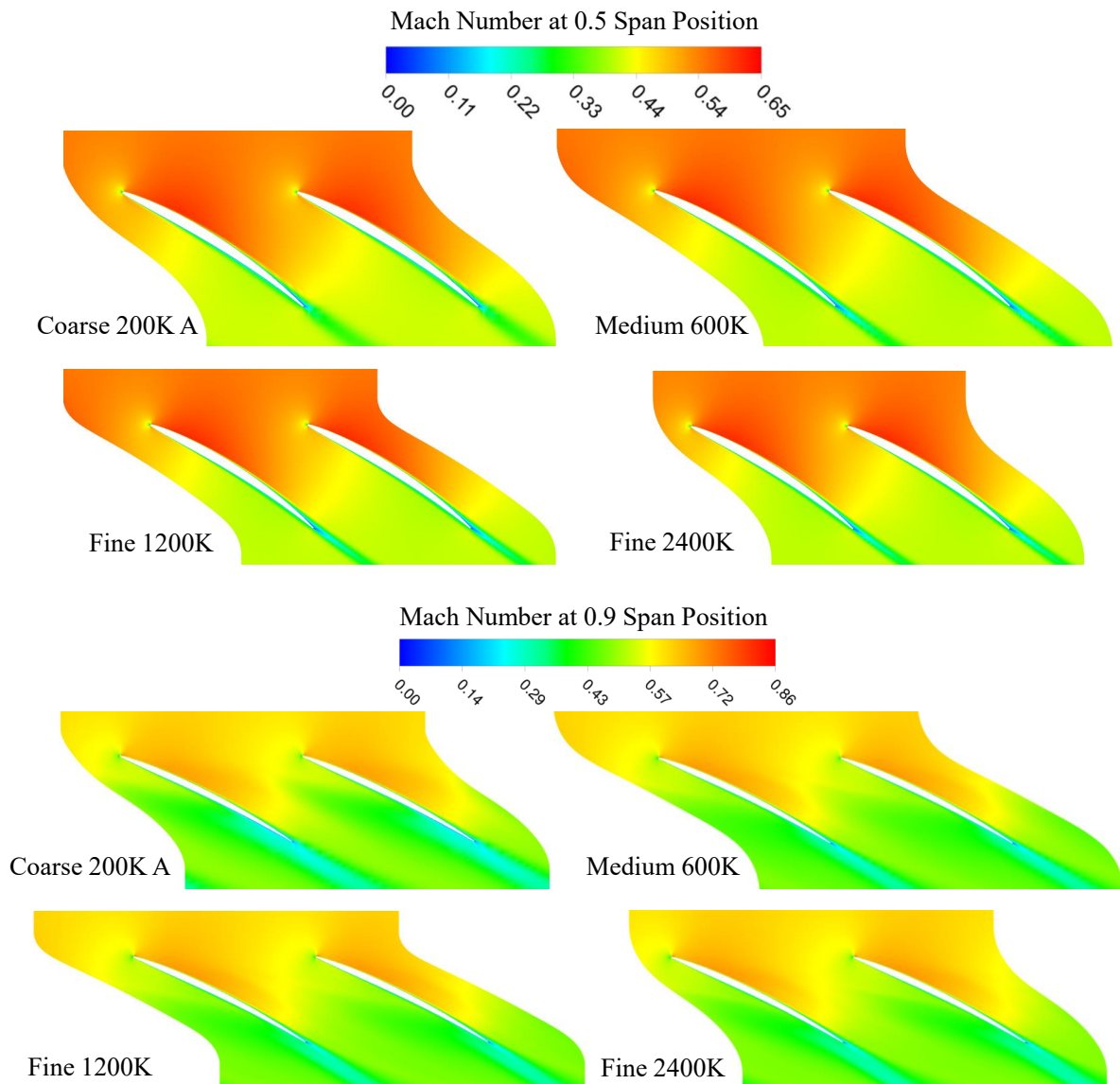


Fig. 7.4 – Mach number plots for different meshes at 0.9 and 0.5 span positions

7.2 Unsteady Simulations

In order to investigate the numerical influence on the unsteady simulations at the presence of oscillating blades, causing periodic mesh motion at the blade wall boundaries, traveling wave mode simulations have been performed for a single passage of the rotor with periodic boundaries, for an inter-blade phase angle of zero ($\sigma = 0$). In contrast to the steady state simulations, a pressure boundary condition has been implied at the outlet of the domain with the aim of obtaining more stable solutions. Also in order to avoid numerical issues due to the reflections from the wall boundaries, the distance of the inlet and outlet sections of the domain from the blade profile have been increased to 200 and 300 [mm] respectively with a coarser mesh resolution towards the inlet and outlet sections. In table 7.3 an outline of the boundary conditions and solver settings applied for the unsteady simulations, are presented, whereas Figure 7.5 illustrates the differences between the steady state and unsteady simulation meshes.

Table 7.3 – Summary of the unsteady simulation setup settings

| Boundary Conditions | |
|---|-------------|
| Rotational Velocity | 16200 RPM |
| Inlet Total Temperature | 294 [K] |
| Inlet Total Pressure | 97000 [Pa] |
| Outlet Average Static Pressure ^a | 102484 [Pa] |

a: implicit pressure averaging over whole outlet with a profile blend factor of zero

| Solver Control | |
|---------------------|-----------------------------|
| Advection Scheme | High Resolution |
| Transient Scheme | Second Order Backward Euler |
| Turbulence Model | Shear Stress Transport |
| Heat Transfer Model | Total Energy |
| Mesh Motion Model | Displacement Diffusion |

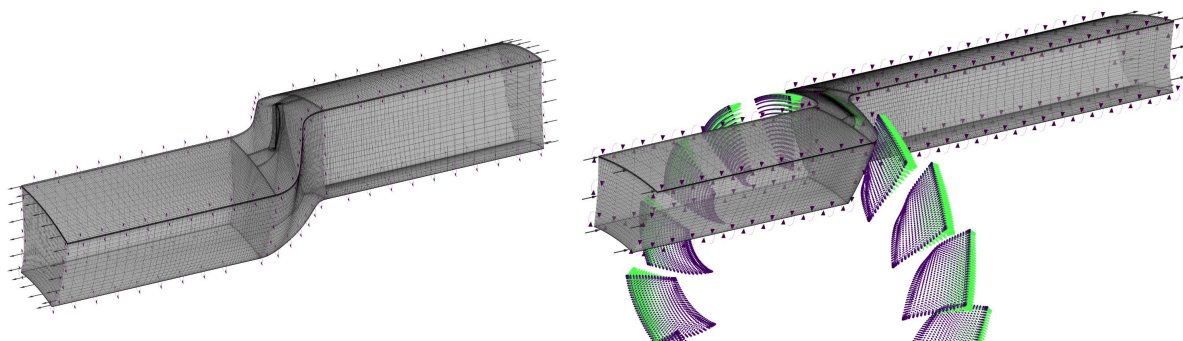


Fig. 7.5 – Steady State simulation mesh (left), compared to unsteady simulation mesh (right) with modified upstream and downstream channel length and mesh resolution

At the blade wall boundaries the displacement vectors corresponding to the first bending mode of the FE mesh are mapped onto the corresponding nodes of the CFD mesh with

an appropriate scaling factor and are introduced as a profile data into the simulation domain. It is worth noting that in order to avoid formation of negative cells due to the mesh deformations, the mesh stiffness option of “Blend Distance and Small Volumes” is incorporated into the mesh motion model which is of “Displacement Diffusion” type.

While monitor points are defined for different variables including the total-to-total efficiency, compression ration, mass-flow rate, and shaft power, the unnormalized value of the aerodynamic damping calculated by CFX-Solver has been monitored as a convergence criteria.

7.2.1 Mesh Resolution

With the aim of investigating influence of mesh resolution on the solution accuracy and the required computational effort, four different meshes were generated base on the meshes which were used for the steady state simulations. In this regard the distance of the inlet and outlet sections from the blade profile are increase and the the grid size gets coarser towards the inlet and outlet sections. Table 7.4 represents an overview of the generated meshes. With maximum amplitude of blade motion being scaled to 1% of the blade chord length, and setting the number of time-steps per period of run to 80, traveling wave mode simulations have been performed over 40 periods for each case. Monitoring the value of the calculated aerodynamic damping, as it is shown in Figure 7.6, it can be observed that full convergence is achieved after approximately 40 periods of run.

Table 7.4 – Unsteady simulation CFD mesh parameters

| Mesh Name | Number of Elements | Average Y^+ | Minimum Face Angle [deg] |
|----------------|--------------------|---------------|--------------------------|
| TR Coarse 200K | 213932 | 3.0 | 21.2 |
| TR Medium 600K | 669676 | 0.6 | 19.9 |
| TR Fine 1200K | 1310048 | 0.6 | 18.2 |
| TR Fine 2400K | 2557664 | 0.6 | 21.6 |

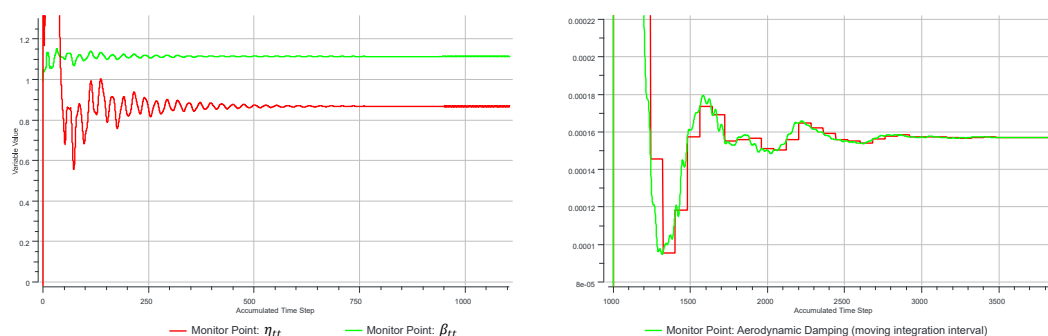


Fig. 7.6 – Monitor points for efficiency, compression ratio (left) and aerodynamic damping (right)

The diagram in Figure 7.7, summarizes the obtained values of aerodynamic damping which are normalized according to equation 5.20 for the four different meshes along with the computational time for each case to reach convergence in terms of CPU-Hours.

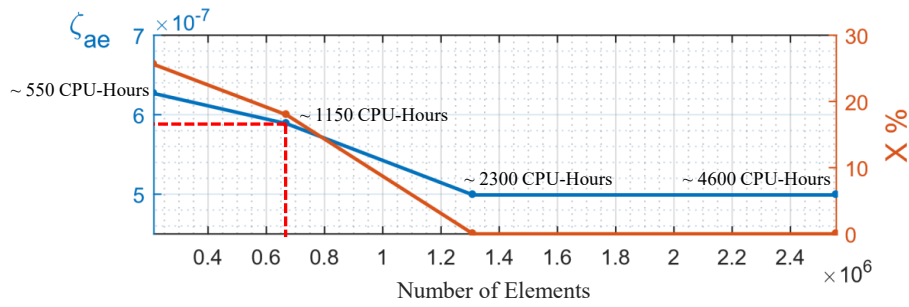


Fig. 7.7 – Normalized aerodynamic damping ratio as a function of mesh resolution

7.2.2 Number of Time-Steps per Period

Number of time-steps per period of run is another parameter which can affect the accuracy of solution as well as the computation time. With the frequency of blade oscillation determining duration of each period, three traveling wave mode simulations are performed in a range of 40 to 160 time steps per period. Figure 7.8, illustrates the results obtained through these simulations. Comparing the two diagrams of figures 7.7 and 7.8, it can be elucidated that, the medium mesh of “TR Medium 600K” results in an overestimation of the aerodynamic damping ratio by approximately 18 percent with respect to the finest mesh, whereas increasing the number of time-steps per period for the same mesh decreases this offset to approximately 6 percents. However this improvement of accuracy is achieved at a computation time which is approximately two times higher.

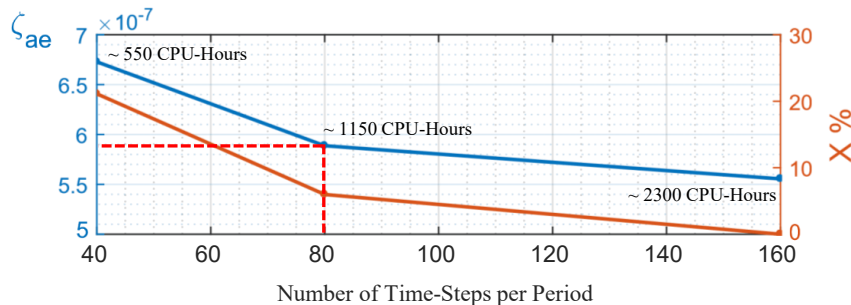


Fig. 7.8 – Aerodynamic damping ratio as a function of number of time-steps per period

7.2.3 Varying Amplitude of Mesh Displacement

In another attempt in order to verify the independence of the aerodynamic damping ratio, which is normalized according to the equation 5.20 over the oscillation frequency and scaling factor, from the amplitude of blade vibrations, further simulations have been performed for the medium mesh of “TR Medium 600K” by varying the max amplitude of motion in a range of 0.5 to 3 percent of the blade chord length and maintaining the number of time-steps per period at 80. As it is observed in Figure 7.9, the variations in aerodynamic damping ratio are negligible. This on the other hand indicates the reliability and robustness of the simulation setup.

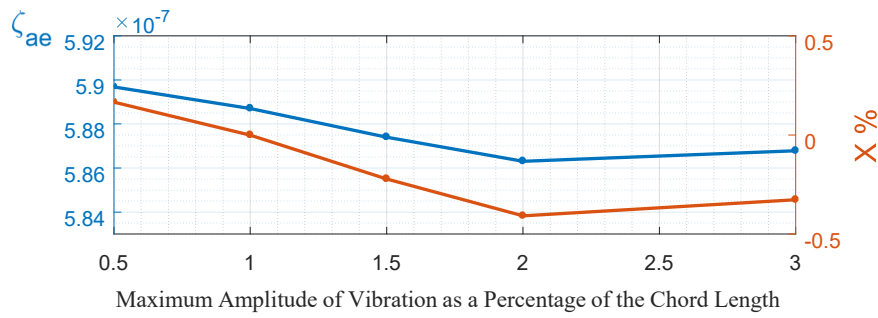


Fig. 7.9 – Aerodynamic damping ratio as a function of maximum amplitude of mesh motion

7.3 Traveling Wave Mode Simulations

Regarding the traveling wave mode approach, for the baseline rotor which consists of 17 equally spaced blades, the maximum number of nodal diameters equals to 8 as calculated according to equation 2.10. Thus considering both the forward and backward traveling waves, the inter-blade phase angle σ can take 17 discrete values including the $\sigma = 0$, in which all the blades oscillate with the same phase.

In order to determine variations of the aerodynamic damping ratio as a function of inter-blade phase angle, or to obtain the characteristic S-Curve in other words, traveling wave mode simulations have been performed for all possible IBPAs. In this regard, for the first bending mode of the baseline rotor blade, 16 unsteady simulations have been performed using the “TR Medium 600K” mesh within a computational domain which consists of all the 17 passages of the rotor without a need for the periodic boundaries.

It is worth noting that the “Transient Blade Row” feature of ANSYS CFX makes it possible to apply a phase shift to each oscillating blade within the domain according to its corresponding sector tag, for various nodal diameters and different directions of the traveling wave. Performing the TWM simulations for over 40 periods of run each consisting of 80 time-steps per period, the aerodynamic damping ratio ζ_{ae} , is derived for all the IBPAs as it is reported in the characteristics S-Curve of Figure 7.10.

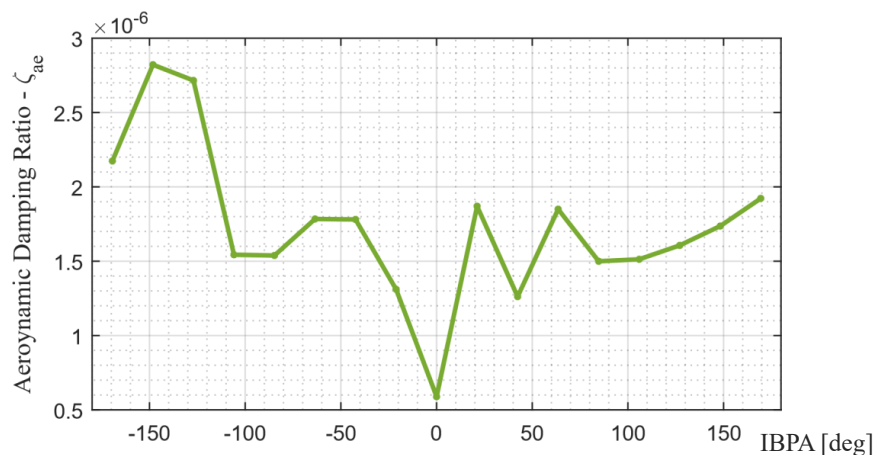


Fig. 7.10 – S-Curve for the baseline case with blades vibration at the 1st bending mode

7.4 Influence Coefficients Method Simulations

Referring to the definition of influence coefficients method as described in section 2.3.4, it can be elucidated that unlike the traveling wave mode approach, the computational domain corresponding to the ICM method involves a reference blade which has an oscillatory motion with the other neighboring blades remaining stationary. In contrast to the TWM approach a single simulation is sufficient with the ICM approach for prediction of the characteristics S-Curve. In this regard a post-processing procedure is required as explained in section 5.3.1 in order to determine the aerodynamic damping ratio as a function of inter-blade phase angle σ .

According to the theoretical definition of ICM approach, it is assumed that the influence of neighboring blades on the reference blade depends on their relative distance, however though the accuracy of numerical results obtained through ICM approach depends directly on the number of passages included in the computational domain. In order to investigate the influence of number of simulated passages on the overall results two unsteady simulations have been performed for different computational domains one including 9 passages with periodic boundaries on either side, and another setup with 17 passages without periodic boundaries.

It should be noted that, similar to the TWM simulation, also in this case the “TR Medium 600K” mesh has been used and the blade is vibrating at its first bending mode with the number of time-steps per period which equal to 80. Figure 7.11 illustrates a comparative representation of the S-Curves obtained through the TWM approach and ICM approach with different computational domains.

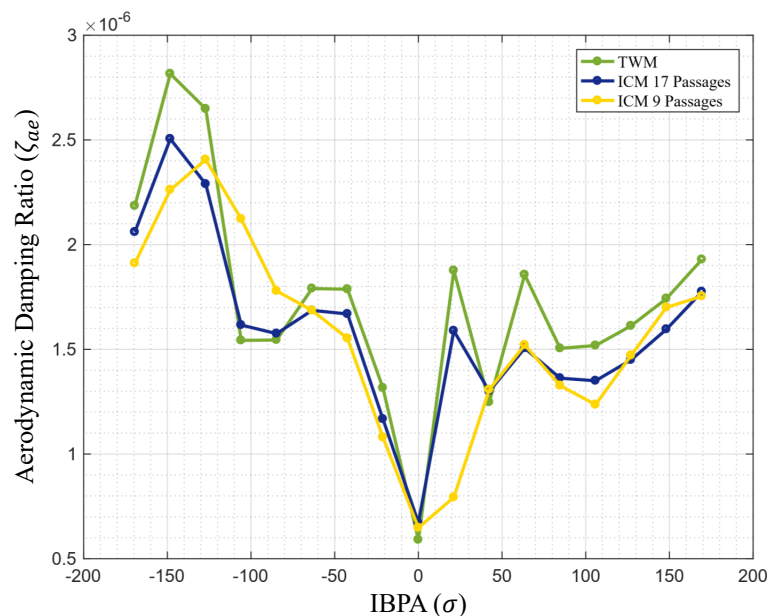


Fig. 7.11 – Comparison of S-Curves obtained with TWM and ICM approaches

It is observed that although the ICM method setup with 9 passages is able to predict the value of minimum damping ratio which corresponds to $\sigma = 0$, with a reasonable accuracy

with respect to the TWM approach, in some particular nodal diameters the deviations are not in an acceptable range. On the other hand in case of the ICM setup with 17 passages, the resulting S-Curve reveals a better accordance with regards to the S-Curve obtained though the TWM Approach.

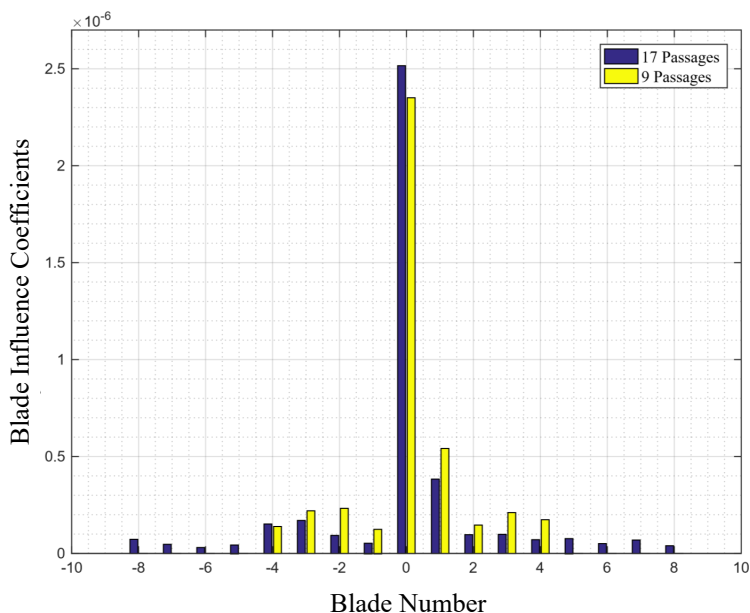


Fig. 7.12 – Comparison of blade influence coefficients obtained through ICM simulations for two computational domains with different number of simulated passages

Figure 7.12 illustrates the differences in blade influence coefficients obtained for the two different ICM simulation setups. As it is described in section 5.3.1, blade influence coefficients represent the contribution coming from each of the individual blades present in the simulation domain, to the overall complex work value that is calculated through the frequency-domain post-processing of the unsteady CFD simulation results. It is observed that in case of the simulation setup with 9 passages, the influence of the reference blade is lower compared to the case with 17 passages, while the influence of the other neighboring blades are over estimated.

Table 7.5 reports an overview of the computational time required to derive the characteristics S-Curve through the TWM and ICM approaches. It is noted that using the ICM method for a CFD setup consisting of 17 passages, results in a reduction of the computational effort by a factor of 16 compared to the TWM approach.

Table 7.5 – Computational time required for CFD simulation using TWM and ICM methods

| Case Name | Number of Required Simulations | Total Computation Time in CPU-Hours |
|-----------|--------------------------------|-------------------------------------|
| TWM | 17 | 369800 |
| ICM 9 | 1 | 11900 |
| ICM 17 | 1 | 23000 |

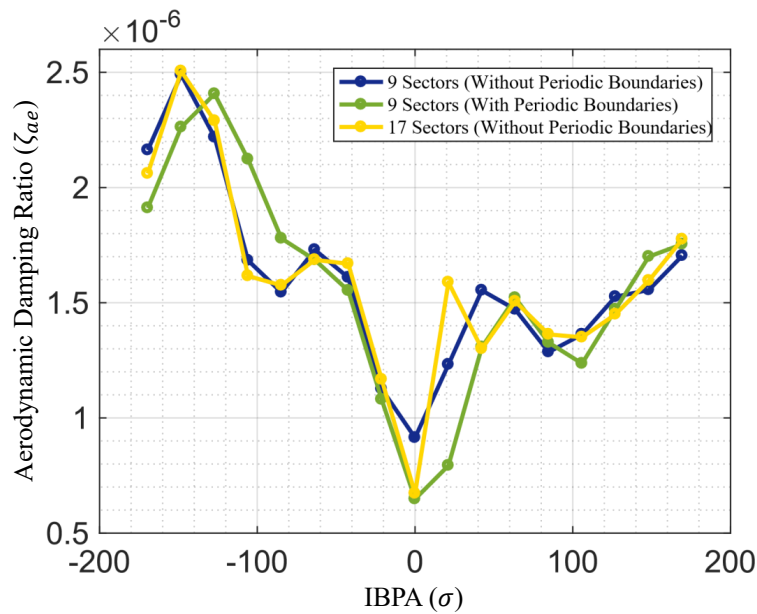


Fig. 7.13 – S-Curves obtained using ICM method with different number of passages

In a further attempt to investigate the influence of the number of simulated passages on the accuracy of the S-Curve derived through the ICM method, it is possible to perform the post-processing procedure using the pressure signals of only 9 blades in a setup consisting of 17 passages. The derived S-Curve is then compared with the setup including 9 passages and periodic boundaries as it is shown in Figure 7.13.

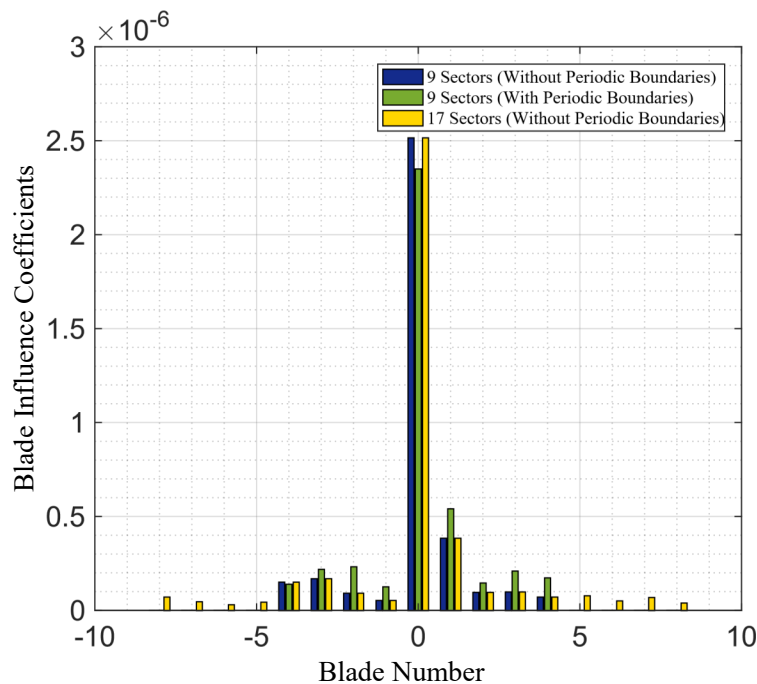


Fig. 7.14 – Blade influence coefficients obtained using ICM method with different number of passages

In a similar manner the blade influence coefficients are compared as it is reported in Figure 7.14. It can be elucidated that the calculated aerodynamic damping ratio for every inter-blade phase angle is influenced by the magnitude and the number of blade influence coefficients considered within the post-processing procedure.

Comparing the S-Curves obtained through numerical simulations with traveling wave mode approach and influence coefficients method, and taking into account the amount of required computational effort, it can be elucidated that the influence coefficients approach yields an appropriate tool for investigation of the influence of geometrical parameters on the aerodynamic damping ratios. Therefore within the present work the influence coefficients method with computational domains consisting of the complete rotor passage without periodic boundaries will be utilized.

8 Influence of Frequency Variations on the Aerodynamic Damping of the Baseline Rotor

With the aim of investigating the influence of frequency variations on the aerodynamic damping characteristics, the baseline rotor has been subjected to unsteady CFD analyses using influence coefficients method. In this regard for each of the two mode shapes under investigation, the blade oscillation frequency is altered while preserving the mode shape. With convergence being reached after approximately 40 periods of run, a post-processing procedure has been conducted on each result file as described in section 5.3.1, to obtain the characteristics S-Curves and to extract the blade influence coefficients.

8.1 1st Bending Mode

In addition to the frequency corresponding to the 1st bending mode shape of the blade which is computed through the modal analysis as described in chapter 6, unsteady CFD simulations are performed for blades oscillating at 1000 [Hz] and 3000 [Hz].

Figure 8.1, illustrates the obtained characteristic S-Curve for the three different cases. It is observed that the value of minimum aerodynamic damping ratio for the case in which the blade is oscillating at 1000 [Hz] corresponds to an interblade phase angle of $\sigma = 0$ and has a deviation of -8.9% compared to the baseline case (Frequency = 1654.4 [Hz]). Considering the case in which the oscillation frequency is set to 3000 [Hz] though, the minimum value of aerodynamic damping ratio corresponds to a nodal diameter of 1 of backward traveling wave and has a deviation of 36.8% with respect to the baseline case.

Considering Figure 8.2, it is noted that the value of influence coefficient of the central reference blade has a deviation of 41.5% and -42.3% for the cases of 1000 [Hz] and 3000 [Hz] respectively compared to the baseline case. Thus it can be elucidated that considering the three cases which have been investigated, the value of minimum damping ratio follows an increasing trend as the blade vibration frequency increases, whereas the influence coefficient of the central reference blade decreases as the frequency increases.

In Figure 8.3, the values of blade influence coefficients are reported as a function of blade vibration frequency. It should be noted that these values have been normalized over the corresponding maximum value of each case for every blade. Considering this plot, in the current case where the blades are oscillating with their 1st bending mode, a clear trend is not detected for all of the blades.

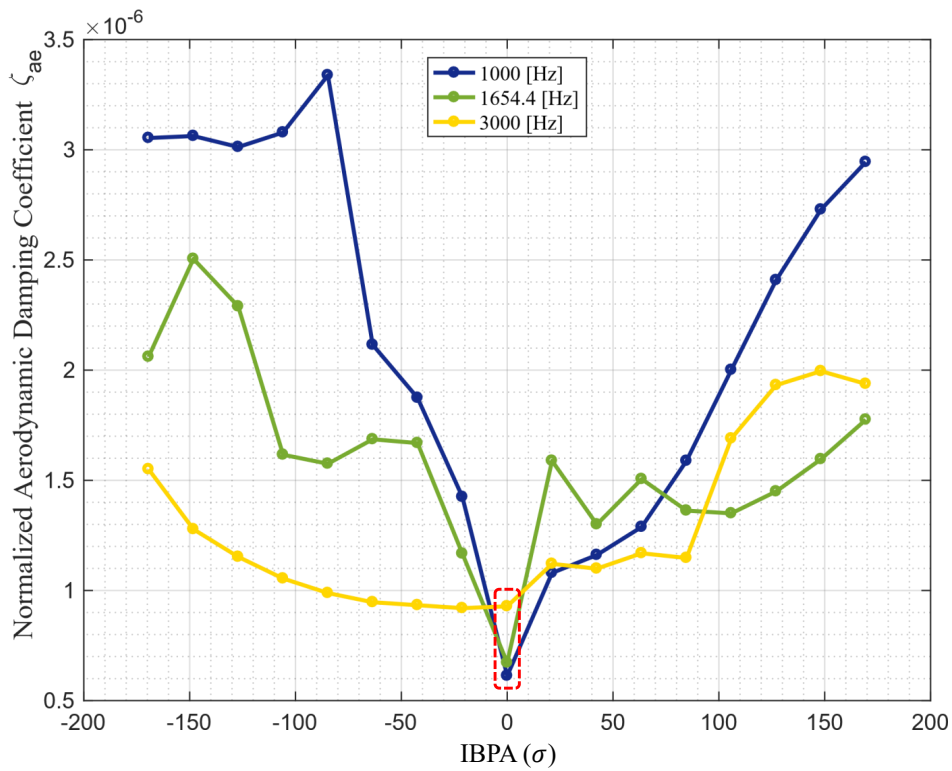


Fig. 8.1 – Characteristic S-Curve of the baseline rotor with different blade oscillation frequencies

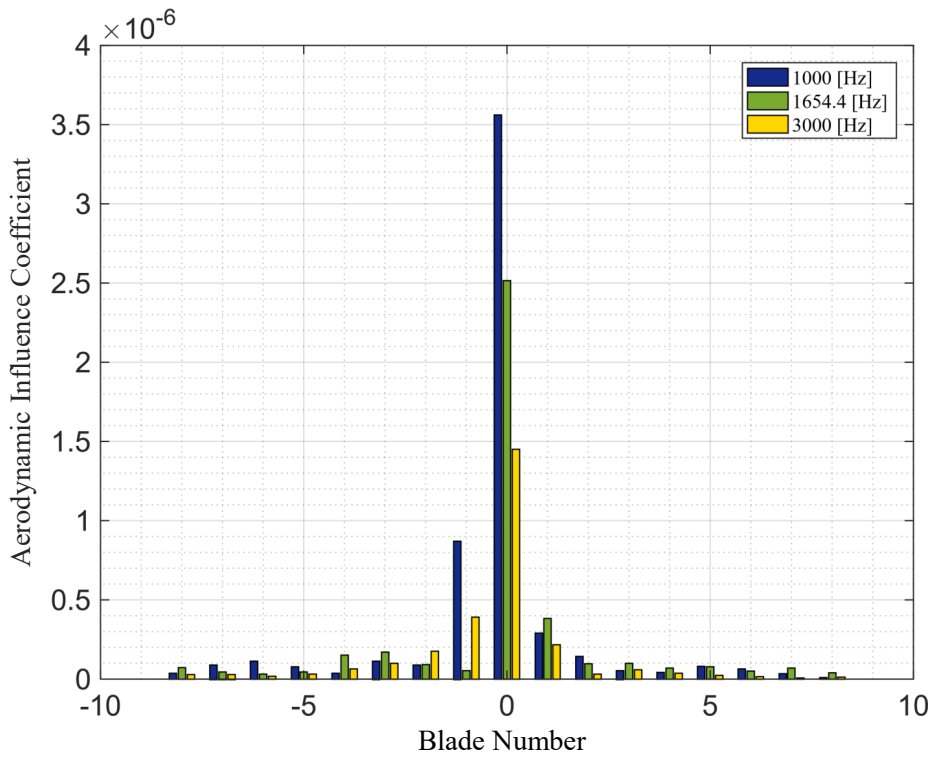


Fig. 8.2 – Blade influence coefficients of baseline rotor with different blade oscillation frequencies

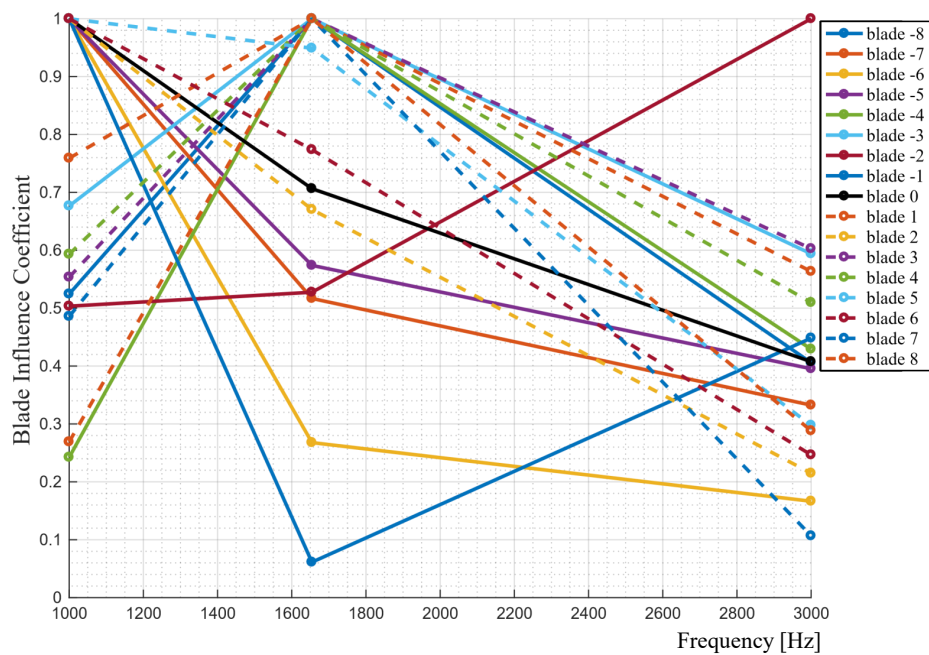


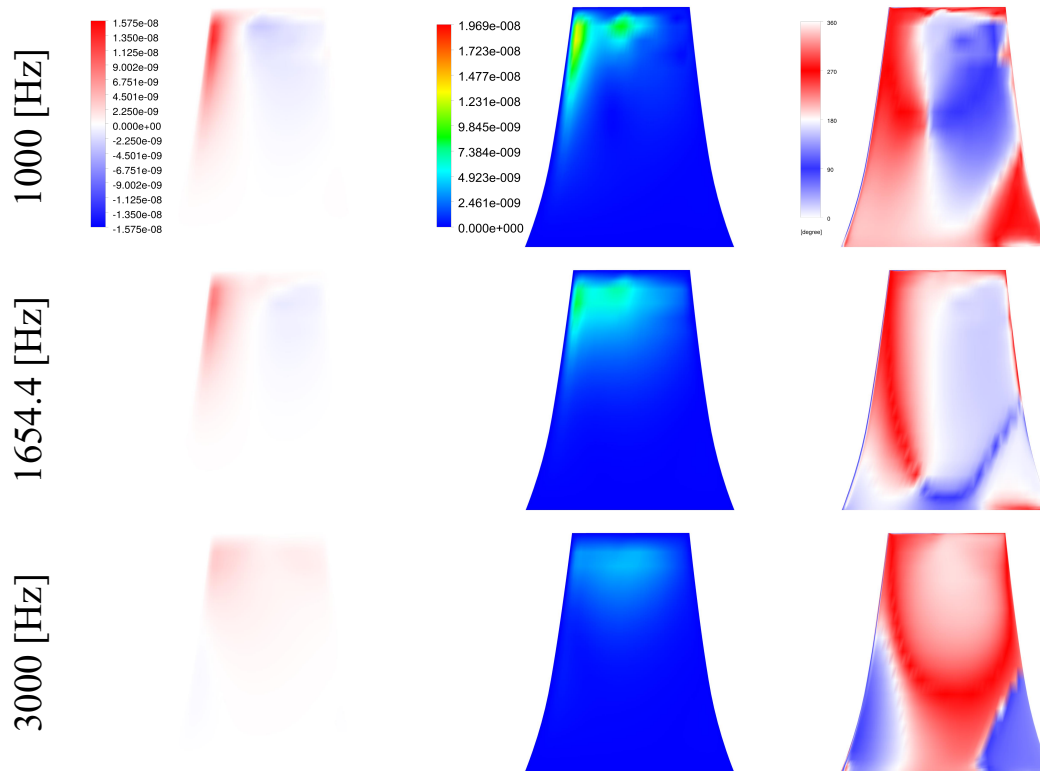
Fig. 8.3 – Variations of the normalized blade influence coefficients as a function of blade oscillation frequency, 1st bending mode

Figure 8.4 reports the local values of aerodynamic damping ratio, amplitude of the complex work per cycle and the phase shift between the complex force and complex displacement values of every node on the blade surface computed through the frequency-domain post-processing of the transient CFD results for an inter-blade phase angle of $\sigma = 0$ as it is marked on Figure 8.1.

In this figure positive values of local aerodynamic damping values, which indicate a stabilizing character of the flow, are highlighted by red color. Considering the difference in phase between the complex force and complex displacement values at every nodal location ($\phi_{\text{rotation}} = \phi_{\text{F}} - \phi_{\text{d}}$, as noted in section 5.3.1), it is worth noting that a phase shift of $\phi_{\text{rotation}} = 270^\circ$, highlighted with red, indicates a positive damping force (force and velocity in phase) where as a phase shift of $\phi_{\text{rotation}} = 90^\circ$, highlighted with blue, results in a negative damping force (force and velocity out of phase) and thus a destabilizing character of the flow.

Referring to Figure 8.4, it can be elucidated that as the oscillation frequency increases, the amplitude of the local complex work per cycle follows a decreasing trend both in magnitude and intensity which can be attributed to the the reduction of the reference blade influence coefficient as it is reported in Figure 8.2. However, comparing the cases in which the oscillation frequency is set to 1000 [Hz] and 3000 [Hz], it can be observed that in the later case although the amplitude of the local complex work per cycle is lower both on the pressure and suction sides of the blade, but with larger regions of phase shift which conform to a value of $\phi_{\text{rotation}} = 270^\circ$, the overall aerodynamic damping ratio yields a higher value.

Pressure Side



Suction Side

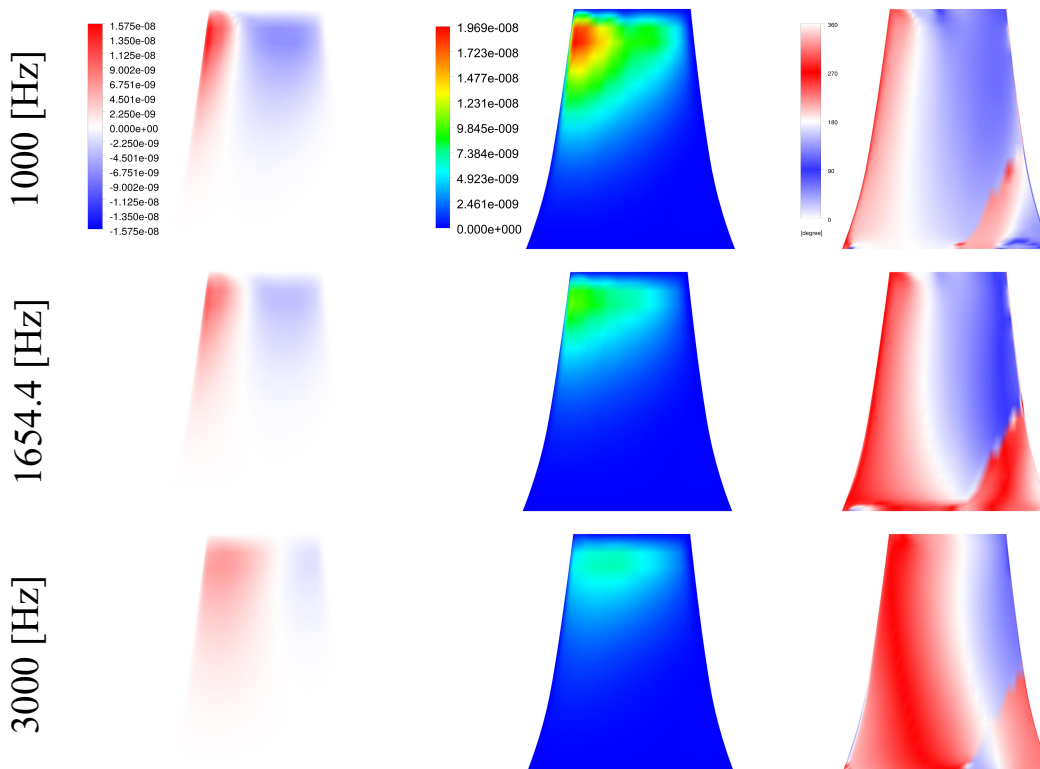


Fig. 8.4 – Local aerodynamic damping ratio (left), amplitude of the local complex work per cycle (center) and phase shift between the local complex force and complex displacement values (right) plotted on the suction and pressure side of baseline rotor blade (1^{st} bending, $\sigma = 0$)

8.2 1st Torsional Mode

In a similar manner, unsteady CFD simulations involving the 1st torsional mode of the baseline rotor blade have been performed with three different frequencies in a range of 2000 [Hz] to 6000 [Hz]. Figure 8.5, represents the characteristics S-Curve plots obtained for the three cases. It can be observed that the value of maximum aerodynamic damping ratio for the baseline case (4151.9 [Hz]), corresponds to an inter-blade phase angle of $\sigma = 0$, whereas, in case where the oscillation frequency is set to 2000 [Hz], this value conforms to a nodal diameter of 3 of forward traveling wave and has a deviation of 195.6% with respect to the baseline case. On the contrary when the blade has a vibration frequency of 6000 [Hz], the maximum aerodynamic damping ratio corresponds to a nodal diameter of 3 of backward traveling wave and has a value that is 40.2% lower compared to the baseline case.

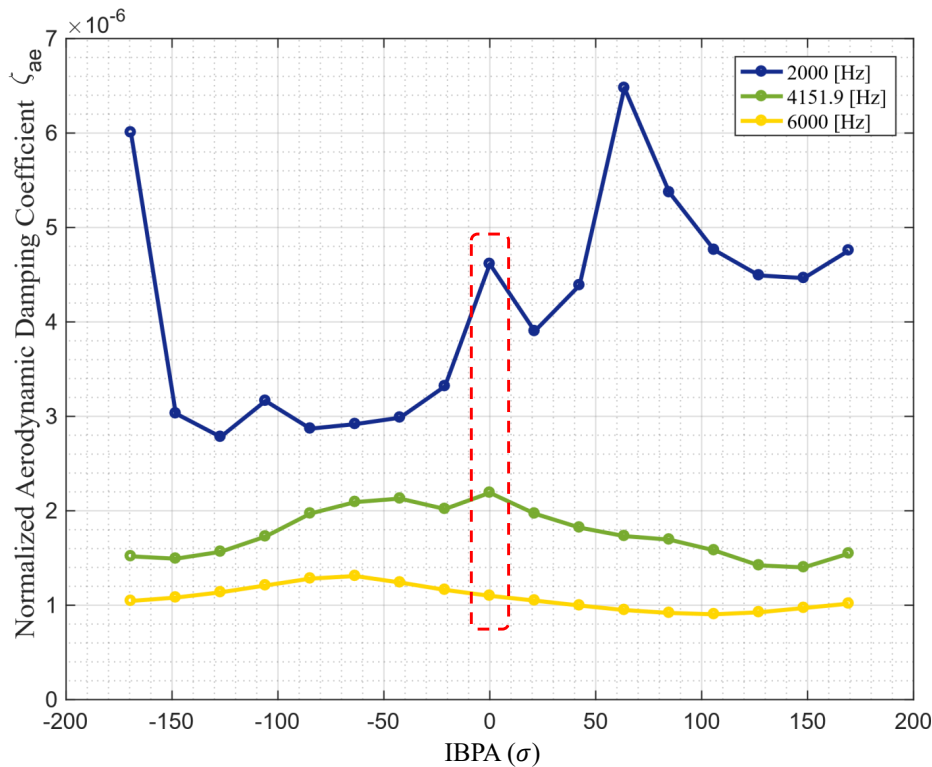


Fig. 8.5 – Characteristic S-Curve of the baseline rotor with different blade oscillation frequencies

Considering the blade influence coefficients as reported in Figure 8.6, it is noted that the influence coefficient of the central reference blade has deviations of 146.2% and -38% compared to the baseline case, when the blade oscillation frequency is set to 2000 [Hz] and 6000 [Hz] respectively.

In this case where the reference blade is oscillating at its 1st torsional mode, it is observed the value of aerodynamic damping ratio for every inter-blade phase angle, conform to a decreasing trend as the vibration frequency increases. Also similar to the 1st bending mode, the value of the influence coefficient of the central reference blade follows a decreasing trend as the frequency increases.

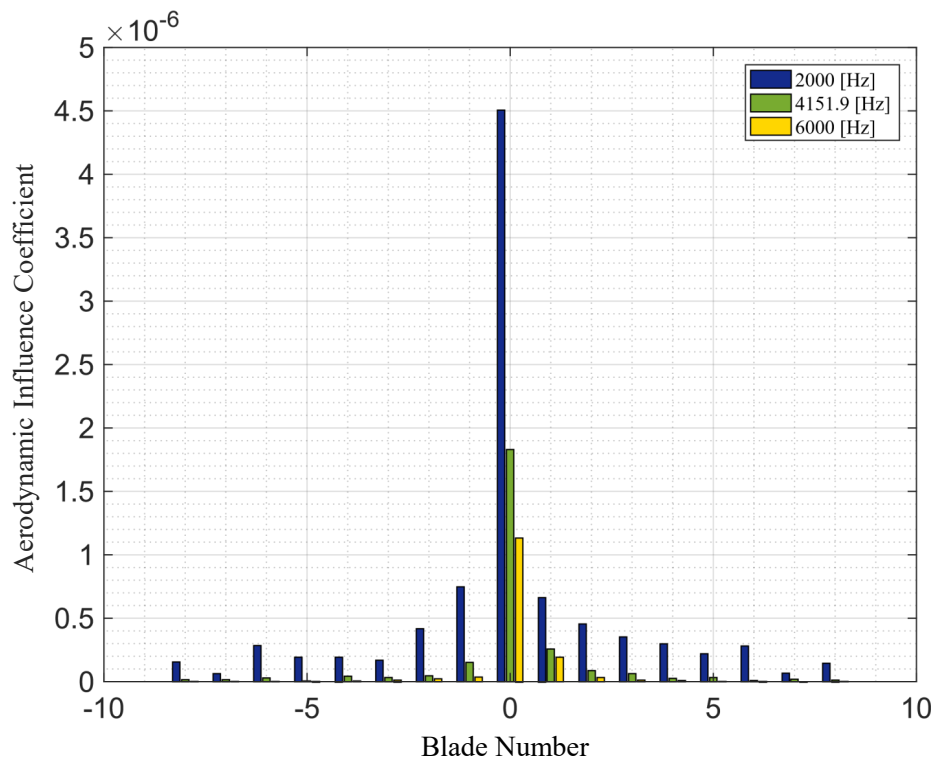


Fig. 8.6 – Blade influence coefficients of baseline rotor with different blade oscillation frequencies

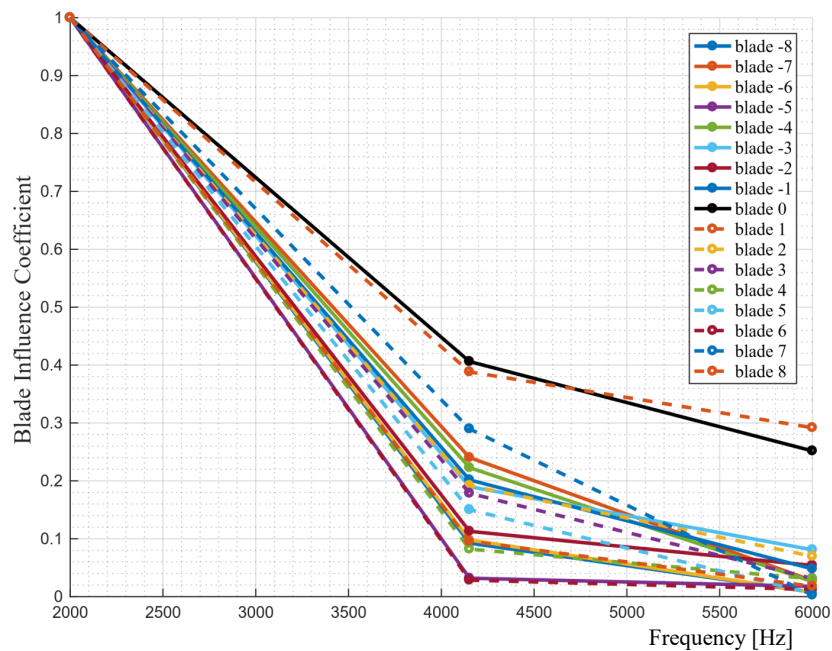


Fig. 8.7 – Variations of the normalized blade influence coefficients as a function of blade oscillation frequency, 1st torsional mode

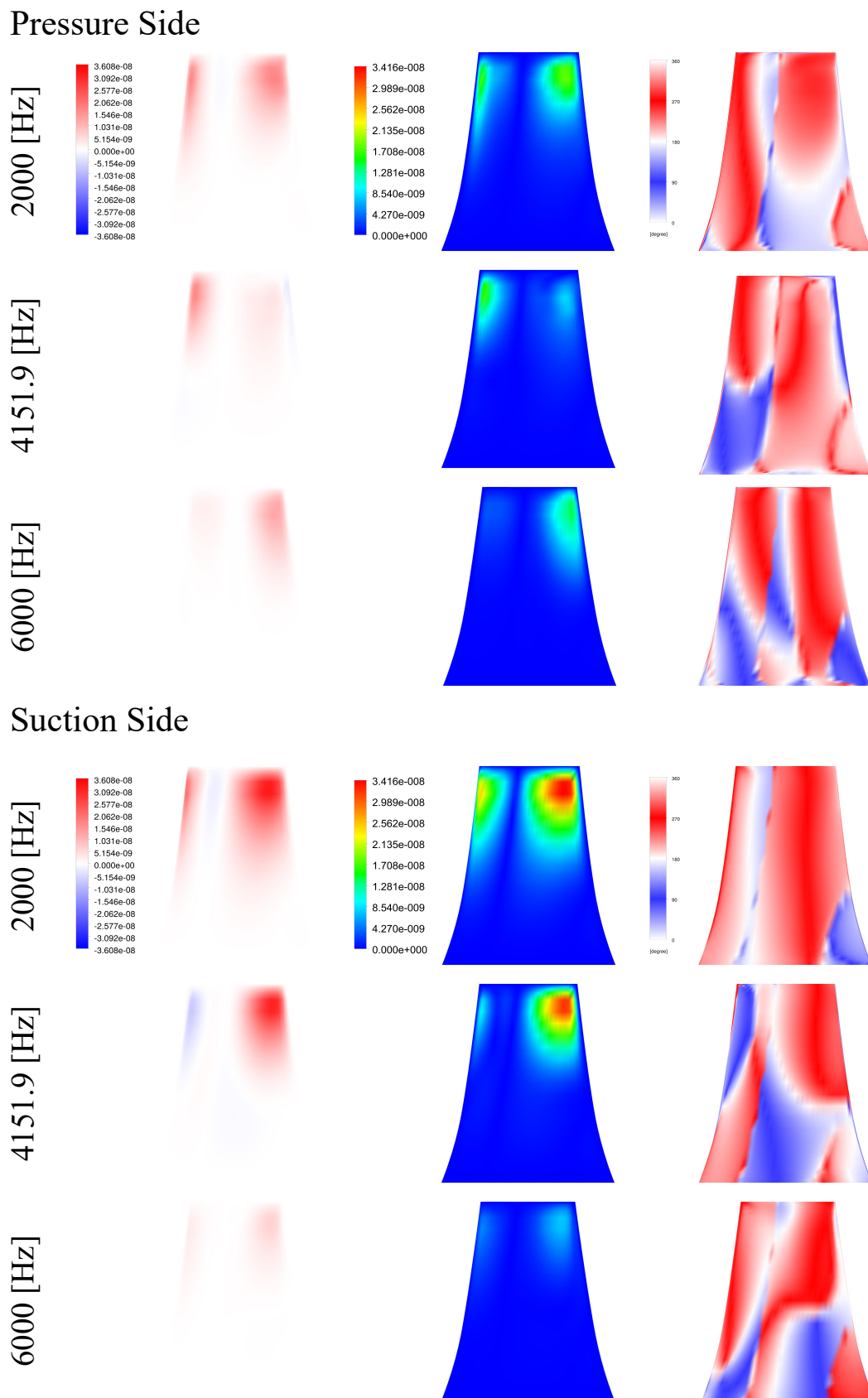


Fig. 8.8 – Local aerodynamic damping ratio (left), amplitude of the local complex work per cycle (center) and phase shift between the local complex force and complex displacement values (right) plotted on the suction and pressure side of baseline rotor blade (1st torsional, $\sigma = 0$)

Figure 8.7 illustrates the variations of normalized blade influence coefficients as a function of vibration frequency for the 1st torsional mode. Unlike the 1st bending mode, in this case a decreasing trend can be clearly detected for the influence coefficients as the vibration frequency increases.

Figure 8.8 illustrates the local values of aerodynamic damping ratio, amplitude of the complex work per cycle and the phase shift between the complex force and complex displacement values of every node on the blade surface when the blades are oscillating at their 1st torsional mode with an inter-blade phase angle of $\sigma = 0$ as it is marked on Figure 8.5.

It is noted that in a similar manner to the 1st bending mode, when the the blades are oscillating at their 1st torsional mode, as the oscillation frequency increases, the amplitude of the local complex work per cycle follows a decreasing trend both in magnitude and intensity which is in consistency with the decreasing trend of the blade influence coefficients as it is reported in Figure 8.7.

Comparing the cases in which the oscillation frequency is set to 2000 [Hz] and 6000 [Hz], it can be observed that in both of the cases the largest values of the amplitude of local complex work per cycle conform to the regions with a phase shift of $\phi_{\text{rotation}} = 270^\circ$, and consequently the overall value of the aerodynamic damping ratio is positive which results in a stabilizing character of the flow. As a result unlike the 1st bending mode, at an inter-blade phase angle of $\sigma = 0$, in this case the overall value of the aerodynamic damping ratio decreases as the oscillation frequency increases.

In general it can be elucidated that the oscillation frequency has a significant influence on the value of aerodynamic damping ratio calculated for every inter-blade phase angle and thus the shape of the derived characteristics S-Curve as it influences both the amplitude of the local complex work per cycle and the phase shift between the local complex force and complex displacement values.

9 Influence of Blade Count on Aerodynamic Damping

With the aim of investigating the influence of geometrical parameters on the aeroelastic stability, two different cases including “variable blade count” and “variable trailing edge angle”, are considered within the present work. In this regard modifications are performed on the baseline rotor in order to obtain new design. Following a structural analysis of each case, unsteady CFD simulations are performed through the influence coefficients method and the obtained results are compared in order to find a possible trend correlating the geometrical modifications and the aerodynamic damping ratio.

Blade count ratio (BCR), i.e. the ratio of blade counts of two adjacent rows in a stage, is a design parameter which can be implied in order to avoid Campbell crossing in turbomachinery applications [14]. In this study though, for the isolated fan rotor under investigation, the blade count is varied in order to investigate its influence on aerodynamic damping ratio.

9.1 Scaling Technique

Blade count variation is achieved by scaling the baseline blade with a fixed chord-to-pitch ratio (solidity) through a scaling technique reported in [15]. Thus a blade scaling factor Sf is introduced as

$$Sf = \frac{N_{NB, \text{baseline}}}{N_{NB, \text{scaled}}} \quad (9.1)$$

The baseline blade is then scaled in the axial and circumferential coordinates only, preserving the blade solidity. In this sense with the blade loading remaining unchanged, the effects on the steady-state aerodynamic performance will be minimal.

$$\begin{aligned} Z_{\text{sclaed}} &= Sf \cdot Z_{\text{baseline}} \\ \theta_{\text{sclaed}} &= Sf \cdot \theta_{\text{baseline}} \\ R_{\text{sclaed}} &= R_{\text{baseline}} \end{aligned} \quad (9.2)$$

Figure 9.1 illustrates profiles of blades with various blade count that are obtained after scaling the baseline line rotor blade. It should be mentioned that in order to minimize the effect of scaling on steady aerodynamics, the stacking of the profiles has been altered in such a manner that the leading edge blade angle is preserved.

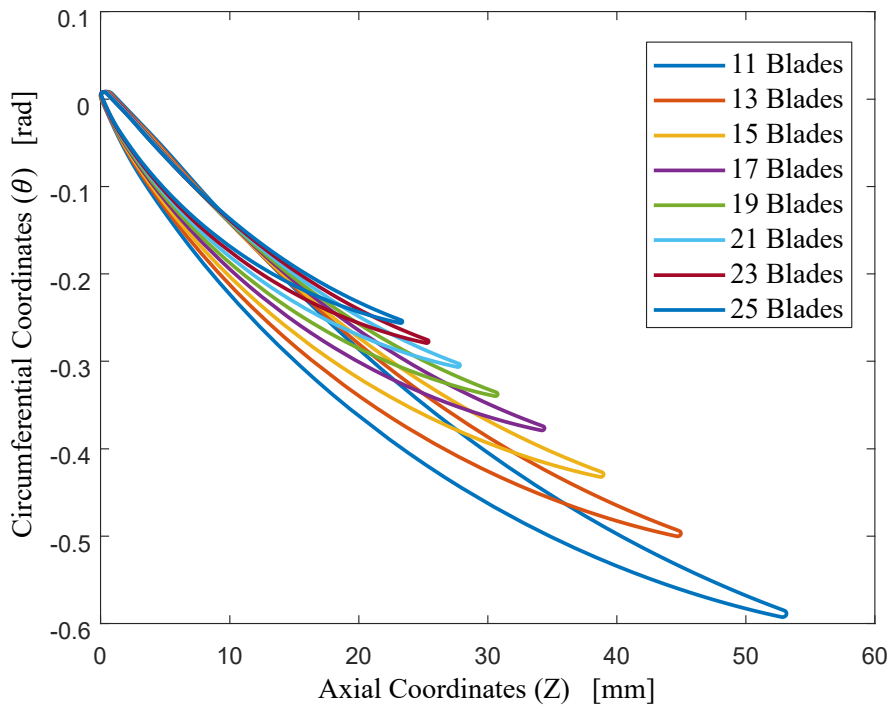


Fig. 9.1 – Blade hub profile of modified rotors with various blade count

9.2 Modal Analysis

In order to explore the influence of scaling on the mode frequency and mode shapes of the modified blades, a modal analysis has been performed as described in chapter 6. Figure 9.2 illustrates the two first mode shapes of the baseline rotor blade as well as the modified blades.

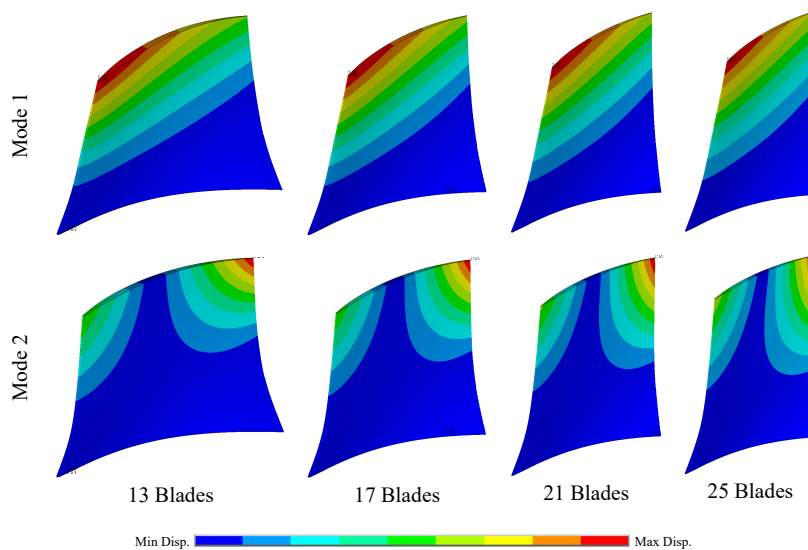


Fig. 9.2 – A graphical representation of the 1st bending and the 1st torsional modes of different blades corresponding to rotors with variable blade count

Further more to investigate the influence of scaling on the mode shapes of modified blades, a modal assurance criteria (MAC-Index) has been computed for the mode shapes obtained from FEM analysis as

$$MAC = \frac{\left| \left\{ \Phi_{x,scaled} \right\}^T \left\{ \Phi_{x,baseline} \right\} \right|^2}{\left(\left\{ \Phi_{x,scaled} \right\}^T \left\{ \Phi_{x,scaled} \right\} \right) \left(\left\{ \Phi_{x,baseline} \right\}^T \left\{ \Phi_{x,baseline} \right\} \right)} \quad (9.3)$$

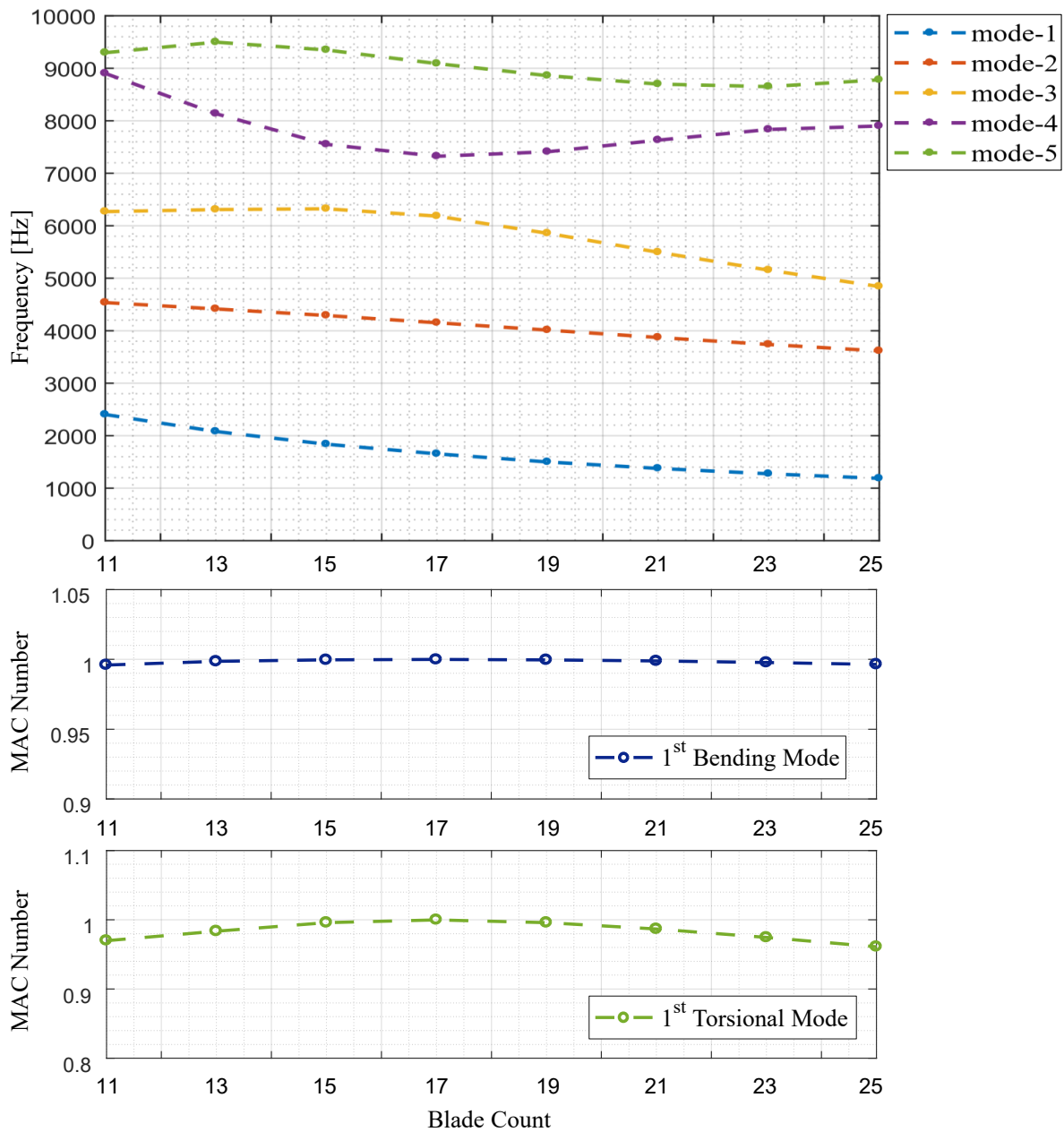


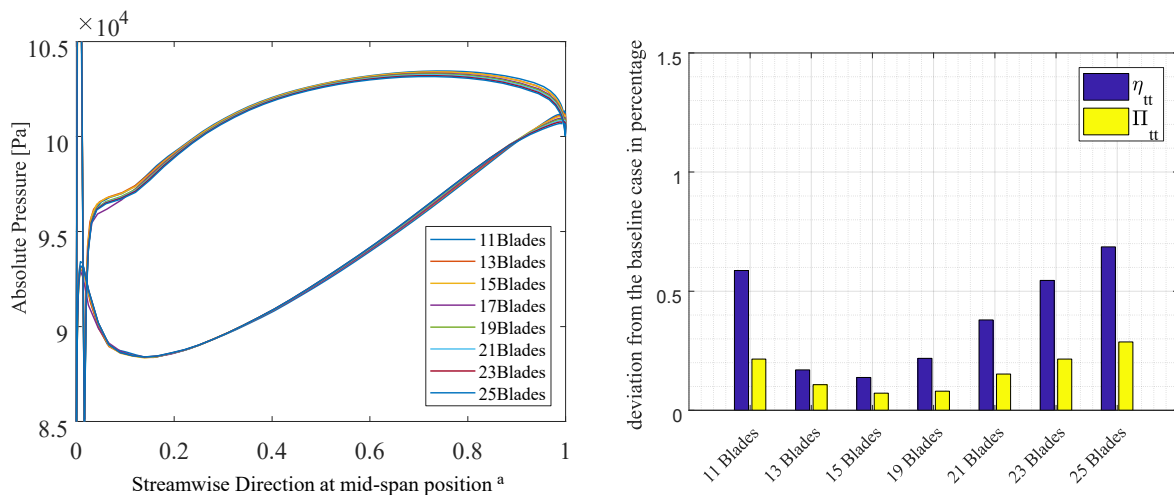
Fig. 9.3 – Comparison of eigen-frequencies and MAC numbers for different blades corresponding to rotors with variable blade count

It is worth noting that in order to calculate the MAC index, having performed the modal analysis, the nodal locations of the modified blades have been scaled back by a factor of $\frac{1}{\sqrt{f}}$, so that a mapping of the modal vectors can be performed over the nodal locations of the baseline rotor blade.

The diagrams in Figure 9.3 report variations of eigen-frequencies corresponding to the first 5 vibration modes and the modal assurance criteria as a function of blade count of the various rotors. It is observed that regarding the 1st bending mode and the 1st torsional mode which are of importance to the present work, the eigen-frequencies follow a decreasing trend as the blade count increases. On the other hand though, considering the MAC numbers with values close to unity for all of the cases, it can be elucidated that the influence of scaling on the mode shapes is of negligible order.

9.3 Steady State Analysis

Considering the scaling method introduced in section 9.1, it is expected that the steady state aerodynamic performance of the modified geometries will be consistent with the baseline design. Thus steady state simulations have been performed for all of the modified cases in ANSYS CFX according to the same CFD setup and mesh resolution, described in section 7.1. Figure 9.4, represents the obtained results in a comparative manner for all the cases. In this figure, blade loadings are plotted at the midspan position for all the cases. Also deviations of the total-to-total efficiency and compression ratio with respect to the baseline rotor design is reported. Comparing the overall results, it can be elucidated that with minimal changes in the operating conditions of the modified geometries with various blade count, the steady aerodynamics is preserved.



a) based on meridional coordinate, following the blade surface and normalized with 0 at the leading edge and 1 at the trailing edge of blade

Fig. 9.4 – Blade loadings plot (left) and steady-state aerodynamic performance variations (right) compared for different cases

9.4 Unsteady CFD Analysis

In order to investigate the influence of blade count on the aerodynamic damping ratio, unsteady CFD analyses have been performed. For this purpose, three cases with 13, 21 and 25 blades have been picked to be compared with the baseline rotor which consists of 17 blades. In this regards, all of the mentioned configurations have been subjected to transient CFD simulation using the influence coefficients method, for both the 1st bending mode and the 1st torsional mode.

According to results obtained in the previous section, variations in the blade count have the major impact on oscillation frequency rather than the mode shape. Thus with the aim of gaining a detailed insight into the influence of mode-shape on the overall aerodynamic damping ratio two series of CFD simulations have been conducted. Within the first series of simulations, blade oscillations involve the eigen-frequency computed through the modal analysis corresponding to each individual case. Meanwhile in the second series of CFD simulations, blade vibrations in all of the different configurations take place at eigen-frequency of the baseline rotor which correspond to the mode shape being investigated.

Influence coefficients method analyses have been conducted through a computational setup as described in section 7.2 with similar boundary conditions and a computational domain which includes the whole rotor passages without a need for periodic boundaries. In table 9.1 an overview of the unsteady simulation parameters and the overall computational effort is reported.

Table 9.1 – An overview of unsteady CFD setups and computational effort for different cases

| Case Name | Blade Count | Number of Elements | Mode Shape | Frequency [Hz] | Computation Time [CPU-Hours] |
|------------------------|-------------|--------------------|---------------|----------------|------------------------------|
| NB13 1st EF | 13 | 8868900 | 1st Bending | 2080.28 | 18900 |
| NB13 1st UF | 13 | 8868900 | 1st Bending | 1654.36 | 18900 |
| NB13 2nd EF | 13 | 8868900 | 1st Torsional | 4415.35 | 18900 |
| NB13 2nd UF | 13 | 8868900 | 1st Torsional | 4151.91 | 18900 |
| NB21 1st EF | 21 | 14063200 | 1st Bending | 1376.86 | 31500 |
| NB21 1st UF | 21 | 14063200 | 1st Bending | 1654.36 | 31500 |
| NB21 2nd EF | 21 | 14063200 | 1st Torsional | 3871.51 | 31500 |
| NB21 2nd UF | 21 | 14063200 | 1st Torsional | 4151.91 | 31500 |
| NB25 1st EF | 25 | 16741900 | 1st Bending | 1187.36 | 34600 |
| NB25 1st UF | 25 | 16741900 | 1st Bending | 1654.36 | 34600 |
| NB25 2nd EF | 25 | 16741900 | 1st Torsional | 3615.48 | 34600 |
| NB25 2nd UF | 25 | 16741900 | 1st Torsional | 4151.91 | 34600 |
| Total Computation Time | | | | | 340000 |

9.5 Results

With convergence being reached after approximately 40 period, a post-processing procedure has been conducted on each result file as described in section 5.3.1, to obtain the characteristic S-Curves and to extract the blade influence coefficients. In addition to the S-Curve plots and blade influence coefficient diagrams, local aerodynamic damping ratios are plotted on the blade surface as well as the amplitude and phase of the normalized complex work per cycle which yield from the frequency-domain post-processing of the transient CFD results.

9.5.1 1st Bending Mode (Blades Vibrating at Different Frequencies)

Figure 9.5 illustrates the obtained characteristic S-Curves for rotors of various blade count vibrating with the 1st bending mode shape at frequencies derived through modal analysis for each individual case. It is observed that in case of the rotor with 13 blades, the value of minimum damping which corresponds to a nodal diameter of 1 of backward traveling wave is 0.17% higher compared to the baseline rotor. Meanwhile for rotors consisting of 21 and 25 blades, minimum damping ratios correspond to nodal diameters of 4 and 3 of forward traveling wave respectively. Also for the later cases minimum damping ratio values increase by 94% and 115% respectively.

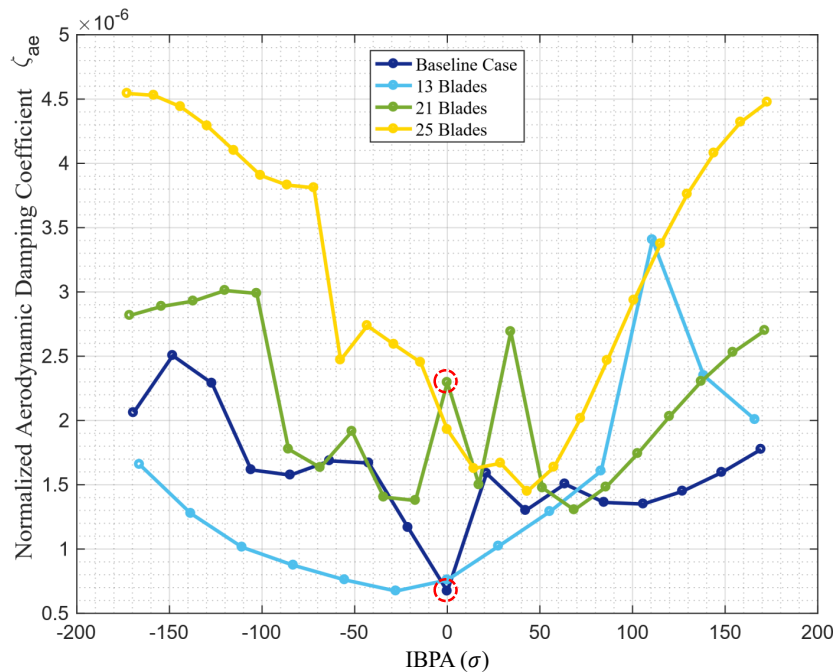


Fig. 9.5 – S-Curve for rotors with various blade count oscillating in different frequencies

Figure 9.6 on the other hand, reports the extracted influence coefficients of the individual blades. As the number of blades increase from 17 to 25, the value of influence coefficient of the central reference blade increases by 26.5% and 83% respectively. On the contrary this value is decreased by 37.7% for the rotor of 13 blades.

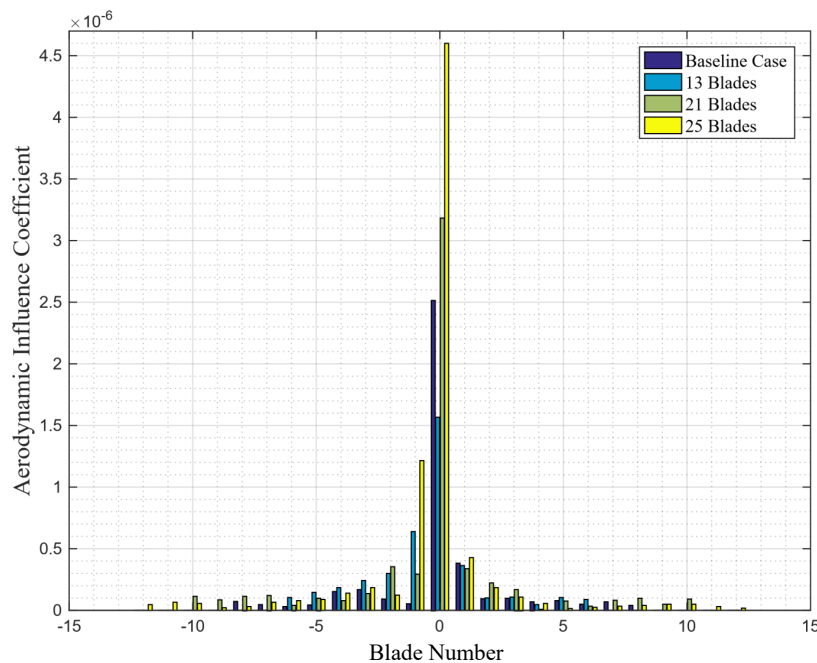


Fig. 9.6 – Blade influence coefficients for rotors with various blade count oscillating in different frequencies

Figure 9.7 reports the local values of aerodynamic damping ratio, amplitude of the complex work per cycle and the phase shift between the complex force and complex displacement values of every node on the blade surface computed through the frequency-domain post-processing of the transient CFD results for an inter-blade phase angle of $\sigma = 0$ as it is marked on Figure 9.5.

In this figure positive values of local aerodynamic damping values, which indicate a stabilizing character of the flow, are highlighted by red color. Considering the difference in phase between the complex force and complex displacement values at every nodal location ($\phi_{\text{rotation}} = \phi_F - \phi_d$, as noted in section 5.3.1), it is worth noting that a phase shift of $\phi_{\text{rotation}} = 270^\circ$, highlighted with red, indicates a positive damping force (force and velocity in phase) whereas a phase shift of $\phi_{\text{rotation}} = 90^\circ$, highlighted with blue, results in a negative damping force (force and velocity out of phase) and thus a destabilizing character of the flow.

It can be elucidated that in the regions of the blade surface above the mid-span position towards the blade tip, the largest values of the amplitude of local complex work per cycle conform to the regions with a phase shift of $\phi_{\text{rotation}} = 270^\circ$, and consequently the overall value of the aerodynamic damping ratio is positive which results in a stabilizing character of the flow.

Figure 9.8, illustrates similar plots for the modified rotor consisting of 21 blades. It is noted that compared to the baseline case, with the values of the phase shift being close to $\phi_{\text{rotation}} = 270^\circ$ on the upper regions of the pressure side of the blade, there are no regions of negative damping present.

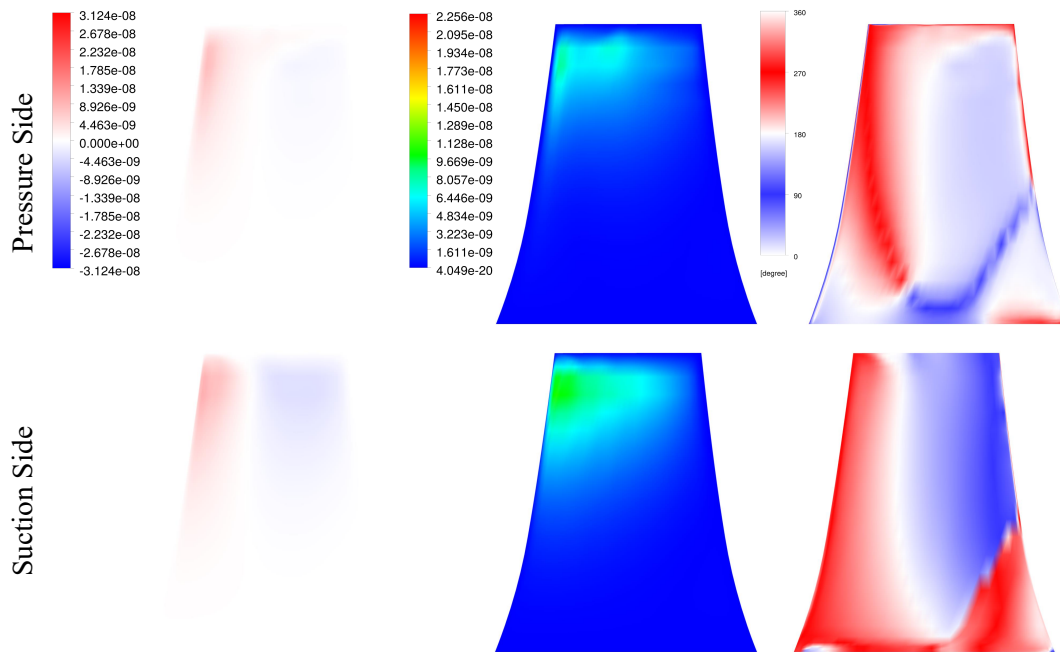


Fig. 9.7 – Local aerodynamic damping ratio (left), amplitude of the local complex work per cycle (center) and phase shift between the local complex force and complex displacement values (right) plotted on the suction and pressure side of baseline rotor blade (mode 1, $\sigma = 0$)

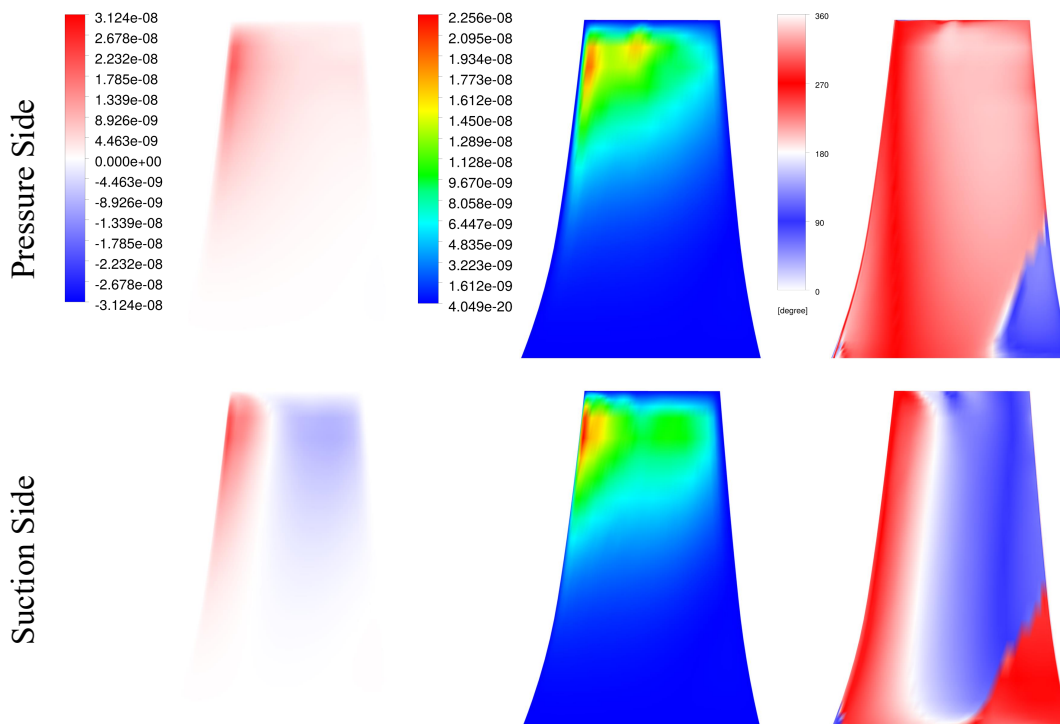


Fig. 9.8 – Local aerodynamic damping ratio (left), amplitude of the local complex work per cycle (center) and phase shift between the local complex force and complex displacement values (right) plotted on the suction and pressure side of the modified rotor with 21 blades (mode 1, $\sigma = 0$)

The plots in Figure 9.9 represent the difference in phase between the values of local complex force and complex displacement of every nodal location on the pressure side of the central reference blade for the modified rotor of 25 blades. As it is illustrated in the figure, some of abrupt changes of phase in the blade tip region can be attributed to the tip vortex arising from the tip of the neighbouring blade.

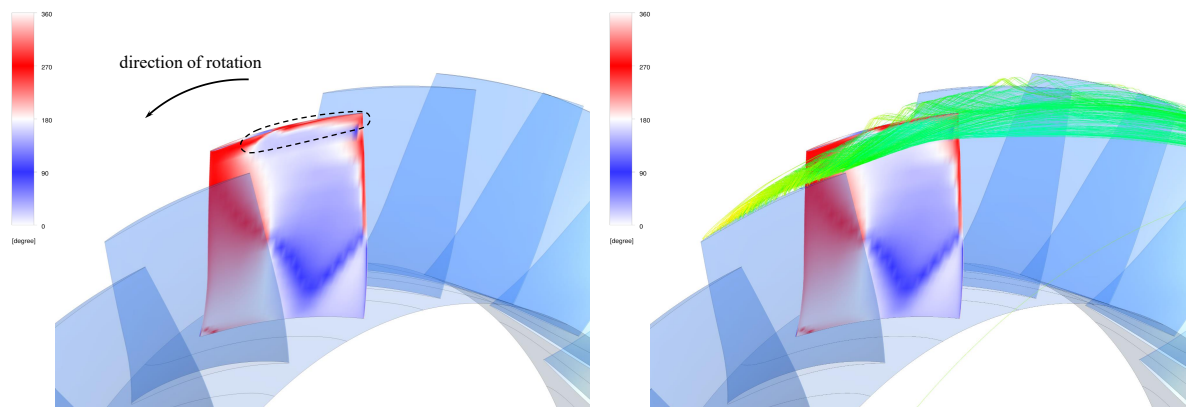


Fig. 9.9 – Phase shift between the local complex force and complex displacement values plotted on the pressure side of modified rotor consisting of 25 blades (mode 1, $\sigma = 0$)

Figure 9.10 illustrates the difference in phase between local complex force and complex displacement values on the suction side as well as local wall shear stress values. Similar abrupt changes of the phase are noticed in the regions close to the blade hub as it is highlighted in Figure 9.10. However in this region very low values of wall shear stress indicates regions of flow separation which could be contributing to the changes in the local phase shift values.

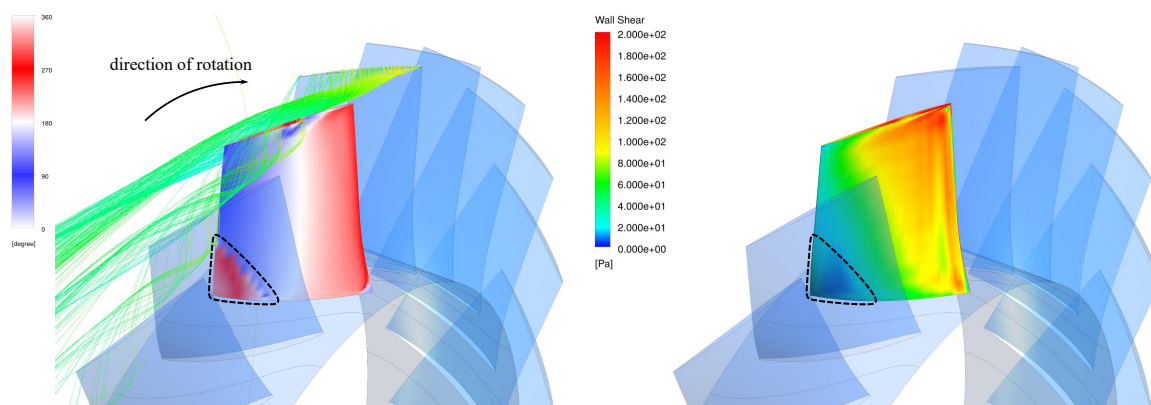


Fig. 9.10 – Phase shift between the local complex force and complex displacement values (left) and the local wall shear stress values (right) plotted on the suction side of modified rotor consisting of 25 blades (mode 1, $\sigma = 0$)

9.5.2 1st Bending Mode (Blades Vibrating at the Same Frequency)

The diagrams in figures 9.11 and 9.12, report the characteristics S-Curve and blade influence coefficients for the case in which blade oscillation frequency is set to that of the baseline rotor for all of the different rotors of various blade count. Regarding the S-Curve plot, it is elucidated that in this case the value of minimum damping ratio corresponds to an inter-blade phase angle of $\sigma = 0$ and it follows an increasing trend as the blade count increases. According to this plot the value of minimum damping is 16.5% and 34.3% higher for with rotors of 21 and 25 blades compared to the baseline design, whereas this value is 14% lower for the rotor of 13 blades.

Also a similar trend is observed concerning the influence coefficient of the central blade with variations of -10% , 14.3% and 31% for the rotors of 13, 21 and 25 blades respectively compared to the baseline rotor design.

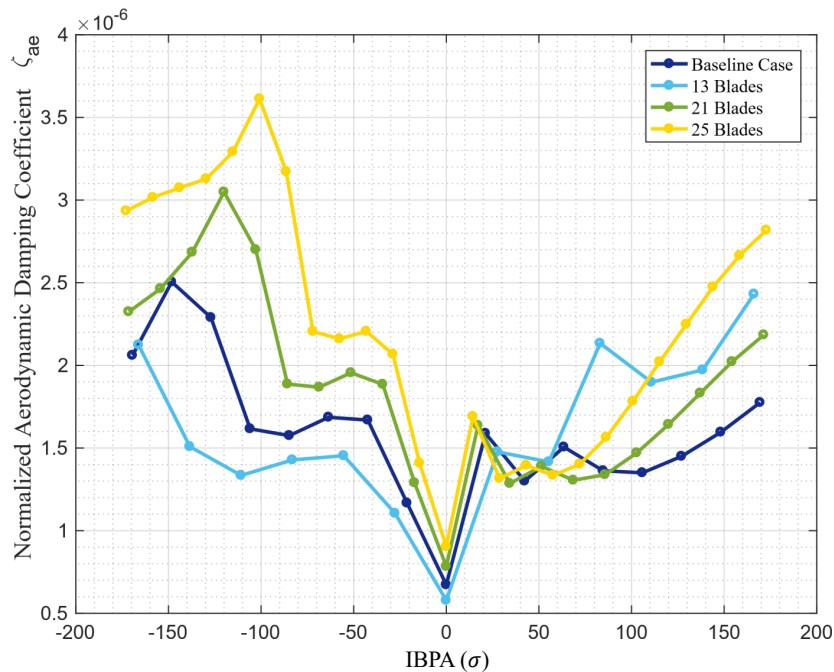


Fig. 9.11 – S-Curve for rotors with various blade count oscillating in same frequency

Figure 9.13 and Figure 9.14, show the local values of aerodynamic damping ratio, amplitude of the complex work per cycle and the phase shift between the complex force and complex displacement values of every node on both suction and pressure sides of blade surface for the rotors of 17 and 25 blades respectively. Considering the phase shift plots in the two figures, it is noted that unlike the case where the blades were oscillating with different frequencies, in this case though a similar trend can be detected for both of the blades on pressure side as well as the suction side. Regarding the amplitude of the local complex work per cycle however, in case of the rotor with 25 blades some regions with larger magnitudes are detected compared to the baseline rotor. This can be attributed to the smaller pitch values and thus more closely spaced blades as the blade count increases and consequently larger influence coefficients as seen in Figure 9.12.

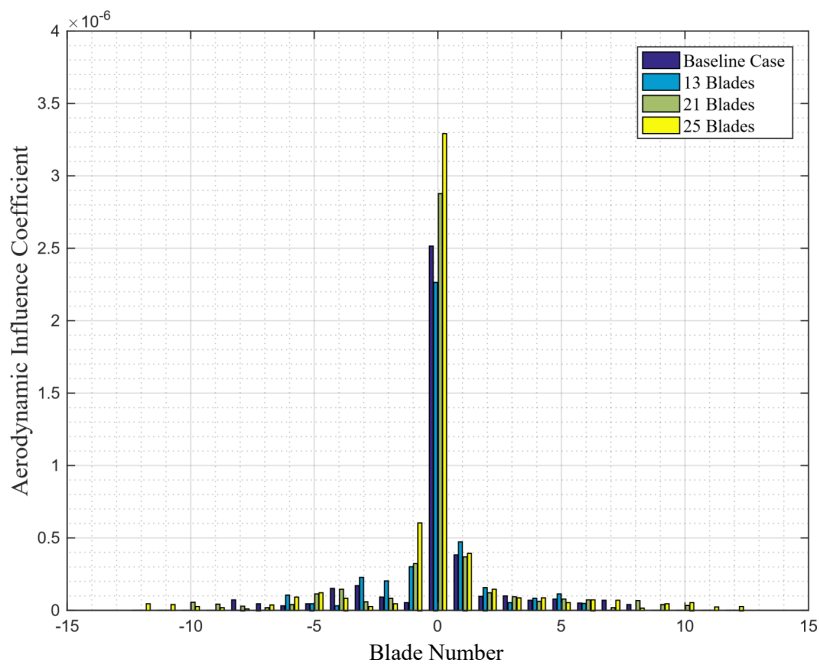


Fig. 9.12 – Blade influence coefficients for rotors with various blade count oscillating in same frequency

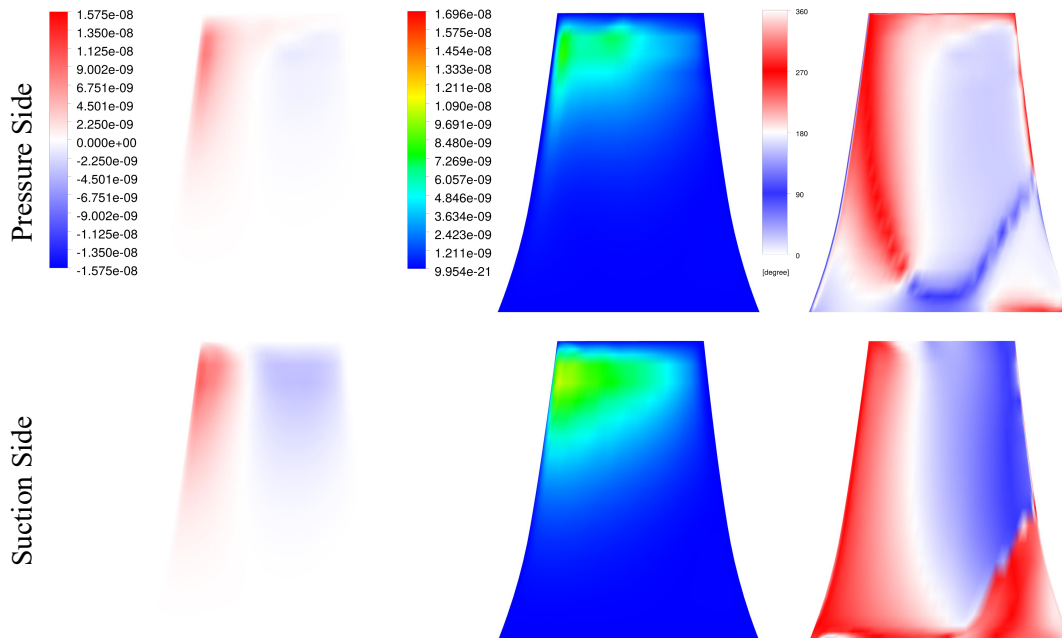


Fig. 9.13 – Local aerodynamic damping ratio (left), amplitude of the local complex work per cycle (center) and phase shift between the local complex force and complex displacement values (right) plotted on the suction and pressure side of baseline rotor blade (mode 1, $\sigma = 0$)

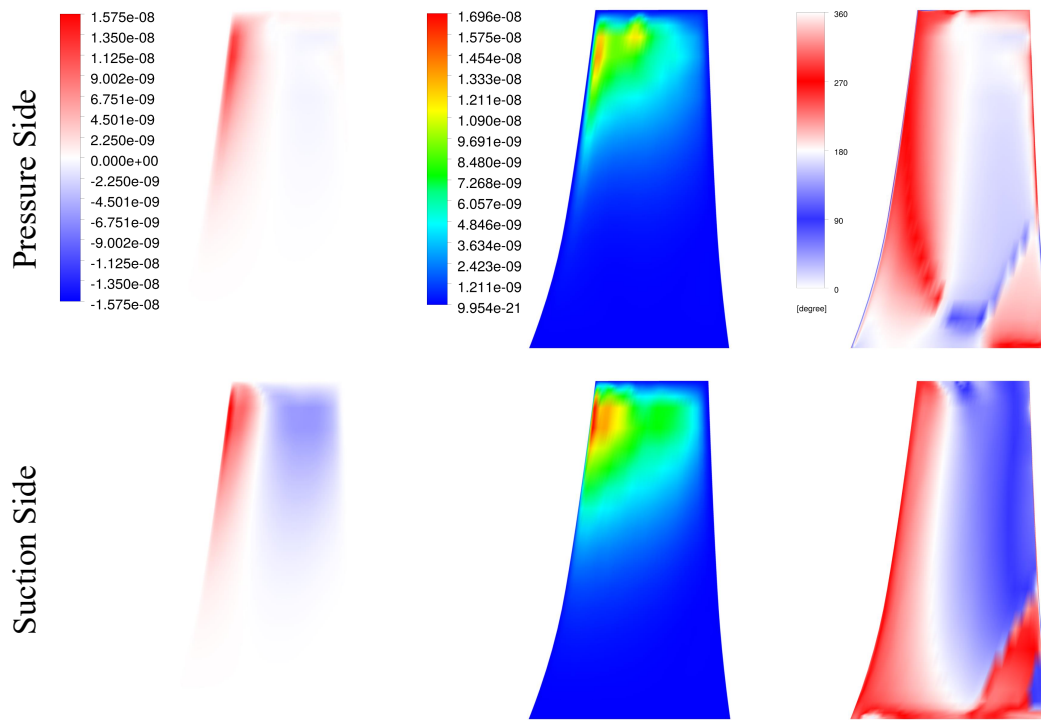


Fig. 9.14 – Local aerodynamic damping ratio (left), amplitude of the local complex work per cycle (center) and phase shift between the local complex force and complex displacement values (right) plotted on the suction and pressure side of the modified rotor with 25 blades (mode 1, $\sigma = 0$)

9.5.3 1^{st} Torsional Mode (Blades Vibrating at Different Frequencies)

Figure 9.15, reports the S-Curve corresponding to the rotors of various blade count vibrating with the 1^{st} torsional mode shape at frequencies derived through modal analysis for each individual case. According to this diagram, the value of minimum damping ratio for rotors of 13, 17 and 21 blades corresponds to nodal diameters of 1, 7 and 6 of forward traveling wave respectively, whereas in case of the rotor with 25 blades minimum damping ratio takes place at a nodal diameter of 11 of backward traveling wave. Also the deviations of value of minimum damping ratios from the baseline case equals to -23% , 23% and 70.4% for rotors of 13, 21 and 25 blades respectively.

In general as the blade count increases an increase in the value of aerodynamic damping ratio is observed for all nodal diameters. However though in case of the rotor with 25 blades a significant increase in the value of aerodynamic damping ratio for nodal diameters of 6 to 10 of forward traveling wave is detected.

Considering Figure 9.16, which illustrates the blade influence coefficients, a similar trend can be observed as the influence coefficient of the central reference blade increases with increasing number of blade count. Deviations in the value of influence coefficient of the central reference blade compared to the baseline case are -29% , 30.5% and 108% for the rotors of 13, 21 and 25 blades respectively.

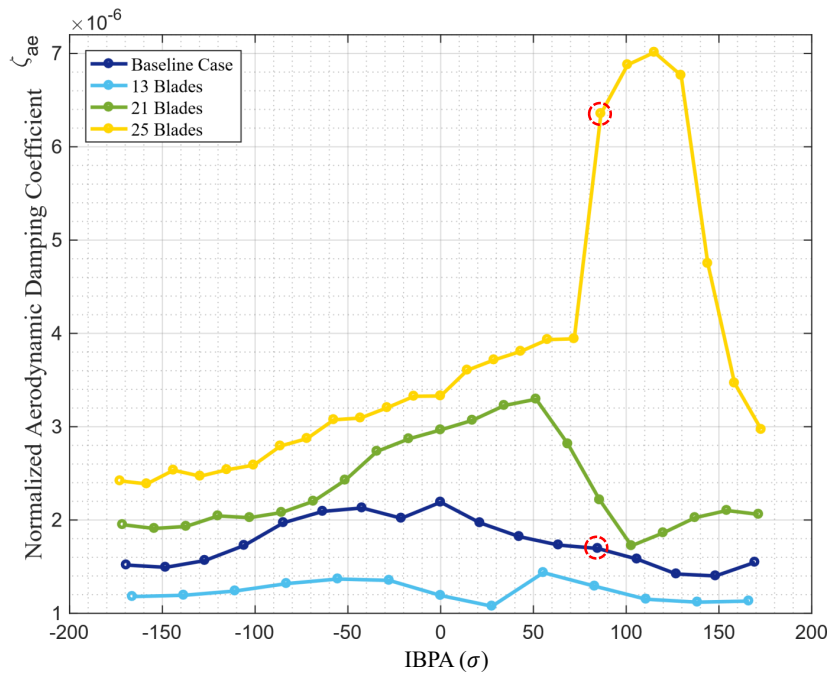


Fig. 9.15 – S-Curve for rotors with various blade count oscillating in different frequencies

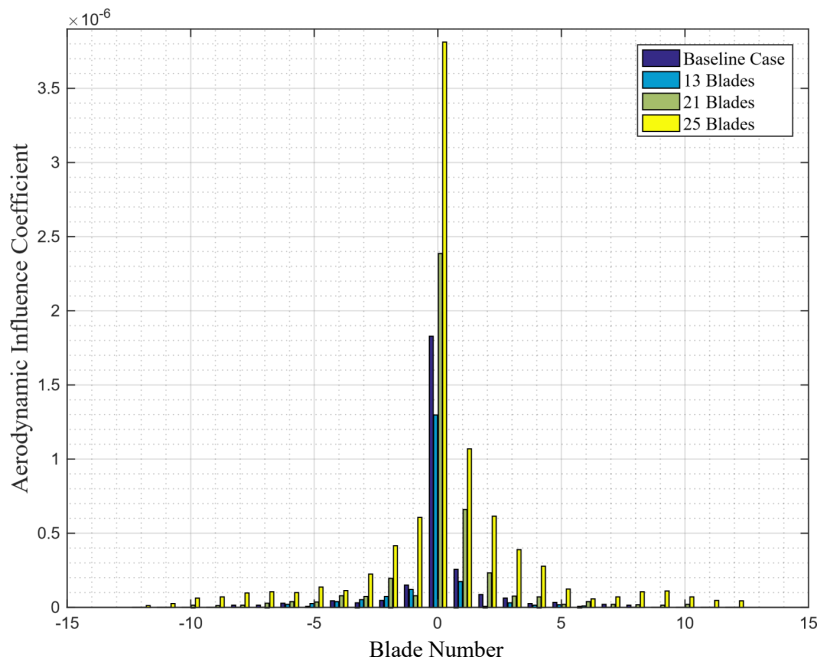


Fig. 9.16 – Blade influence coefficients for rotors with various blade count oscillating in different frequencies

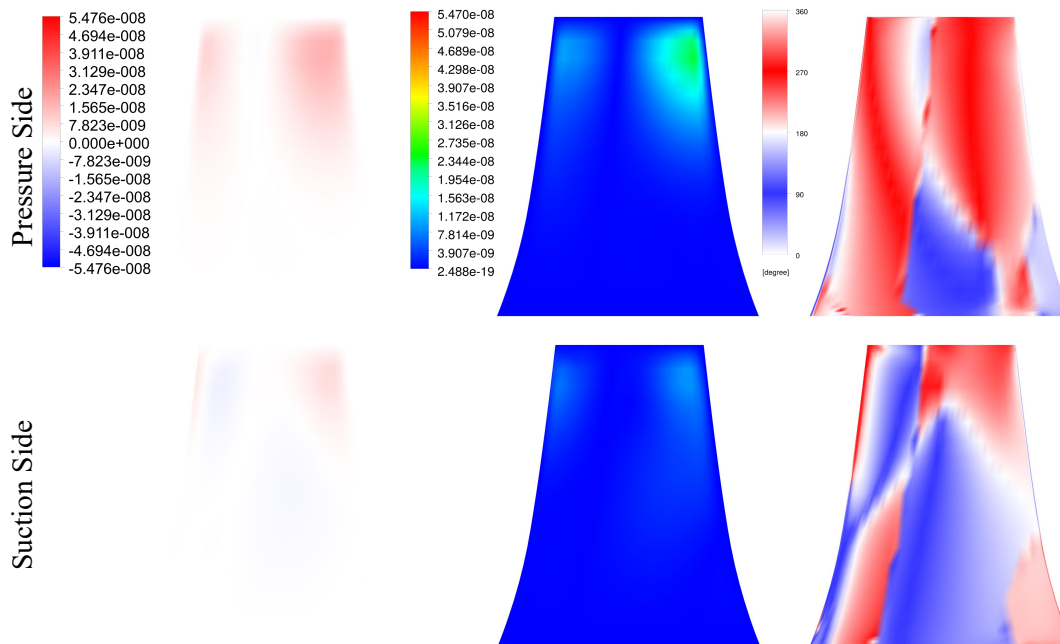


Fig. 9.17 – Local aerodynamic damping ratio (left), amplitude of the local complex work per cycle (center) and phase shift between the local complex force and complex displacement values (right) plotted on the suction and pressure side of baseline rotor blade (mode 2, $\sigma = 84.7$)

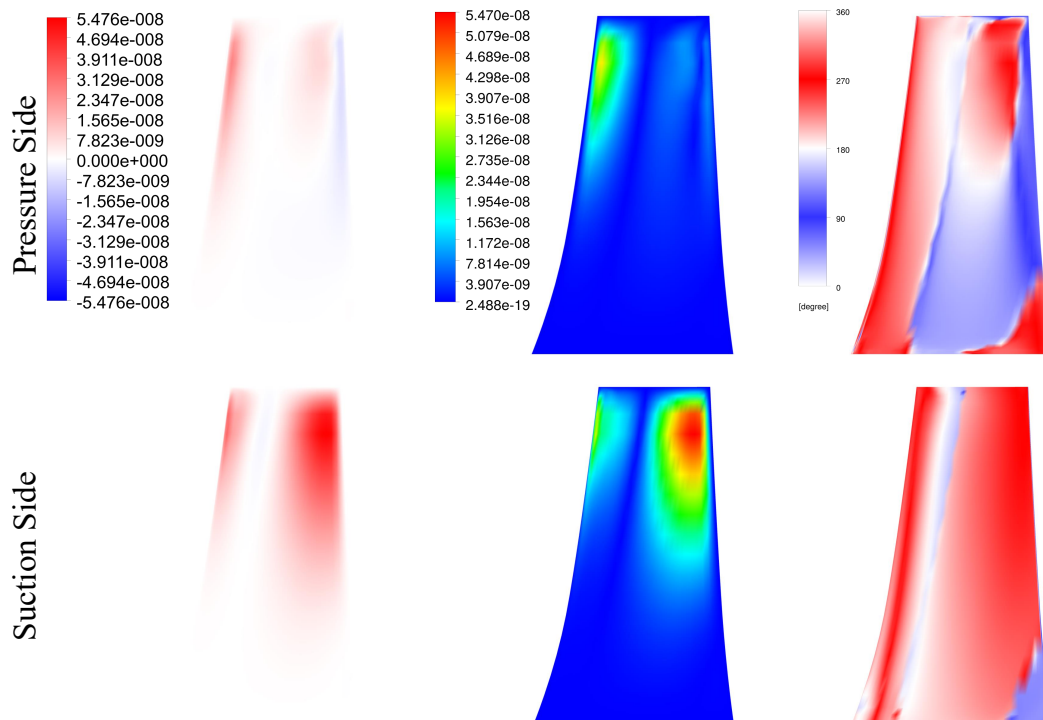


Fig. 9.18 – Local aerodynamic damping ratio (left), amplitude of the local complex work per cycle (center) and phase shift between the local complex force and complex displacement values (right) plotted on the suction and pressure side of the modified rotor with 25 blades (mode 2, $\sigma = 100.8$)

Figure 9.17 illustrates the local values of aerodynamic damping ratio, amplitude of the complex work per cycle and the phase shift between the complex force and complex displacement values for the baseline rotor case which is oscillating at a nodal diameter of 4 of forward traveling wave ($\sigma = 84.7$) as it is marked on Figure 9.15. On the other hand Figure 9.18 reports similar plots for the rotor consisting of 25 blades oscillating at a nodal diameter of 6 of forward traveling wave ($\sigma = 100.8$).

Considering the two figures mentioned, it is observed that in case of the rotor with 25 blades, large values of the local complex work per cycle magnitude, together with the values of the phase shift being close to $\phi_{\text{rotation}} = 270^\circ$, have resulted in regions of high local aerodynamic damping ratios on the suction side. On the contrary in case of the baseline rotor, the distribution of local phase shift values on the suction side cause regions of negative local aerodynamic damping.

9.5.4 1st Torsional Mode (Blades Vibrating at the Same Frequency)

In case where blade oscillation frequency is set to that of the baseline rotor for all of the different rotors of various blade count, the characteristics S-Curve and blade influence coefficients plots corresponding to the 1st torsional mode of blades are illustrated in figures 9.19 and 9.20.

Comparing the aerodynamic damping ratio plots as reported in Figure 9.19, for rotors of 13 and 21 blades with respect to the baseline rotor, it is observed that the S-Curves follow a similar trend with the maximum damping ratio corresponding to the inter-blade phase angle of ($\sigma = 0$). In case of the rotor with 25 blades though, the maximum damping ratio takes place at the nodal diameter 5 of forward traveling wave, while significant deviations in terms of aerodynamic damping ratios are present at nodal diameters of 6 to 10 of forward traveling wave compared to the baseline rotor.

Figure 9.19 also yields the fact that the value of minimum aerodynamic damping ratio for rotors of 13 and 25 blades correspond to the nodal diameters of 6 and 10 of backward traveling wave with deviations of -18.6% and 54.5% respectively compared to the baseline rotor. Meanwhile in case of the rotor with 21 blades, the value of minimum damping ratio is detected at a nodal diameter 7 of forward traveling wave and with deviation of 1.4% compared to the baseline rotor.

Regarding the blade influence coefficients plot in Figure 9.20, the deviations in value of influence coefficient of the central reference blade with respect to the baseline case, is -20.4% , -22.4% and -54.5% for rotors of 13, 21 and 25 blades respectively.

Figures 9.21 and 9.22, represent the local values of aerodynamic damping ratio, amplitude of the complex work per cycle and the phase shift between the complex force and complex displacement values, for the baseline rotor ($\sigma = 84.7$) and the rotor consisting of 25 blades ($\sigma = 100.8$) respectively. Comparing the two figures it is noted that when both of the blades are oscillating with a similar frequency, the distribution of phase shift values on both the suction and pressure sides of the blade follow a similar trend, although the magnitude of the local complex work per cycle remains substantially higher in case of the rotor with 25 blades compared to the baseline case.

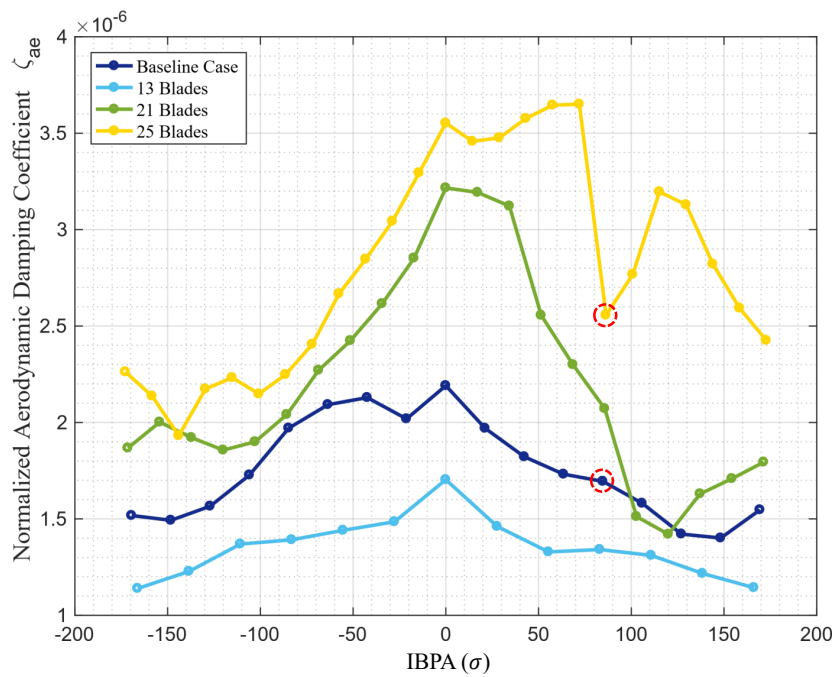


Fig. 9.19 – S-Curve for rotors with various blade count oscillating in same frequency

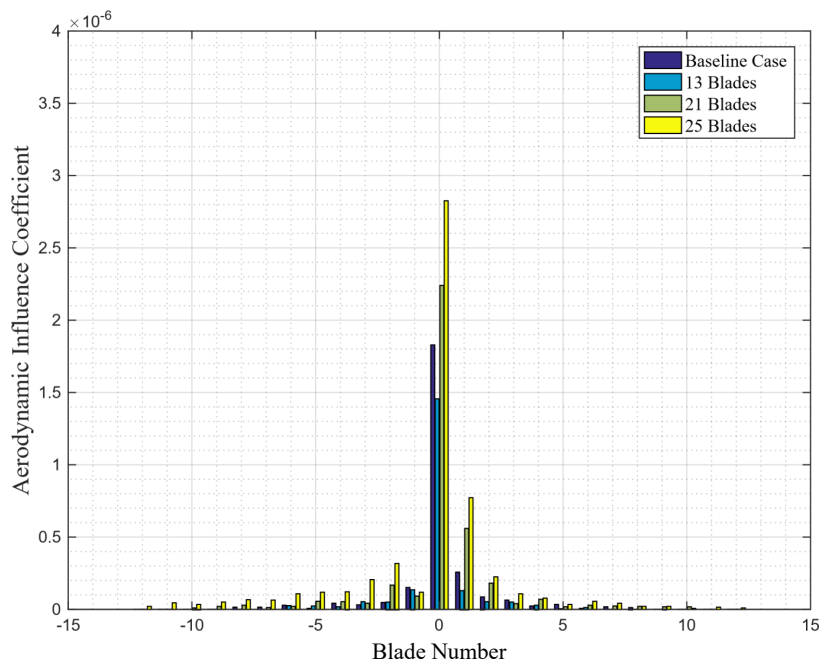


Fig. 9.20 – Blade influence coefficients for rotors with various blade count oscillating in same frequency

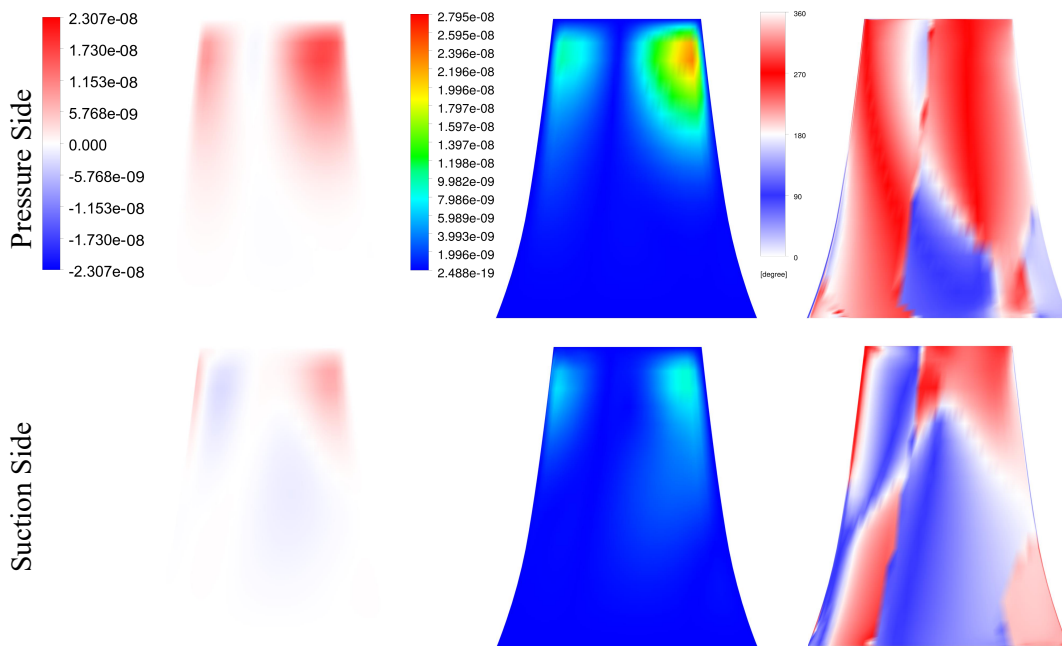


Fig. 9.21 – Local aerodynamic damping ratio (left), amplitude of the local complex work per cycle (center) and phase shift between the local complex force and complex displacement values (right) plotted on the suction and pressure side of baseline rotor blade (mode 2, $\sigma = 84.7$)

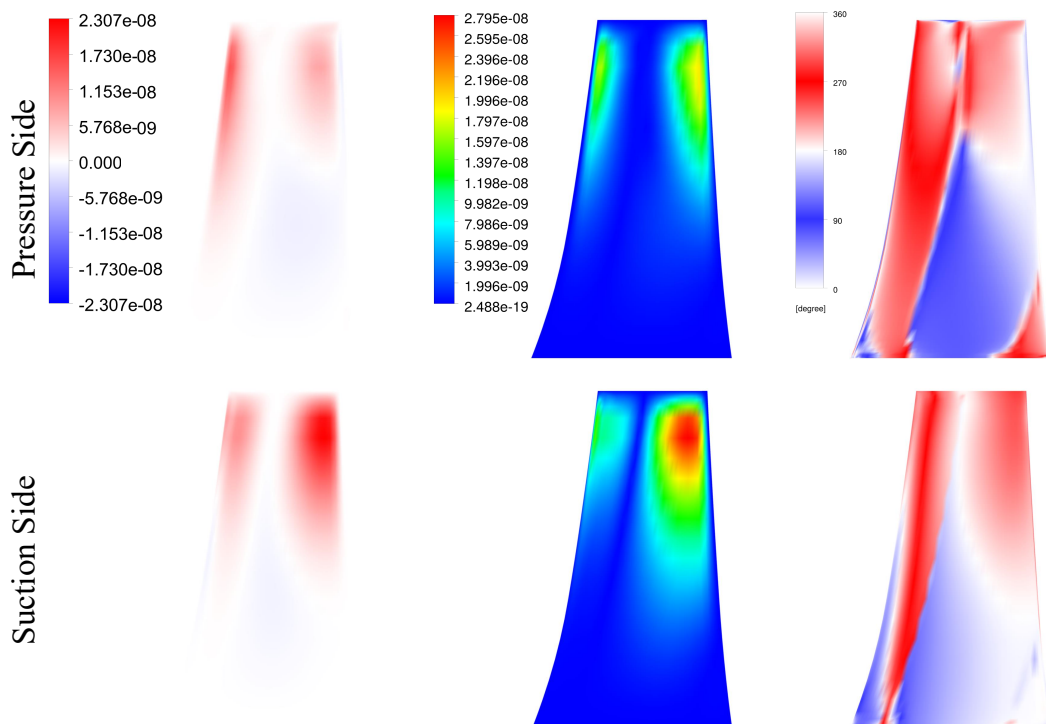


Fig. 9.22 – Local aerodynamic damping ratio (left), amplitude of the local complex work per cycle (center) and phase shift between the local complex force and complex displacement values (right) plotted on the suction and pressure side of the modified rotor with 25 blades (mode 2, $\sigma = 100.8$)

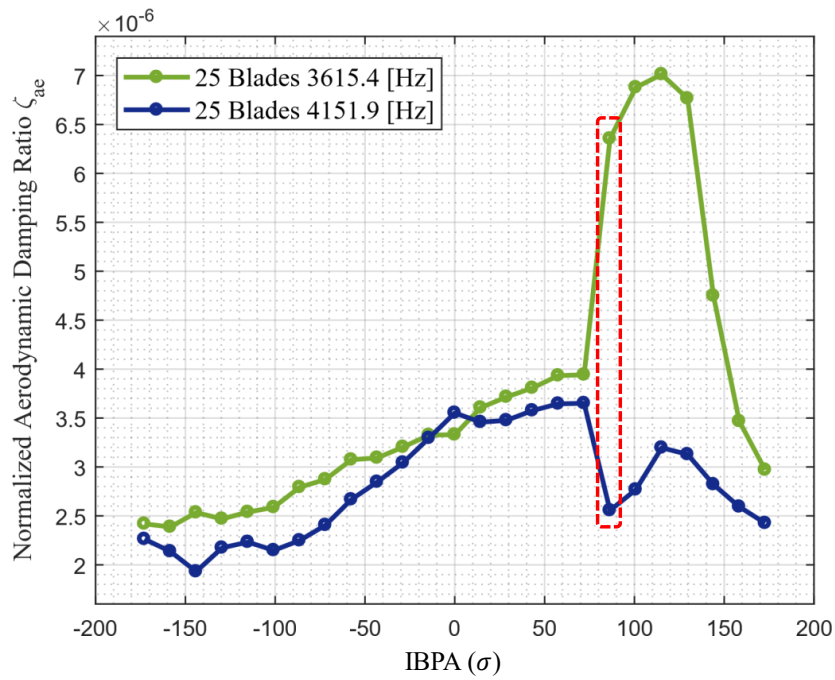


Fig. 9.23 – S-Curves of the rotor consisting of 25 blades compared at two different frequencies (mode 2, $\sigma = 100.8$)

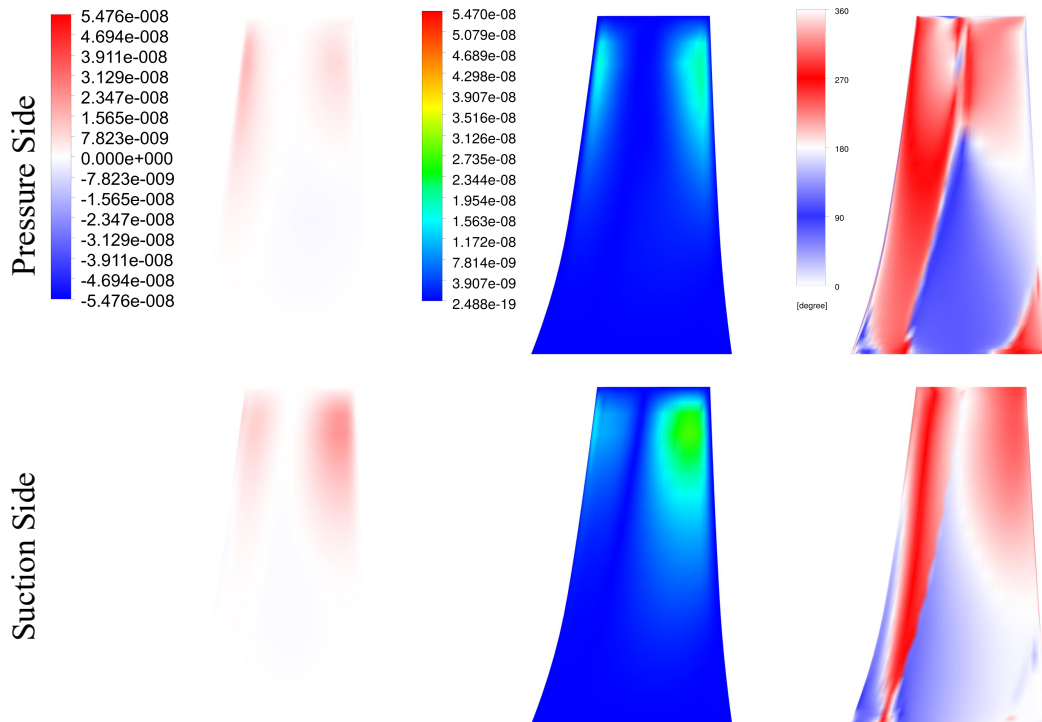


Fig. 9.24 – Local aerodynamic damping ratio (left), amplitude of the local complex work per cycle (center) and phase shift between the local complex force and complex displacement values (right) plotted on the suction and pressure side of the modified rotor with 25 blades (mode 2, $\sigma = 100.8$)

Figures 9.18 and 9.24 represent the local aerodynamic damping ratio, amplitude of the local complex work per cycle and phase shift between the local complex force and complex displacement values for the rotor consisting of 25 blades oscillating at the 1st torsional mode with two different frequencies, as it is marked on Figure 9.23. Comparing the two figures a substantial reduction in the magnitude and intensity of the local complex work per cycle can be detected as the oscillation frequency decreases. Referring to section 8.2, however such variations in the phase and amplitude of the local complex work per cycle and the resulting shape of the characteristics S-Curve can be attributed to the variations of the blade vibration frequency.

9.6 Conclusion

Referring to the results obtained in chapter 8, it can be perceived that, a reduction in the value of oscillation frequency results in an increase in the value of the reference blade influence coefficient and thus an increase both in the magnitude and intensity of the local complex work per cycle values. However though such an increase in the value and intensity of the local complex work per cycle values may result either in a stabilizing or destabilizing character of the flow depending on the distribution of the local phase shift between the complex force and complex displacement values which is itself largely influenced by variations of the oscillation frequency.

It is worth to restate that as it was illustrated in section 9.2, in the current case by increasing the blade count a reduction in the values of the eigen-frequencies of the 1st bending and torsional modes is detected. Meanwhile with the MAC indices remaining close to 1 for both of the mode shapes under investigation in all of the cases, it can be elucidated that the variations in the mode shapes are minimum.

Considering the case where the blades are oscillating at their 1st bending mode and with different frequencies, as it is demonstrated in a comparative manner for the baseline rotor and the rotor consisting of 21 blades at an inter-blade phase angle of $\sigma = 0$, the larger values of the aerodynamic damping ratio for the rotor of 21 blades can be attributed to the variations in value and distribution of the local phase shift between the complex force and complex displacement as well as the variations in the magnitude and intensity of the local complex work per cycle.

On the other hand when the blade oscillation frequency in all of the cases with variable blade count is set to eigen-frequency corresponding to the 1st bending mode of the baseline rotor, it is noted that the value and distribution of the phase shift between the local complex force and complex displacement follow a similar trend for all of the cases as it is demonstrated by comparing the baseline rotor and the rotor of 25 blades.

However though in this case with increasing blade count a substantial increase in the magnitude and intensity of the local complex work per cycle can still be detected which results in larger values of overall aerodynamic damping ratio for the rotors with larger blade count. Thus with the variations of the mode that pertain to a minimum extent, such an increase in the magnitude and intensity of the local complex work per cycle can

be attributed to the reduction of blade pitch for increasing blade count as the blades are more closely spaced.

Considering the 1st torsional mode shape similar conclusions can be drawn when the blades of different rotors of variable blade count are oscillating at different frequencies. As it is demonstrated in a comparative manner for the baseline rotor and the rotor of 25 blades at an inter-blade phase angle of $\sigma = 84.7$ and $\sigma = 100.8$ respectively. Also comparing the rotor consisting of 25 blades at an inter-blade phase angle of $\sigma = 100.8$, at two different frequencies it is observed that an increase in the magnitude and intensity of the local complex work per cycle as a result of reduction in the oscillation frequency, followed by variations in distribution and value of the local phase shift between the complex force and complex displacement, can result in significant changes in the value of the overall aerodynamic damping ratio.

Referring to section 9.5.1, it is also worth restating that phenomena such as the tip vortex of the neighbouring blades or flow separations can influence the values of the phase shift between the complex force and complex displacement as well.

10 Influence of Blade Loading Distribution on Aerodynamic Damping

The baseline rotor blade has been designed according to the “free vortex” law which results in a flow with a radial component of velocity equal to zero and an axial component which remains constant along spanwise direction. Characteristics of such a design criteria are the large flow deflections near the blade hub and smaller flow deflections near the blade tip region.

In an attempt to investigate the influence of variations of the blade trailing edge angle on the aerodynamic damping characteristics, multiple blades have been generated by modifying the baseline rotor design. In this regard, while the leading edge angle (β_1) is preserved, the trailing edge angle (β_2) has been altered in such a manner that the blade chord length remains unchanged.

It must be noted that, unlike the baseline design which pertains to a parabolic distribution of β_2 angle along the spanwise position, in case of the modified blades, the variations of β_2 angle follow a linear trend as it is illustrated in Figure 10.1.

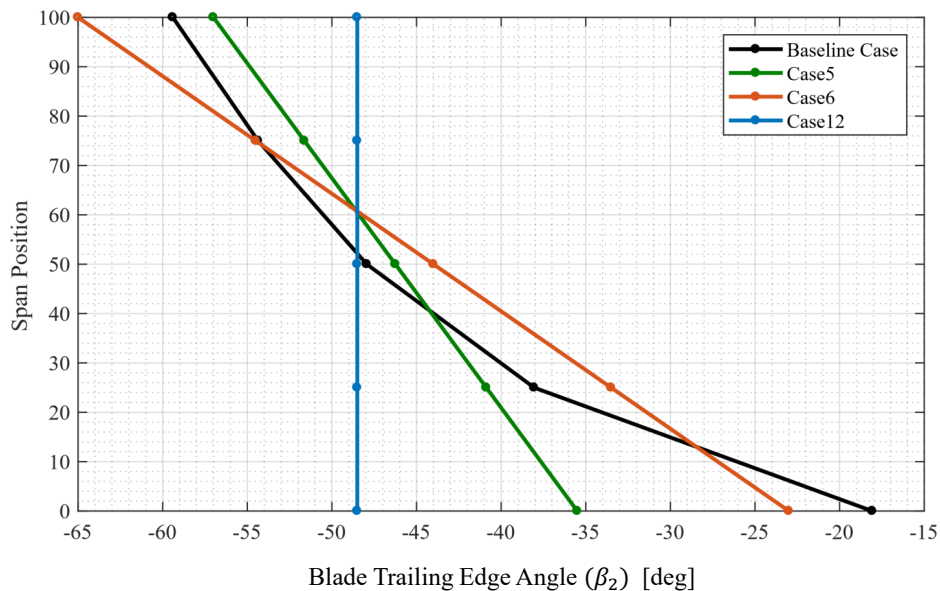


Fig. 10.1 – Variations of the (β_2) angle as a function of the spanwise position for different cases of modified geometries

As a result, 12 new cases have been generated which no longer conform to the free vortex law and yield different flow deflection both at the blade hub and tip regions compared to the baseline design. Table 10.1 reports the geometrical parameters of the selected modified blades.

Table 10.1 – Geometrical parameters for different cases with modified trailing edge angle

| Case Name | $\beta_{1,hub}$ [deg] | $\beta_{2,hub}$ [deg] | $\beta_{1,tip}$ [deg] | $\beta_{2,tip}$ [deg] | $\Delta\beta_{hub}$ | $\Delta\beta_{tip}$ |
|---------------|-----------------------|-----------------------|-----------------------|-----------------------|---------------------|---------------------|
| Baseline Case | -60.7 | -18 | -69.7 | -59.4 | 42.7 | 10.3 |
| Case 5 | -60.7 | -35.5 | -69.7 | -57 | 25.2 | 12.7 |
| Case 6 | -60.7 | -23 | -69.7 | -65 | 37.7 | 4.7 |
| Case 12 | -60.7 | -48.5 | -69.7 | -48.5 | 12.2 | 21.2 |

10.1 Steady State Analysis

Prior to conducting unsteady CFD analysis to determine the aerodynamic damping characteristics of the modified rotors, a steady state analysis is necessary for all of the modified cases. Thus by investigating the steady state performance it is possible to distinguish the cases in which the steady state aerodynamics is preserved.

Figure 10.2, represents the aerodynamic performance characteristics in terms of efficiency and compression ratio in a comparative manner for all of the investigated cases. It is observed that the cases 5, 6 and 12, which are also highlighted in Figure 10.1, guarantee steady state aerodynamics with minimal deviations with respect to the baseline rotor design.

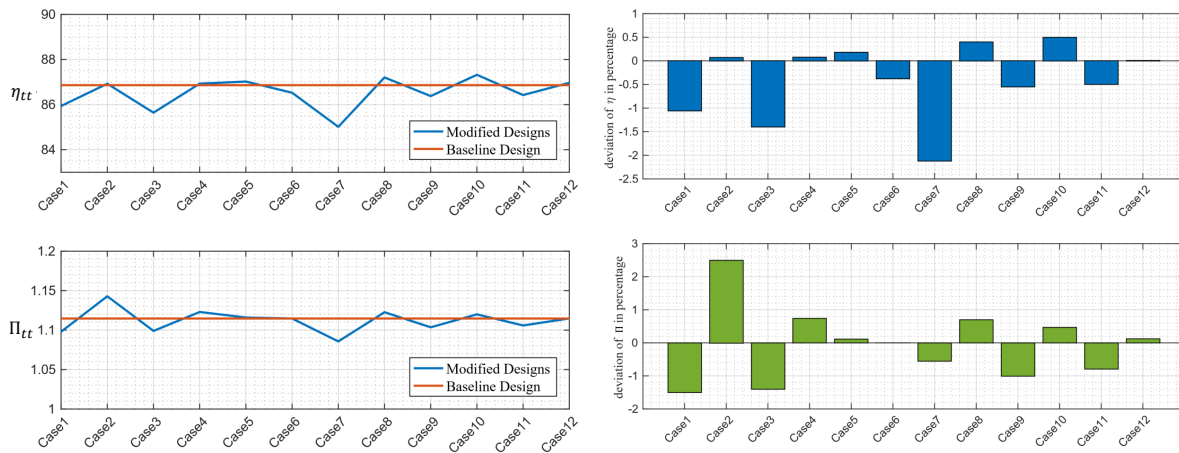
**Fig. 10.2** – Steady state aerodynamic performance of the investigated cases with variable β_2 angle

Figure 10.3, illustrates the blade loading plots for the investigated cases at different span positions. It is noted that an increase in the flow deflection results in an increases in blade loadings both at the hub region and blade tip region. In this regard, it can be observed that the blades of case 12 and case 6 yield the highest and lowest blade loadings in the tip region respectively.

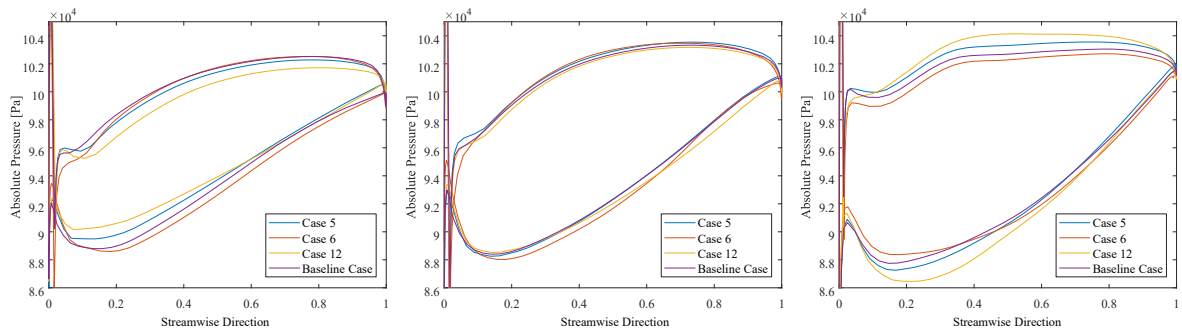


Fig. 10.3 – Blade loading plots at 0.1 span positions (left), 0.5 span position (center) and 0.9 span position (right)

10.2 Modal Analysis

In order to obtain oscillation frequencies and mode shapes which will be mapped on the CFD mesh within the unsteady simulations setup, a modal analysis has been performed for each case through finite element analysis as described in section 6. A graphical representation of the 1st bending and 1st torsional mode shapes of each case is represented in Figure 10.4 where as table 10.2 reports the oscillation frequencies.

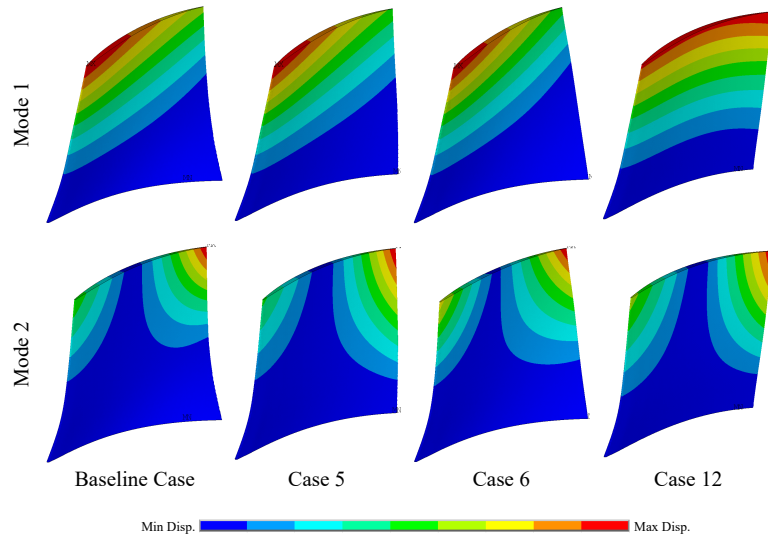


Fig. 10.4 – Graphical representation of the 1st bending and 1st torsional mode shapes of the investigated cases with variable β_2 angle

Table 10.2 – Frequencies of the first two mode shapes of investigated cases with variable β_2 angle

| Case Name | Baseline Case | Case 5 | Case 6 | Case 12 |
|-------------------------|---------------|---------|---------|---------|
| Frequency [Hz] - Mode 1 | 1654.36 | 1702.29 | 1733.25 | 1599.67 |
| Frequency [Hz] - Mode 2 | 4151.91 | 3519.94 | 4654.72 | 2722.89 |

10.3 Unsteady CFD Analysis

In an attempt to investigate the influence of variations in the blade trailing edge β_2 on the aerodynamic damping ratio, an unsteady CFD analysis is required. Thus transient CFD simulations have been performed for the three selected case through the influence coefficients method approach for the 1st bending and 1st torsional mode shapes.

Similar to the case of variable blade counts, also in this case with the aim of gaining a distinguished overview on the influence of oscillation frequency and mode shape, two series of simulations are performed. For the first set of simulations, the eigen-frequencies computed through the modal analysis for each individual case are used, where as in the second set of the simulations, all the modified geometries oscillate with the eigen-frequency of the baseline rotor blade.

The computational domain which includes the full rotor geometry for each case with 17 passages without the need for applying periodic boundaries, consists of approximately 11,400,000 elements. With the boundary conditions and solver control being defined according to the CFD setup described in section 7.2, the convergence is reached after approximately 40 periods of run for each case. Thereafter each case has been subjected to the post-processing procedure described in section 5.3.1, in order to obtain the characteristics S-Curves and to extract the blade influence coefficients.

10.4 Results

10.4.1 1st Bending Mode (Blades Vibrating at Different Frequencies)

Figure 10.5 illustrates the obtained characteristic S-Curves corresponding to different rotors with modified blade trailing edge angles, vibrating with the 1st bending mode shape at frequencies derived through modal analysis for each individual case. It can be observed that for all the cases, the value of minimum aerodynamic damping coefficient conforms to an inter-blade phase angle of $\sigma = 0$, with a deviation of 16.4%, 28.8% and 21.5% for case 5, case 6 and case 12 respectively, compared to the baseline case.

Considering the blade influence coefficients as plotted in Figure 10.6, it is noted that, the influence coefficient of the central reference blade in case 5 and case 6, is higher by 2.7% and 0.75% respectively compared to the baseline design, where as this value is lower by -8.8% for case 12.

Figures 10.7 and 10.8, represent the local values of aerodynamic damping ratio, amplitude of the complex work per cycle and the phase shift between the complex force and complex displacement values, on both suction and pressure sides of blade surface for the baseline rotor and the rotor of case 6 respectively. Considering the plots which show the values of phase shift (ϕ_{rotation}) for an inter-blade phase angle of $\sigma = 0$, on the pressure side of the rotor of case 6 a different distribution of ϕ_{rotation} compared to the baseline rotor is detected which results in larger regions of positive local aerodynamic damping values. On the suction side though, a similar trend is detected for both of the cases.

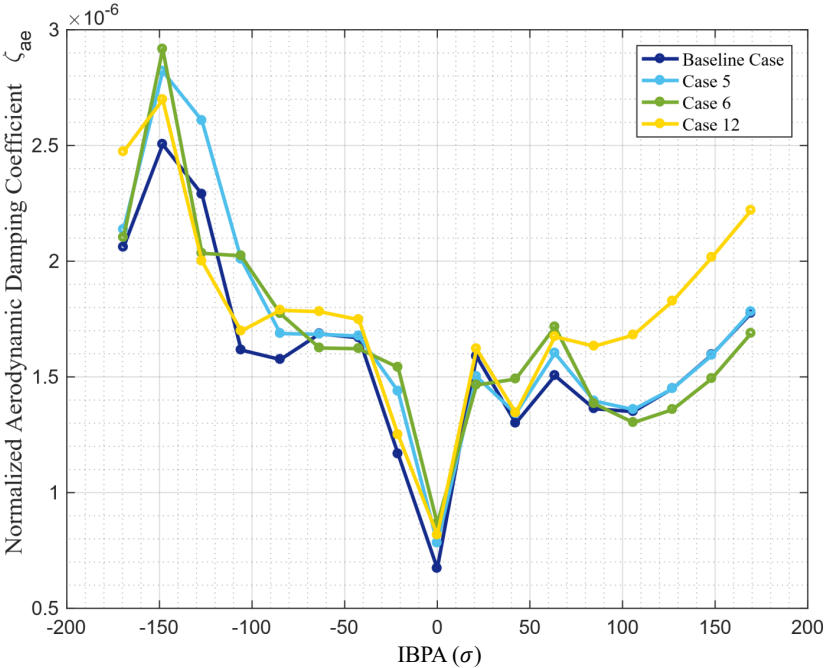


Fig. 10.5 – S-Curve for rotors with various trailing edge angle oscillating in different frequencies

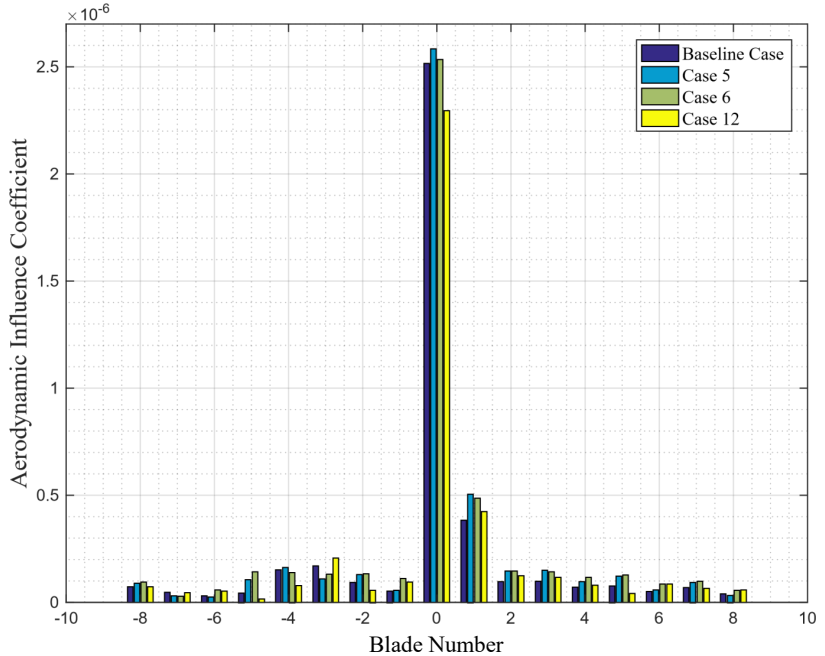


Fig. 10.6 – Blade influence coefficients for rotors with various trailing edge angle oscillating in different frequencies

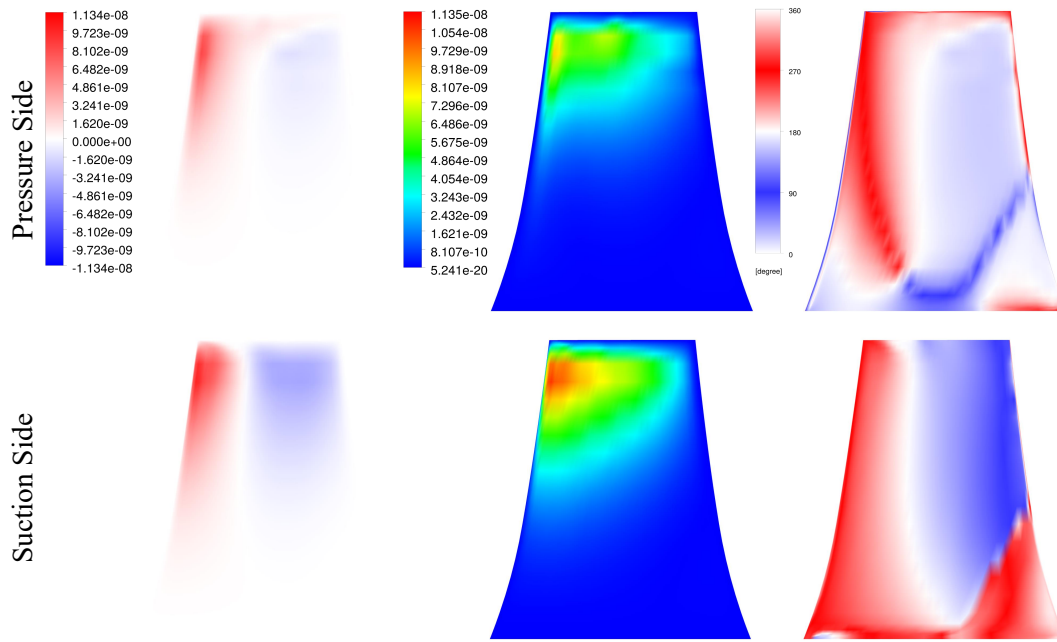


Fig. 10.7 – Local aerodynamic damping ratio (left), amplitude of the local complex work per cycle (center) and phase shift between the local complex force and complex displacement values (right) plotted on the suction and pressure side of baseline rotor blade (mode 1, $\sigma = 0$)

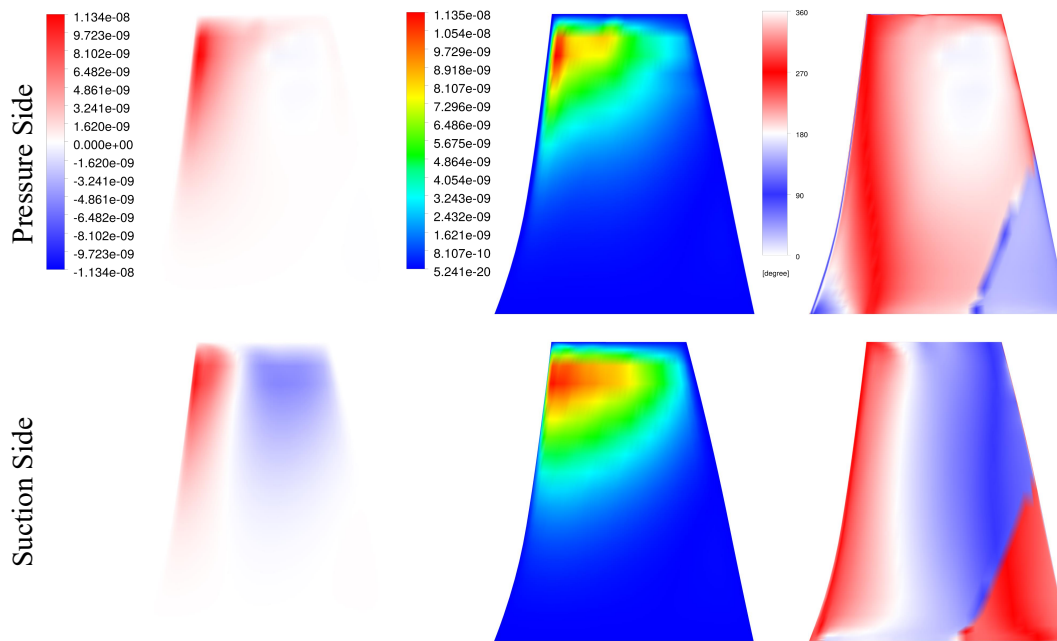


Fig. 10.8 – Local aerodynamic damping ratio (left), amplitude of the local complex work per cycle (center) and phase shift between the local complex force and complex displacement values (right) plotted on the suction and pressure side of the modified rotor of case 6 (mode 1, $\sigma = 0$)

10.4.2 1st Bending Mode (Blades Vibrating at the Same Frequency)

Figure 10.9 represents the characteristic S-Curves in case where different rotors with modified blade trailing edge angles oscillate with the 1st bending mode shape at a frequency which is set to that of the baseline rotor. It is observed that while the minimum damping value corresponds to an inter-blade phase angle of $\sigma = 0$ for all of the cases, the deviations in this value for case 5 and case 6 compared to the baseline case is limited to -2.5% and -5.3% whereas in case 12 minimum damping ratio pertains to a value which is 38.8% higher with respect to the baseline case.

Considering Figure 10.10 which depicts the blade influence coefficients, the influence coefficient of the central reference blade in case 5, case 6 and case 12 incorporates a deviation of 2.6%, 2.5% and -2.9% respectively compared to the baseline rotor.

Referring to section 10.2, it is worth noting that, the rotor blade of case 6 has the highest eigen-frequency corresponding to the 1st eigen-mode compared to the other cases. Regarding the rotor blade of case 12 however, it can be elucidated that albeit having the lowest oscillation frequency compared to the other cases, the mode shape conforms to a pure bending mode about the blade camber line (flap mode) rather than a corner mode as the other cases.

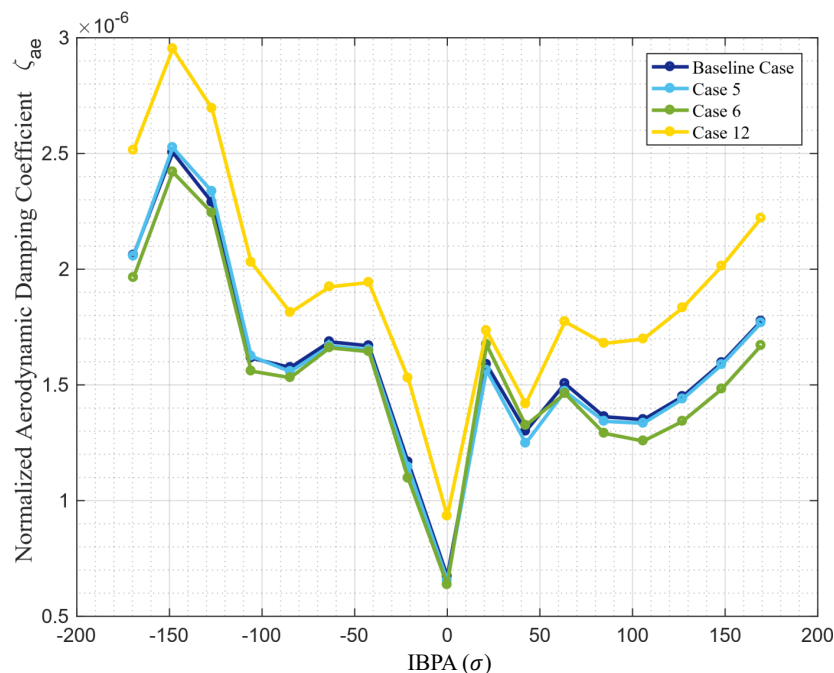


Fig. 10.9 – S-Curve for rotors with various trailing edge angle oscillating in same frequency

Figures 10.11 and 10.12, represent the local values of aerodynamic damping ratio, amplitude of the complex work per cycle and the phase shift between the complex force and complex displacement values, on both suction and pressure sides of blade surface for the baseline rotor and the rotor of case 12 respectively.

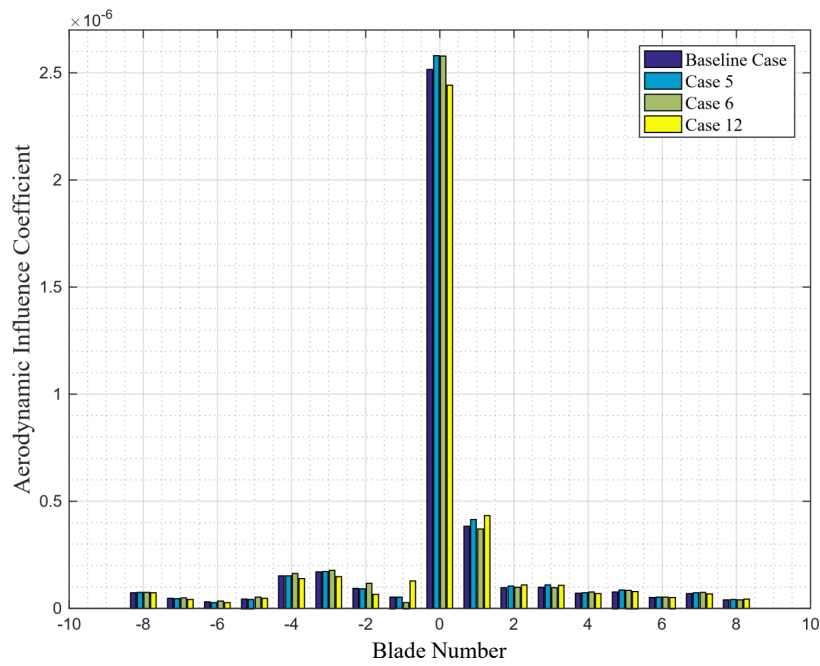


Fig. 10.10 – Blade influence coefficients for rotors with various trailing edge angle oscillating in same frequency

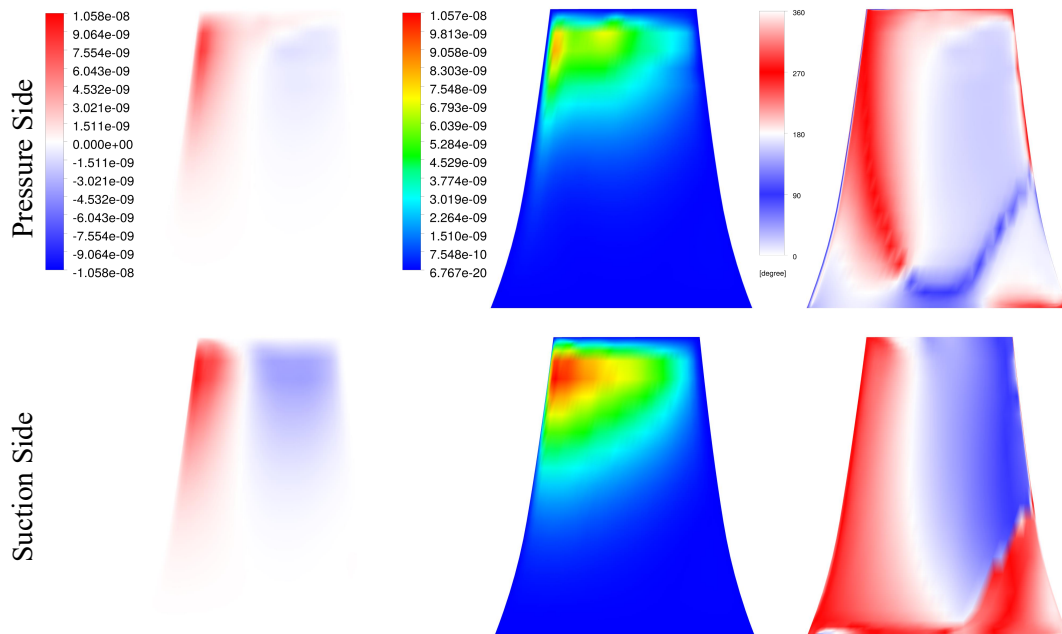


Fig. 10.11 – Local aerodynamic damping ratio (left), amplitude of the local complex work per cycle (center) and phase shift between the local complex force and complex displacement values (right) plotted on the suction and pressure side of baseline rotor blade (mode 1, $\sigma = 0$)

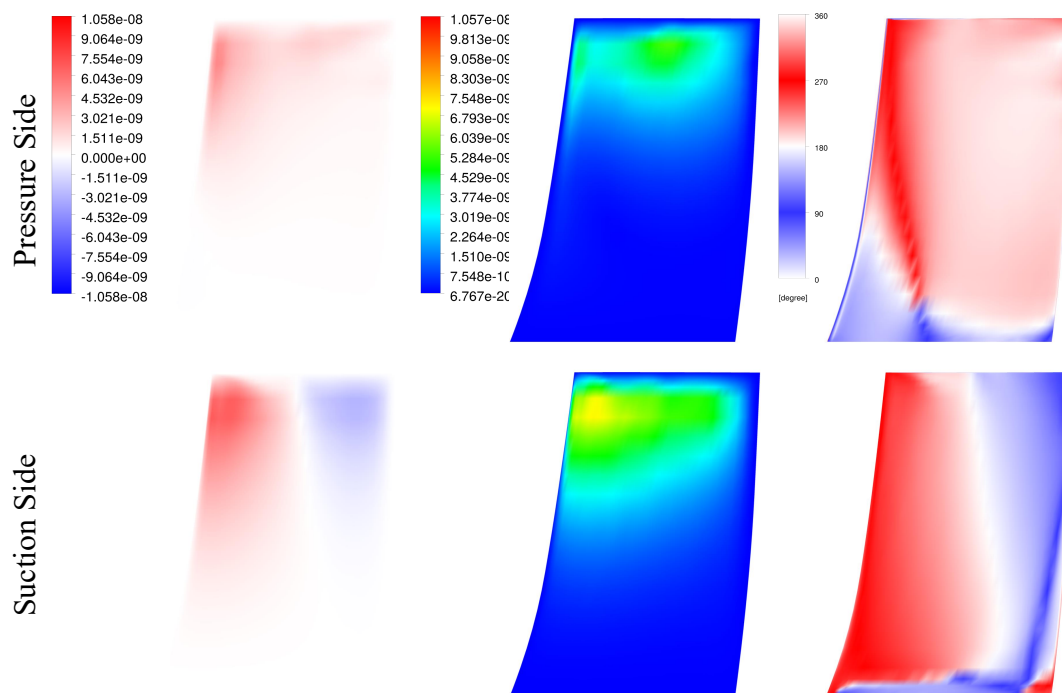


Fig. 10.12 – Local aerodynamic damping ratio (left), amplitude of the local complex work per cycle (center) and phase shift between the local complex force and complex displacement values (right) plotted on the suction and pressure side of the modified rotor of case 12 (mode 1, $\sigma = 0$)

Comparing the two figures, it is observed that although both of blades are oscillating with a similar frequency, differences in the distribution of the local phase shift values (ϕ_{rotation}) can be detected which can be attributed to differences in the corresponding mode shapes.

It is worth noting that, comparing similar plots for rotors of case 5 and case 6 with the baseline rotor, a similar trend can be seen in terms of local phase shift distribution on blade surfaces.

10.4.3 1st Torsional Mode (Blades Vibrating at Different Frequencies)

Figure 10.13 illustrates the obtained characteristic S-Curves corresponding to different rotors with modified blade trailing edge angles, vibrating with the 1st torsional mode shape at frequencies derived through modal analysis for each individual case. It is observed that for rotors of case 5 and case 6, the minimum damping ratio conforms to nodal diameters of 6 and 7 of forward traveling wave respectively, with values that have deviations of -18.2% and -19.8% compared to the baseline case. For the rotor of case 12 though, the minimum damping ratio corresponds to a nodal diameter of 6 of backward traveling wave with a value which is 35.6% higher than the baseline rotor.

It is also noted that the value of maximum damping ratio for rotors of case 5, case 6 and case 12, pertains to nodal diameters of 1, 3 and 4 of forward traveling wave, with values that are by 27.4% , -13.5% and 134% deviated from the baseline rotor design.

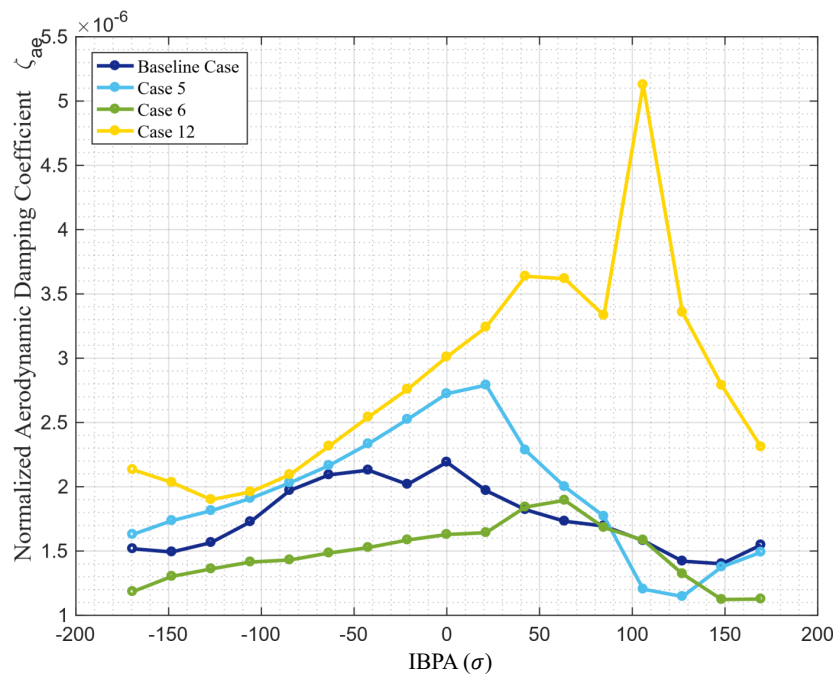


Fig. 10.13 – S-Curve for rotors with various trailing edge angle oscillating in different frequencies

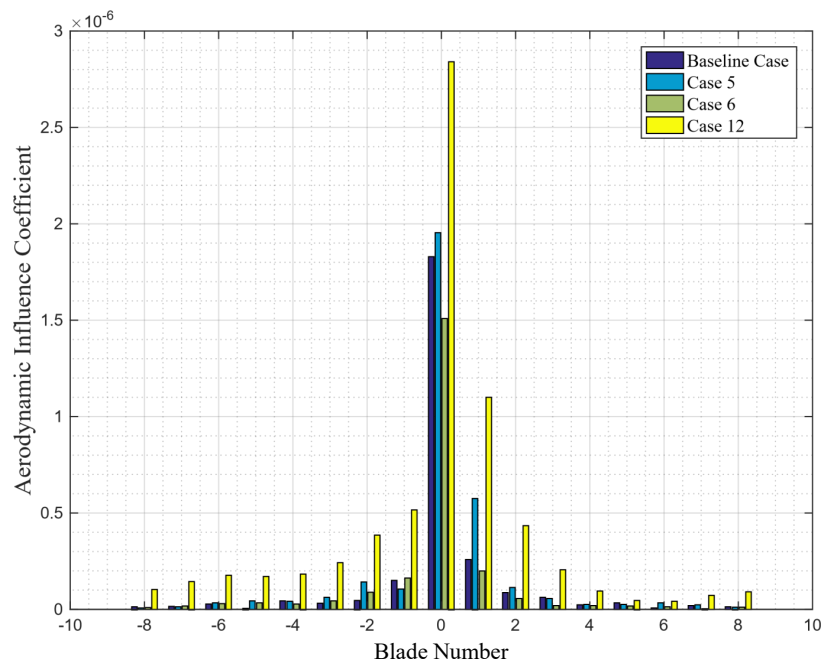


Fig. 10.14 – Blade influence coefficients for rotors with various trailing edge angle oscillating in different frequencies

Considering the blade influence coefficients as plotted in Figure 10.14, it is noted that, the influence coefficient of the central reference blade in case 5 and case 12, is higher by 6.8% and 55.3% respectively compared to the baseline design, where as this value is lower by -17.6% for case 6.

Referring to section 10.2, it is worth noting that, the rotor blades of case 6 and case 12 have the highest and lowest eigen-frequencies corresponding to the 2nd eigen-mode compared to the other cases.

Figures 10.15 and 10.16, represent the local values of aerodynamic damping ratio, amplitude of the complex work per cycle and the phase shift between the complex force and complex displacement values, on both suction and pressure sides of blade surface for the baseline rotor and the rotor of case 5 respectively.

Referring to Figure 10.16, it is elucidated that, on the suction side of the blade of rotor of case 5, although the magnitude of local complex work per cycle retains lower values compared to the baseline case, with regions of phase shift (ϕ_{rotation}) which conform to a value of 270° , the values of local aerodynamic damping ratio are mainly positive on the suction side.

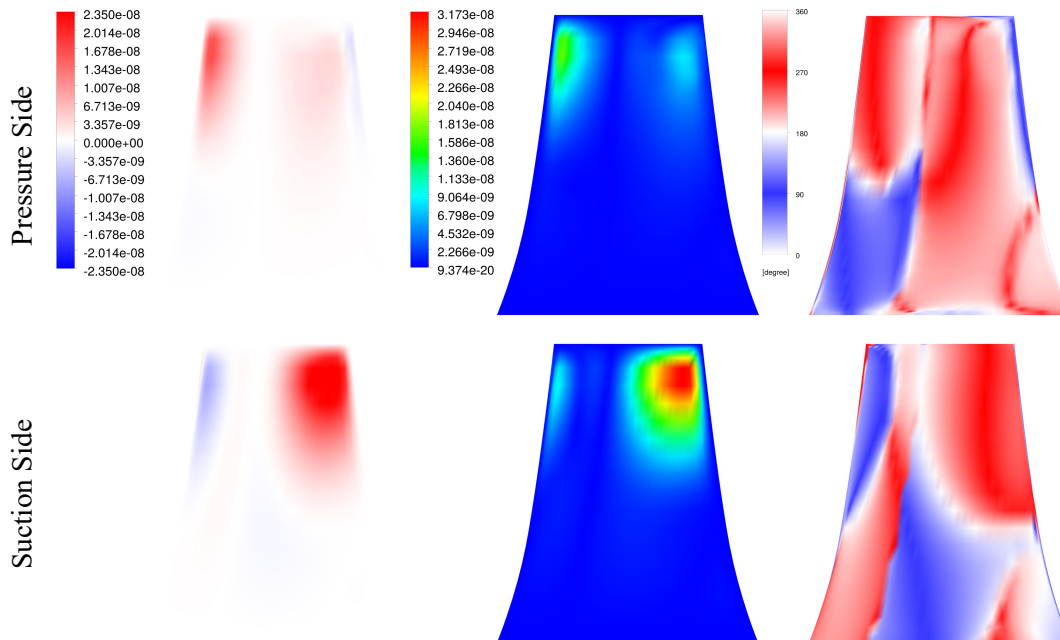


Fig. 10.15 – Local aerodynamic damping ratio (left), amplitude of the local complex work per cycle (center) and phase shift between the local complex force and complex displacement values (right) plotted on the suction and pressure side of baseline rotor blade (mode 2, $\sigma = 0$)

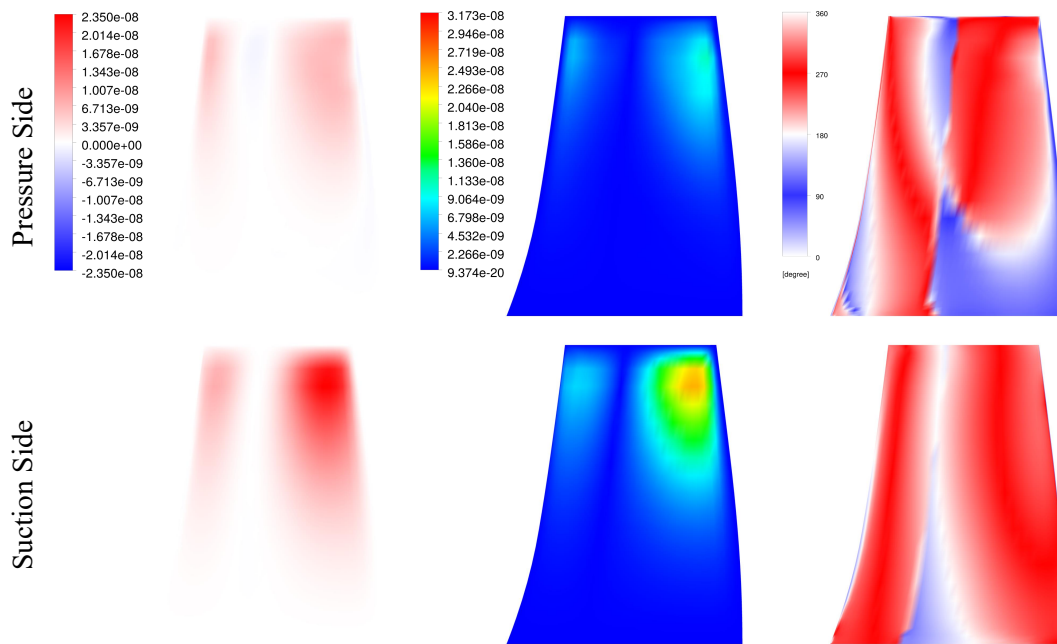


Fig. 10.16 – Local aerodynamic damping ratio (left), amplitude of the local complex work per cycle (center) and phase shift between the local complex force and complex displacement values (right) plotted on the suction and pressure side of the modified rotor of case 5 (mode 2, $\sigma = 0$)

10.4.4 1st Torsional Mode (Blades Vibrating at the Same Frequency)

Figure 10.17 represents the characteristic S-Curves in case where different rotors with modified blade trailing edge angles oscillate with the 1st torsional mode shape at a frequency which is set to that of the baseline rotor. It is observed that for rotors of case 5, case 6 and case 12 the minimum aerodynamic damping ratio conforms to a nodal diameter of 6 of forward traveling wave which have deviations equal to -11.8% , -9.9% and -22.5% respectively compared to the baseline case. It is also noted that for all of the cases the value of maximum aerodynamic damping ratio corresponds to an inter-blade phase angle of $\sigma = 0$. The deviations in this value for case 5, case 6 and case 12 compared to the baseline case is limited to -1.3% , -4.8% and -9.7% respectively.

Considering Figure 10.18 which illustrates the blade influence coefficients, the influence coefficient of the central reference blade in case 5, case 6 and case 12 incorporates a deviation of -4.8% , -7.1% and -11.5% respectively compared to the baseline rotor.

Figures 10.19 and 10.20, represent the local values of aerodynamic damping ratio, amplitude of the complex work per cycle and the phase shift between the complex force and complex displacement values, on both suction and pressure sides of blade surface for the baseline rotor and the rotor of case 12 respectively. Comparing the two figures, a similar trend is detected in terms of local phase shift value ϕ_{rotation} distribution on both the pressure side and suction side of the blades. Regarding the amplitude of the local complex work per cycle however, the baseline case yields larger values compare to the rotor of case 12.

Meanwhile it is worth noting that, if similar plots are compared for the baseline rotor and the rotor of case 5, similarities both in terms of phase shift value distribution and local complex work per cycle magnitudes are observed which is in consistency with the S-Curve and blade influence coefficient plots.

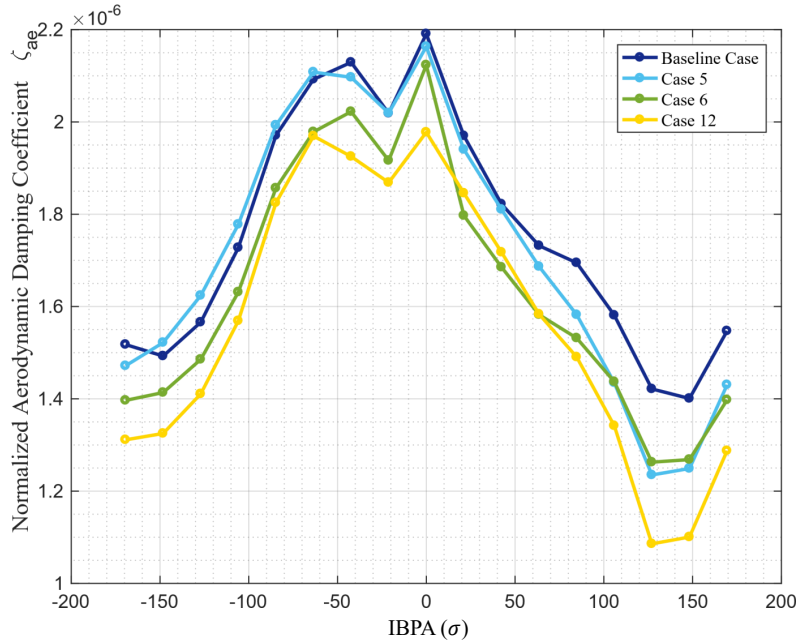


Fig. 10.17 – S-Curve for rotors with various trailing edge angle oscillating in same frequency

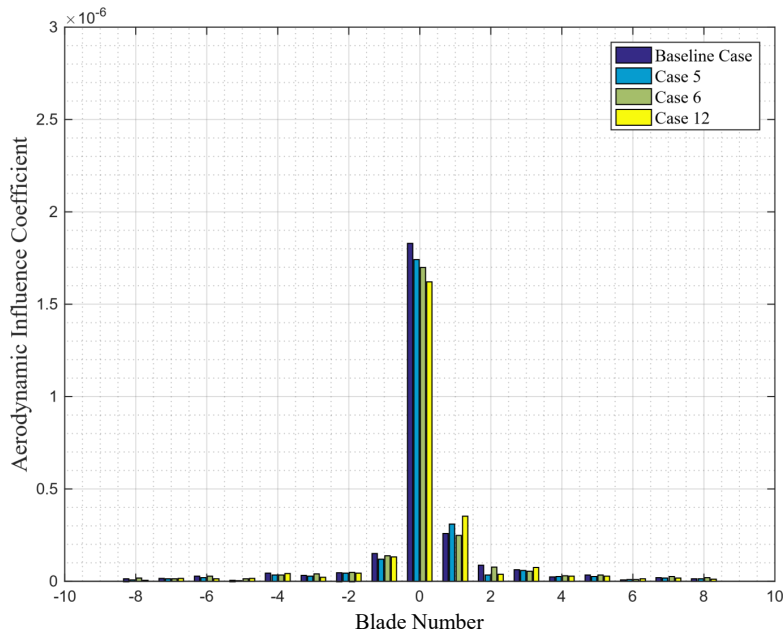


Fig. 10.18 – Blade influence coefficients for rotors with various trailing edge angle oscillating in same frequency

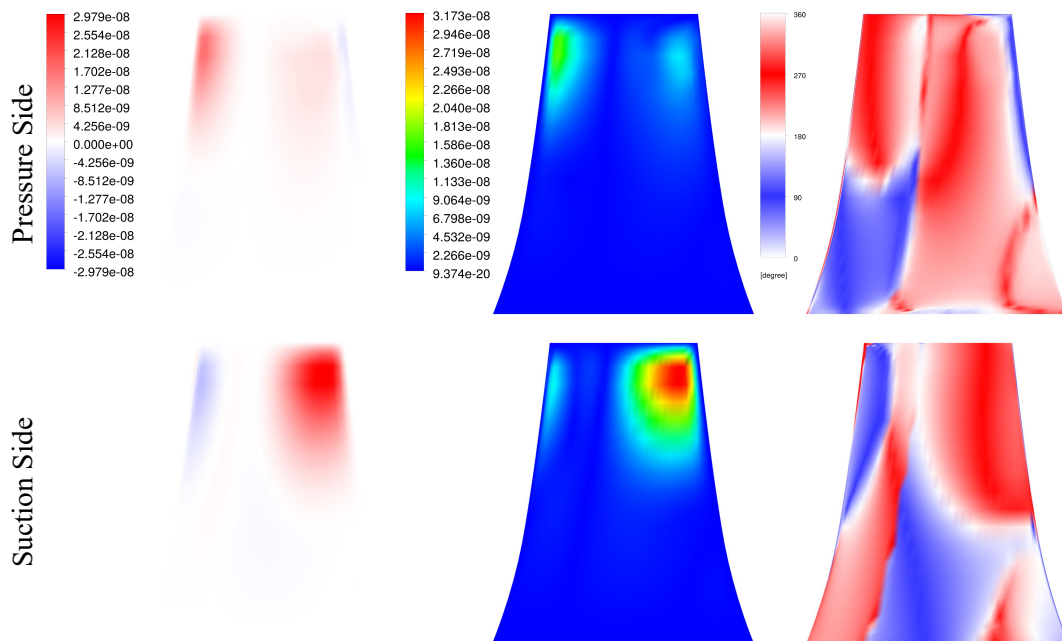


Fig. 10.19 – Local aerodynamic damping ratio (left), amplitude of the local complex work per cycle (center) and phase shift between the local complex force and complex displacement values (right) plotted on the suction and pressure side of baseline rotor blade (mode 2, $\sigma = 0$)

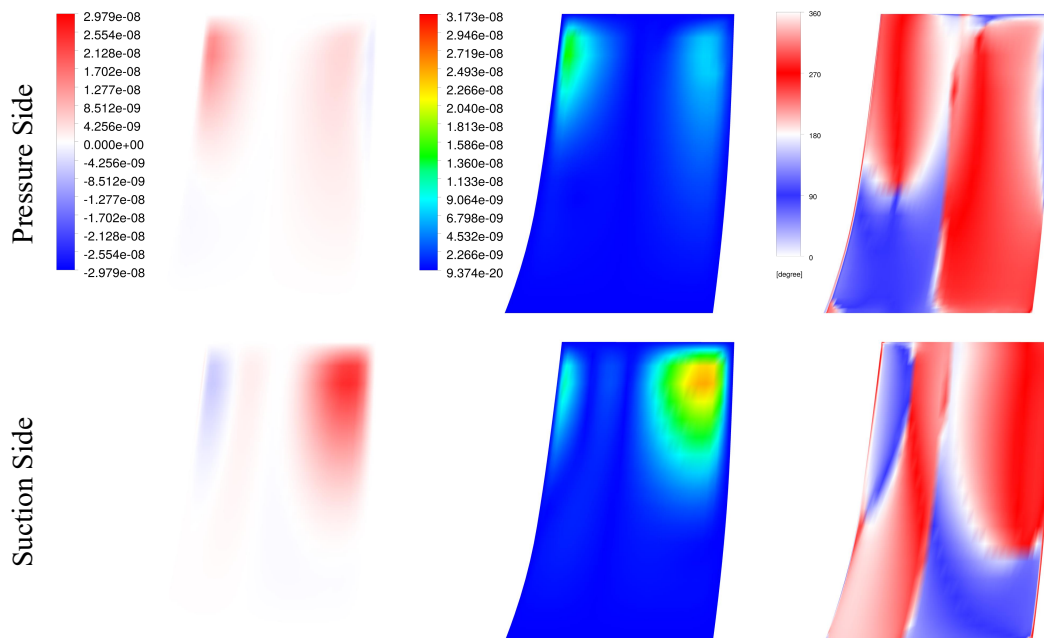


Fig. 10.20 – Local aerodynamic damping ratio (left), amplitude of the local complex work per cycle (center) and phase shift between the local complex force and complex displacement values (right) plotted on the suction and pressure side of the modified rotor of case 12 (mode 2, $\sigma = 0$)

10.5 Conclusion

Referring to the case in which the blades of different rotors with variable trailing edge angle are oscillating at their 1st bending mode as it is demonstrated in a comparative manner for the baseline rotor and the rotor of case 6, and considering the fact that the eigen-frequency of the baseline rotor blade has a lower value for the 1st bending mode compared to the rotor of case 6, in contrast to the results obtained in chapter 8, the magnitude and intensity of the local complex work per cycle in the baseline rotor blade is lower compared to the rotor of case 6. A similar trend is also detected when both of the blades are oscillating with the same frequency. Thus as the mode shapes are similar for both of the blades, such a phenomenon can be attributed to the variations of the blade loadings of the two rotors.

In a further attempt the baseline rotor has been compared to the rotor of case 12 when both of the blades are oscillating at their 1st bending mode but with the same frequency. In this case in addition to the variations of the blade loadings, a significant change in the mode shape can be detected. It is worth noting that in a similar manner when the baseline rotor is compared to the rotors of case 5 and case 6 which pertain to similar mode shapes, it is observed that the distribution and values of the phase shift between the complex force and complex displacement conform to a similar pattern for the cases mentioned. On the contrary the rotor of case 12 follows a different pattern as it is illustrated in Figure 10.12. As a result it can be elucidated that comparing the baseline rotor with the rotor of case 12 when oscillating at their 1st bending mode and with the same frequency, the variations in terms of the local complex work per cycle and the phase shift between the complex force and complex displacement values can be attributed to the variations in the blade loading and oscillation mode shape respectively.

Referring to the case where the blades of different rotors are oscillating at their 1st torsional mode shapes with different frequencies, the baseline rotor is compared to the rotor of case 5 which has an eigen-frequency with a lower value compared to the baseline rotor at an inter-blade phase angle of $\sigma = 0$. In contrast to the results obtained in chapter 8, it is observed the magnitude and intensity of the local complex work per cycle is lower for the rotor of case 5 compared to the baseline case. However though considering the value and distribution of the local phase shift between the complex force and complex displacement, for the rotor of case 5, the overall aerodynamic damping ratio yields a higher value.

Considering the case in which the the blades of different rotors are oscillating at their 1st torsional mode shapes but with the same frequency, the baseline rotor has been compared with the rotor of case 12. In this regard, with the mode shapes and the distribution of the local phase shift between the complex force and complex displacement values which follow a similar pattern or both of the cases, the variations in the magnitude and intensity of the local complex work per cycle values, can be attributed to the variations in the blade loadings of the two rotors.

11 Conclusion and Future Work

The baseline rotor design has been subjected to unsteady CFD simulations using the influence coefficients method with the central reference blade oscillating at its 1st bending and torsional mode shapes with different frequencies. Tracing the characteristics S-Curves, blade influence coefficients, local values of aerodynamic damping ratio, amplitude of the local complex work per cycle values and the difference in phase between the nodal complex work and complex displacement values, it is perceived that as the mode shape and operating condition is preserved in all of the cases, an increase in the oscillation frequency results in a reduction in the magnitude and intensity of the local complex work per cycle values for both of the mode shapes under investigation. Variations in frequency also influence the value and distribution of the phase shift between the local complex work and complex displacement and thus directly affect the overall aerodynamic damping ratio.

With the aim of investigating the influence of blade count on the aerodynamic damping ratio, the baseline rotor design has been scaled to generate different rotors of variable blade count with minimum changes in the blade loading and thus the steady-state aerodynamic performance of the rotor. Following a modal analysis for each case, a reduction in the eigen-frequencies corresponding to the 1st bending and torsional mode shapes has been detected for increasing blade count, with the variations in the mode shape being of negligible order. Unsteady CFD analyses has been performed for each of the mode shapes under investigation with the corresponding eigen-frequencies. Furthermore with the aim of obtaining a distinguished insight into the influence of frequency and blade pith values, a second set of unsteady CFD simulations have been performed with the oscillation frequency being set to the eigen-frequency of the baseline rotor blade in all of the cases.

Comparing the obtained results, it has been observed that with increasing blade count which is followed by a reduction of the oscillation frequency, the magnitude and intensity of the local complex work per cycle values follow an increasing trend for both of the mode shapes under investigation, while the difference in phase between the local complex force and complex displacement values is largely influenced by the oscillation frequency at every nodal diameter. Meanwhile comparing the results of the second set of simulations with the oscillation frequency being the same for all of the cases, a similar increasing trend in terms of the magnitude of the local complex work per cycle is detected. As the distribution and value of the phase shift between the local complex force and complex displacement follows a similar trend in this case, such an increase in the amplitude of the local complex work per cycle values can be attributed to the reduction of the blade pith as the blade count increases.

In a further attempt to investigate the influence of the blade loadings on the aerodynamic damping ratio, the trailing edge angle of the baseline rotor blade profile which

has been designed according to the free-vortex law, has been modified with the aim of generating alternative blade designs. Following an iterative procedure, three cases which conform to similar steady-state aerodynamic performance of the baseline rotor, have been selected for the subsequent unsteady CFD analysis. Referring to the obtained results for the case in which the blades oscillate at their 1st bending and torsional mode shapes with the corresponding eigen-frequencies, it is noted that in contrast to the results obtained in chapter 8, a reduction in the oscillation frequency is not followed by an increasing trend in terms of local complex work per cycle magnitude and intensity. On the other hand tracing the results corresponding to the case in which the blades of different rotors oscillate with the same eigen-frequency of the baseline rotor at the 1st bending and torsional mode shapes, it can be elucidated that the variations in terms of the local complex work per cycle and the phase shift between the complex force and complex displacement values can be attributed to the variations in the blade loading and oscillation mode shape respectively.

Within the present work, the “traveling wave mode approach” and the “influence coefficients method” have been incorporated for the 1st bending and 1st torsional blade dominated mode shapes that are independent of the nodal diameters, in an attempt to establish possible trends correlating the geometrical parameters and the aerodynamic damping ratio.

A future investigation shall include higher mode shapes as well as real mode shapes corresponding to every nodal diameter of forward and backward traveling waves. Also unsteady CFD analysis using “Fourier Transformation Method” for particular nodal diameters can provide a detailed insight into the variations of the flow field between different cases. Regarding the influence of the oscillation frequency on the aerodynamic damping ratio, it is suggested to perform unsteady CFD simulations for a wider range of frequencies for the baseline rotor. The current work has been focused on the design working point of the compressor blisk under investigation, while a similar study should be performed for the off-design operating conditions including transonic flow fields.

Bibliography

- [1] ANSYS: ANSYS CFX R18.1 Theory Guide, 2017
- [2] ANSYS: ANSYS Mechanical APDL Theory Reference, 2017
- [3] Asinari, P.; Chiavazzo, E.: *An Introduction to Multiscale Modeling with Applications*, Esculapio, ISBN 9788874885879, 2013
- [4] Bisplinghoff, R.; Ashley, H.; Halfman, R.: *Aeroelasticity in Axial-Flow Turbomachines*, Dover Publications, ISBN 9780486132433, 1999
- [5] BÖHLER: BÖHLER EDELSTAHL GMBH & Co KG N700 (17-4 PH) Data Sheet, www.bucorp.com/media/bohler-N700.pdf, 2010
- [6] Carta, F. O.: *Coupled Blade-Disk-Shroud Flutter Instabilities in Turbojet Engine Rotors*, *Journal of Engineering in Power*, Vol. 89, pp. 419–426, 1967
- [7] Cecrdle, J.: *Whirl Flutter of Turboprop Aircraft Structures*, 1st edn., Elsevier Science, ISBN 9781782421863, 2015
- [8] Crawley, E.: *Aeroelastic Formulation for Tuned and Mistuned Rotors*, *AGARD Manual on Aeroelasticity in Axial-Flow Turbomachines*, Vol. 2, Structural Dynamics and Aeroelasticity, Chapter 19, AGARD-AG-298, 1988
- [9] Dowell, E. H.: *A Modern Course in Aeroelasticity: Fifth Revised and Enlarged Edition*, 5th edn., Springer, ISBN 9783319094533, 2014
- [10] Franson, T. H.: *Aeroelasticity*, Book 1, 2013
- [11] Fung, Y. C.: *An Introduction to the Theory of Aeroelasticity*, Dover Publications, ISBN 9780486495057, 2002
- [12] Genta, G.: *Vibration Dynamics and Control*, Springer, ISBN 9780387795805, 2008
- [13] Kielb, J. J. Abhari R. S.: *Experimental Study of Aerodynamic and Structural Damping in a Full-Scale Rotating Turbine*, *ASME. J. Eng. Gas Turbines Power*, Vol. 125, pp. 102–112, 2003
- [14] Li, J. Kielb R. E.: *Effects of Blade Count Ratio on Aerodynamic Forcing and Mode Excitability*, *ASME. Turbo Expo: Power for Land, Sea, and Air*, Volume 7B: Structures and Dynamics, GT2015-43304, 2015
- [15] Mayorca, M. A. De Andrade J. A. V. D. M. M. H. F. T. H.: *Effect of Scaling of Blade Row Sectors on the Prediction of Aerodynamic Forcing in a Highly Loaded Transonic Compressor Stage*, *ASME. Journal of Turbomachinery*, Vol. 133, p. 021013-021013-10, 2011
- [16] Moffatt, S. He L.: *Blade Forced Response Prediction for Industrial Gas Trubines - Part I:Methodologies*, ASME Paper 2003-GT-38640, in: *Proc. ASME Turbo Expo 2003*, 2003

-
- [17] Monaco, L.: Parametric Study of the Effect of Blade Shape on the Performance of Turbomachinery Cascades, Master thesis, Royal Institute of Technology (KTH), Stockholm, 2010
- [18] MTU: MTU Aero Engines AG EJ200 Product Sheet, www.mtu.de/fileadmin/EN/7-News-Media/2-Media/Brochures/Engines/EJ200.pdf, 2017
- [19] NUMECA: AutoGrid5 User's Manual, Documentation v8d, March 2010
- [20] Sayma, A.i. e. a.: An Integrated Nonlinear Approach For Turbomachinery Forced Response Prediction. Part I: Formulation, *Journal of Fluids and Structures*, Vol. 14, pp. 87–101, 2000
- [21] Schäfer, B. J.: Determination of the aerodynamic damping in a centrifugal compressor using computational fluid dynamics, Studienarbeit, Institut für Thermische Strömungsmaschinen und Maschinenlaboratorium, Universität Stuttgart, 2016
- [22] Srinivasan, A. V.: Flutter and Resonant Vibration Characteristics of Engine Blades, *ASME J. of Engineering for Gas Turbines and Power*, Vol. 119, pp. 742–775, 1997
- [23] Srinivasan, A. Cutts D. G. S. C.: Turbojet engine blade damping, technical report nasa-cr-165406, NASA, 1981
- [24] Szèchényi, E.: Fan Blade Flutter: Single Blade Instability or Blade to Blade Coupling ?, ASME Paper 1985-GT-216, in: *Proc. ASME Gas Turbine Conference and Exhibit Houston 1985*, 1985
- [25] Verdon, J. M.: Linearized Unsteady Aerodynamic Theory, AGARD-AG-298, AGARD Manual on Aeroelasticity in Axial-Flow Turbomachines, Vol. 1, Unsteady Turbomachinery Aerodynamics, Chapter 2, 1987
- [26] Versteeg, H.; Malalasekera, W.: *An Introduction to Computational Fluid Dynamics: The Finite Volume Approach*, Longman Scientific & Technical, ISBN 9780582218840, 1995
- [27] Vogt, D.: Experimental Investigation of Three-Dimensional Mechanisms in Low-Pressure Turbine Flutter, Dissertation, Royal Institute of Technology (KTH), Stockholm, 2005
- [28] Waite, J. J. Kielb R. E.: Physical Understanding and Sensitivities of LPT Flutter, *ASME Turbo Expo 2014*, 2014